RESONANCE RAMAN STUDIES OF METALLOPORPHYRINS AND SOME IRON CONTAINING ENZYMES

A THESIS

Presented to

The Faculty of the Division of Graduate Studies

By

Lok-Sang Duncan Cheung

In Partial Fulfillment

of the Requirements for the Degree

Doctor of Philosophy

in the School of Chemistry

Georgia Institute of Technology

June, 1978

RESONANCE RAMAN STUDIES OF METALLOPORPHYRINS

AND SOME IRON CONTAINING ENZYMES

Approved:

Ronald H. Felton, Chairman

Nai-Teng Yu

Thomas F. Moran

Date approved by Chairman May 24, 1978

ACKNOWLEGEMENTS

The author is deeply grateful to Dr. Ronald H. Felton for initiating this work and for his guidance and helpful suggestions. The author also wishes to thank Dr. Nai-Teng Yu, Dr. Thomas F. Moran and Dr. Uzi Landman for their reading of this thesis and their suggestions.

Special thanks is extended to Dr. John A. Shelnutt for his friendship and his assistance through discussion.

Especially, the author is indebted to his parents, family and friends for their support and encouragement throughout this study.

Finally, the author wishes to thank his fiancee, Esther, for her patience and understanding which made this work possible.

TABLE OF CONTENTS

TABLE OF CONTENTS (Continued)

LIST OF TABLES

LIST OF ILLUSTRATIONS

LIST OF ILLUSTRATIONS (Continued)

SUMMARY

The research described herein involves the use of resonance Raman spectroscopy to study the excited states of metalloporphyrins, the vibrational structure of the chromophore in camphor bound cytochrome P-450, and the ligation in protocatechuate 3,4-dioxygenase.

Excitation profiles of depolarized modes (b_{1g},b_{2g}) in Ni etioporphyrin I exhibit marked 0-0 resonance Raman intensity upon Q band excitation. By contrast, inversely polarized Raman scattering (a_{2g}) is stronger with 0-1 excitation. Within the Longuet-Higgins representation, a theoretical model is presented which explains the 0-0 enhancements of depolarized modes as arising from interference of intermanifold (Q-B) and intramanifold (Q-Q) vibronic coupling. Comparison of computed and observed excitation profiles shows that a weak Jahn-Teller distortion is present in the Q state. Evidence of increased vibronic coupling of both 400 and 1365cm^{-1} polarized vibrations (a_{1g}) is found in chromium(III) tetraphenylporphyrin chloride with the appearance of a supernumerary peak at 1400cm^{-1} in the excitation profile of the 400cm^{-1} vibration. Excitation profiles of a_{2g} modes in the chromium complex exhibit an apparent decrease in excited state vibrational frequency due to increase coupling.

The vibronic model predicts the behavior of Raman intensity in the B(Soret) electronic states. Resonance Raman spectra of nickel, chromium and copper porphyrins excited at their respective Soret absorption maxima support this treatment. The spectra show a decrease in the scattering intensity for depolarized modes and correlate with diminished $^{1}Q(0\text{-}0)$ absorption in the porphyrins. Inversely polarized vibrations are not observed as predicted.

Direct calculation of vibronic coupling strengths shows a general agreement between the calculated and the Raman-derived constants. The calculated results indicate that four a_{2g} modes should dominate upon Q(0-0) or Q(0-1) excitation as observed. Totally symmetric modes residing between 800-1550cm^{-1} will be the most intense and off-diagonal Q-B coupling usually dominates that of the intramanifold Q-Q coupling. Scattering from b_{2g} vibration is calculated to be smaller than those from b_{1g} vibration and is observed experimentally.

Resonance Raman spectra of camphor bound cytochrome P-450 show low frequency enhancement at 351cm^{-1}. This band is not observed in reduced P-450 and metyrapone complexes of either the oxidized or reduced form. Assignment of the 351cm^{-1} band to a ν(Fe-S) vibration is not conclusive. The oxidation marker band of the reduced P-450cam appears at 1346cm^{-1} and is lower than that of other hemeproteins. This

can be explained by assuming competition for iron dπ electrons between the porphyrin ring and the axial ligand, presumably a thiolate anion.

The resonance Raman spectrum of protocatechuate-3,4-dioxygenase (PCD) exhibits enhanced Raman scattering at 1608, 1508(?), 1264, and 1177cm^{-1}, which is assigned to tyrosine. Saturation of PCD binding sites by the non-metabolized, competitive inhibitors, 3-fluoro-4-hydroxybenzoic acid (3-FHB) and 3-chloro-4-hydroxy-benzoic acid (3-ClHB), results in new , enhanced lines at 1303cm^{-1} in PCD·3-FHB and at 1592 and 1299cm^{-1} in PCD·3-ClHB. Comparison of the Raman spectra of the enzyme-bound inhibitors with those of the free inhibitors in neutral, monoanionic, and dianionic forms provides evidence that inhibitor binding at the active sites does not involve iron ligation by an ionized hydroxyl function.

CHAPTER I

INTRODUCTION

Resonance Raman spectroscopy is a technique that has been used to study electronic and vibrational structure of molecules. The ability to enhance a particular group of vibrations selectively from a complex system makes it valuable for the study of biological chromophores. Because of the inherent spectral properties and biological importance of metalloporphyrins, resonance Raman spectroscopy has been used extensively to study the molecules. A typical metalloporphyrin optical spectrum consists of an intense B(Soret) band in near UV region and a weaker Q(0-0) band in the visible. The Q band often exhibits an additional vibrationally induced structure at Q(0-1) on the higher energy side, and the two visible bands are referred as α and β bands respectively. The electronic structure that gives rise to these bands has been discussed by Gouterman[1,2] and others[3,4], who show that Q band intensity appears primarily by vibronic coupling to the B band.

Theories of resonance Raman intensity that have been developed thus far involve, basically, two kinds of scattering mechanisms. One involves vibrational coupling to a single electronic transition through the Franck-Condon

term; while the other involves vibronic coupling of two closeby electronic states via the Herzberg-Teller perturbation. Thus, metalloporphyrins provide a set of ideal systems to investigate the existing theories.

The following chapters in this thesis contain their own introduction, therefore, no lengthy introduction is given here. However, for clarity, the outline of each chapter is described briefly here. After a brief discussion of resonance Raman theories and the properties of the excited states of metalloporphyrins in Chapter II, Chapter III discusses the study of excitation profiles of NiEtio and CrTPPCl in the visible region. The method used to calculate theoretical excitation profiles is described. Also, details of sample preparation, apparatus and techniques are presented. In Chapter IV, Raman spectra of NiEtio, CrTPPCl and CuTPP at their respective Soret maxima are interpreted in terms of the experimental findings in Chapter III. Experimental techniques involved in using a pulse laser source are discussed. Chapter V describes the method of calculating vibronic coupling strength between Q and B states using coefficients of molecular wavefunction obtained from semi-empirical calculations. In Chapter VI, resonance Raman spectroscopy is used to study the vibrational structures of the chromophore of camphor-bounded cytochrome-P-450 and ligation in protocatechuate 3,4-dioxygenase.

CHAPTER II

THEORY

1. Introduction

The theory of light scattering from an individual particle was first described by Kramer and Heisenberg[5] in 1925 based on second-order perturbation theory. It was later verified by Dirac[6] on the basis of radiation field theory. Raman scattering is one of the processes of light scattering resulting from the interaction of radiation with matter. For a molecular system, an incident photon is destroyed and a scattered photon is created, while the molecular system undergoes a transition from an initial state to a final state. Although this process can be described phenomenologically as a sequential absorption and reemission of a photon by the system which undergoes the transition, the system is not excited for any measurable length of time to a higher energy state since the scattering process is fast. It can only be viewed as a set of inseparable processes with intermediate states involved being purely virtual states. Placzek[7] had shown that when incident light is far away from any optical transition region, the intensity of molecular Raman scattering arises from the dependence of the polarizability on the nuclear vibration.

The initial and final states involved are both ground electronic states, differing, however, in the internal state specification.

If the excitation frequency is in resonance or close to a transition frequency, the process is called resonance Raman scattering. The intermediate states involved are no longer virtual, and Raman intensities of the ground electronic state will reflect the properties of the excited vibronic states. This has been pointed out by Albrecht[8] some time ago. Albrecht[8], and Tang and Albrecht[9] extended Placzek's polarizability theory to include vibronic interaction by using Born-Oppenheimer adiabatic states and expansion of electronic wavefunction in a Taylor series of displacement of nuclear coordinates (Herzberg-Teller expansion). However, the theory was incomplete since the expressions described will give singularities when the exciting frequency is exactly equal to a vibronic transition. Inclusion of damping of states[10] allows their equations to be modified and applied to the study of resonance Raman scattering.

In this chapter, the classical viewpoint of Raman scattering is described first. It gives a pictorial view of some fundamental principles of Raman scattering. Resonance Raman scattering is discussed from the vibronic expansion approach of Tang and Albrecht with the addition of a

non-adiabatic term. In Section 4, a brief description of the excited states of metalloporphyrins is described.

2. Classical Description

From the classical point of view, vibrational Raman scattering is associated with the modulation of the induced dipole moment by the molecular skeletal vibrations. Consider the interaction of an oscillating electromagnetic field, $\vec{E}=\vec{E}_0\cos 2\pi\nu_0 t$, with an non-rotating molecule, the induced dipole moment is

$$\vec{P} = \alpha\vec{E}_0\cos 2\pi\nu_0 t \qquad (1)$$

where α is the molecular polarizability, and ν_0 is the frequency of the incident photon. The molecular polarizability depends upon the molecular conformation which changes with the displacements of the nuclei during vibrations. α may then be expanded in a power series in Q_K, the normal mode of the Kth vibration, around the equilibrium configuration, i.e.,

$$\alpha = \alpha_0 + \left(\frac{\partial\alpha}{\partial Q_K}\right)_0 Q_K^0 \ (\cos 2\pi\nu_K t) + \ldots. \qquad (2)$$

with $Q_K=Q_K^0\cos(2\pi\nu_K t)$. The induced dipole becomes

$$\vec{P} = \alpha_0\vec{E}_0\cos(2\pi\nu_0 t) + \frac{1}{2}Q_K^0\left(\frac{\partial\alpha}{\partial Q_K}\right)_0 \times$$

$$\vec{E}_0 \left[\cos 2\pi(\nu_0+\nu_K)t + \cos 2\pi(\nu_0-\nu_K)t\right] \tag{3}$$

Therefore, when the molecule vibrates with frequency ν_K, the induced dipole oscillates not only with frequency ν_0, but also with frequencies $(\nu_0+\nu_K)$ and $(\nu_0-\nu_K)$. The first term in Eq.(3) gives rise to Rayleigh scattering with unshifted frequency. The second and third terms, yield, anti-Stokes and Stokes Raman scattering respectively, in which the difference between the scattered and excitation frequency is the vibration of the molecular mode. According to the classical electromagnetic theory, a dipole oscillating with frequency ν emits radiation at this frequency, with an intensity given by[11]

$$I = \frac{16\pi^4\nu^4}{3c^2} |\ \alpha\ |^2 \tag{4}$$

With Eq.(3), the scattered light intensity becomes

$$I = \frac{16\pi^4}{3c^2} E_0^2 \left\{ \nu_0^4 \alpha_0 \cos^2(2\pi\nu_0 t) + \frac{1}{4}(\nu_0+\nu_K)^4 \left(\frac{\partial\alpha}{\partial Q_K}\right)^2 \right.$$
$$\times \cos^2\left[2\pi(\nu_0+\nu_K)t\right] + \frac{1}{4}(\nu_0-\nu_K)^4 \left(\frac{\partial\alpha}{\partial Q_K}\right)^2 \tag{5}$$
$$\left. \times \cos^2\left[2\pi(\nu_0-\nu_K)t\right] \right\} + \text{cross terms}$$

and

$$\frac{I_{Stokes}}{I_{anti\text{-}Stokes}} = \frac{(\nu_0-\nu_K)^4}{(\nu_0+\nu_K)^4} \tag{6}$$

The classical theory thus predicts the occurence of Stokes and anti-Stokes lines but incorrect intensity ratios, since it is found experimentally that Stokes lines are much stronger than anti-Stokes lines. This discrepancy can be eliminated if one uses the more complete qunatum theory. However, the classical treatment can be used to describe some fundamental physical principles.

Referring to Eq.(1), the induced dipole and the electric field are vectors and the molecular polarizability is a second order tensor. Equation (1) may be written as,

$$\begin{pmatrix} P_x \\ P_y \\ P_z \end{pmatrix} = \begin{pmatrix} \alpha_{xx} & \alpha_{xy} & \alpha_{xz} \\ \alpha_{yx} & \alpha_{yy} & \alpha_{yz} \\ \alpha_{zx} & \alpha_{zy} & \alpha_{zz} \end{pmatrix} \begin{pmatrix} E_x \\ E_y \\ E_z \end{pmatrix} \tag{7}$$

In non-resonant Raman scattering, the tensor is symmetric.

In most laser Raman experiments, a linearly polarized

laser beam is used as an exciting line. Using the coordinate system shown in Figure 1, in which the laser beam propagates along the z-axis and the electric vector oscillating in the x-direction, the scattered intensity in y-direction (90° scattering) has x and y (I_x,I_y) components and the total intensity collected per solid angle is given by

$$I = \frac{2\pi^3 \nu^4}{c^3} (P_x^2 + P_y^2) \qquad (8)$$

with $I_x \sim P_x^2$, $I_y \sim P_y^2$. By insertion of a polarizer after the sample, one can collect only part of the scattered light, which is polarized in either the x or y direction. The ratio of these two intensities

$$\rho_\ell = \frac{I_y}{I_x} = \frac{I_\perp}{I_{||}} \qquad (9)$$

is called the depolarization ratio where $I_\perp$ and $I_{||}$ are components perpendicular and parallel to $\vec{E}$ respectively. The subscript ℓ denotes linearly polarized, incident radiation. The depolarization ratio can be expressed in terms of invariants of the scattering tensor which are defined by[7,11],

$$G^O = \frac{1}{3}\left[\alpha_{xx} + \alpha_{yy} + \alpha_{zz}\right]^2$$

$$G^S = \frac{1}{3}\left[(\alpha_{xx} - \alpha_{yy})^2 + (\alpha_{xx} - \alpha_{zz})^2 + (\alpha_{yy} - \alpha_{zz})\right]^2 +$$

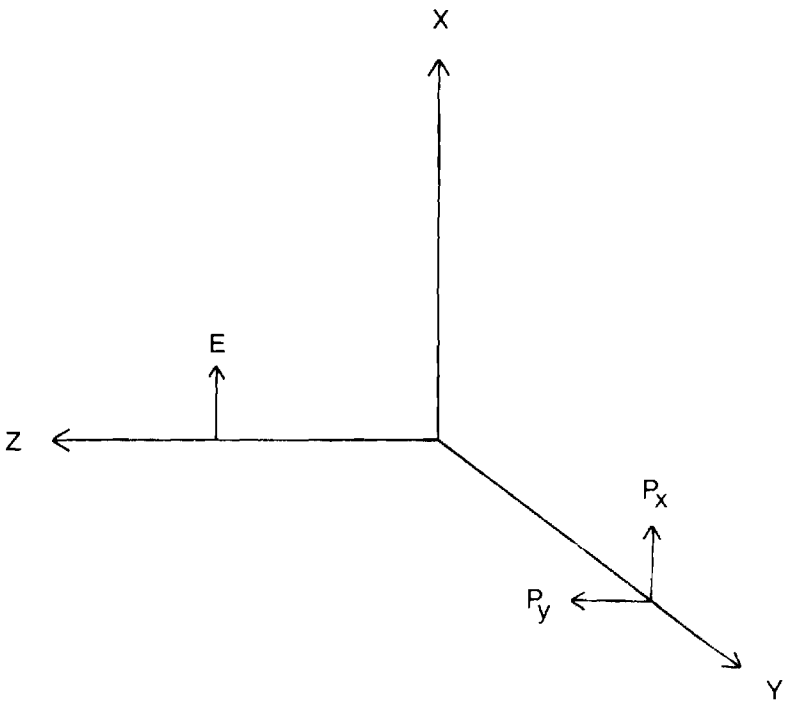

Figure 1. Coordinate System for Observing Scattered Light at 90° Scattering. Light propagating along Z with scattered radiation detected at Y.

$$G^a = \frac{1}{2}\left[(\alpha_{xy} + \alpha_{yx})^2 + (\alpha_{xz} + \alpha_{zx})^2 + (\alpha_{yz} + \alpha_{zy})\right]^2 \quad (10)$$
$$\frac{1}{2}\left[(\alpha_{xy} - \alpha_{yx})^2 + (\alpha_{xz} - \alpha_{zx})^2 + (\alpha_{yz} - \alpha_{zy})\right]^2$$

where G^o is the isotropic or trace component, G^s is the anisotropic component and $G^a$is the antisymmetric component. The depolarization ratio for 90° scattering after averaging over random molecular orientation is

$$\rho_\ell = \frac{3G^s + 5G^a}{10G^o + 4G^s} \quad (11)$$

Far from resonance, $G^o=0$ and the maximum depolarization ratio is 3/4. In C_{4v}, D_{2d}, D_4 or D_{4h} syrmetry, G^o is zero for a non-totally symmetric mode and therefore ρ_ℓ is 3/4. For a totally symmetric mode, ρ_ℓ can have any value between 0 and 3/4. In the near resonance case, the scattering tensor may not be symmetric, i.e., $G^a \neq 0$, and a vibration characterized by $G^s=G^o=0$ may have infinite depolarization ratio.

In D_{4h} symmetry, some scattering tensor patterns[12] are

$$\left(\alpha_{\rho\sigma}\right)_{a_{1g}} = \begin{bmatrix} s_1 & 0 & 0 \\ 0 & s_1 & 0 \\ 0 & 0 & s_2 \end{bmatrix} \qquad (12)$$

$$\left(\alpha_{\rho\sigma}\right)_{a_{2g}} = \begin{bmatrix} 0 & s_3 & 0 \\ -s_3 & 0 & 0 \\ 0 & 0 & 0 \end{bmatrix}$$

$$\left(\alpha_{\rho\sigma}\right)_{b_{1g}} = \begin{bmatrix} s_4 & 0 & 0 \\ 0 & -s_4 & 0 \\ 0 & 0 & 0 \end{bmatrix}$$

$$\left(\alpha_{\rho\sigma}\right)_{b_{2g}} = \begin{bmatrix} 0 & s_5 & 0 \\ s_5 & 0 & 0 \\ 0 & 0 & 0 \end{bmatrix}$$

where s_i represents the components in the tensor operator. From these, the depolarization ratios calculated from Eq.(11) are $\rho_{a_{1g}}=1/8$, $\rho_{a_{2g}}=\infty$, $\rho_{b_{1g}}=\rho_{b_{2g}}=3/4$. Raman lines with $\rho_\ell < 3/4$ are called polarized lines (p), $\rho_\ell = 3/4$, depolarized lines (dp), and $\rho_\ell = \infty$, inversely polarized lines (ip). For inversely polarized Raman bands that show some intensity in $I_{||}$, i.e. $3/4 < \rho_\ell < \infty$, they are called analmously polarized lines(ap).

However, when the scattering tensor components are

complex, it is more convenient for calculation purposes if the tensor invariants of McClain[12] are used. They are defined by

$$\delta_F = \sum_{\rho,\sigma} (\alpha_{\rho\rho})(\alpha_{\sigma\sigma})^*$$
$$\delta_G = \sum_{\rho,\sigma} (\alpha_{\rho\sigma})(\alpha_{\rho\sigma})^* \qquad (13)$$
$$\delta_H = \sum_{\rho,\sigma} (\alpha_{\rho\sigma})(\alpha_{\sigma\rho})^*$$

where σ,ρ =x,y,z and are related to G^o, G^s and G^a by

$$G^o = \frac{1}{3}\delta_F$$
$$G^s = \frac{1}{2}(\delta_G + \delta_H) - \frac{1}{3}\delta_F \qquad (14)$$
$$G^a = \frac{1}{2}(\delta_G - \delta_H)$$

In terms of the McClain invariants, the depolarization ratio for 90° scattering becomes

$$\rho_\ell = \frac{-\delta_F + 4\delta_G - \delta_H}{2(\delta_F + \delta_G + \delta_H)} \qquad (15)$$

3. Resonance Raman Scattering

The total scattering intensity I_{gf} for a Raman transition from the initial state $|g\rangle$ to the final state $|f\rangle$, averaging over all orientation (4π solid angle) of the molecule is given by[13]

$$I_{gf} = \frac{2^3\pi}{3^2c^4} I_o(\omega \pm \omega_K)^4 \sum_{\rho,\sigma} (\alpha_{\rho\sigma})_{gf}^{\ 2} [\mp 1 \pm e^{\pm\hbar\omega_K/kT}]^{-1} \qquad (16)$$

where I_o is the intensity of the incident light, $(\omega \pm \omega_K)$ are the frequencies of the scattered light with $(\omega - \omega_K)$ corresponding to the frequency of the Stokes line. The $\rho\sigma$ component of the polarizability tensor for a transition from $|g\rangle \longrightarrow |f\rangle$ is $(\alpha_{\rho\sigma})_{gf}$. From the second order perturbation theory (Kramers-Heisenberg-Dirac dispersion theory[14]), $(\alpha_{\rho\sigma})_{gf}$ is

$$(\alpha_{\rho\sigma})_{gf} = \sum_e{}' \left[\frac{\langle g|R_\sigma|e\rangle\langle e|R_\rho|f\rangle}{E_e - E_g - h\nu - i\Gamma_e} + \frac{\langle g|R_\rho|e\rangle\langle e|R_\sigma|f\rangle}{E_e - E_f + h\nu - i\Gamma_e} \right] \qquad (17)$$

where E_e and Γ_e are the energy and homogeneous linewidth of the molecular eigenstate $|e\rangle$. R_σ, R_ρ are the electric dipole operators with $\rho,\sigma = x,y,z$. The prime notation in the

summation indicates the summation excludes initial and final states. Evaluation of $(\alpha_{\rho\sigma})_{gf}$ can be treated either as a problem of the nuclear coordinate dependence of the ground state polarizability or as a problem of vibronic spectroscopy. In view of its applicability in discussing resonance Raman spectroscopy, the vibronic approach[9] is described here. The other approach has been discussed in detail by Tang and Albrecht[9].

To treat Raman scattering from vibronic viewpoint, the eigenstates in Eq.(17) are expanded within the adiabatic approximation as

$$\begin{aligned} |g\rangle &= |g(q,Q)\rangle|i(Q)\rangle \\ |f\rangle &= |g(q,Q)\rangle|j(Q)\rangle \\ |e\rangle &= |e(q,Q)\rangle|u(Q)\rangle \end{aligned} \tag{18}$$

where q, Q represent electronic and nuclear coordinates respectively. The electronic wavefunction $|g(q,Q)\rangle$ depends parametrically on Q. The vibrational state $|i(Q)\rangle$ is Q dependent and i denotes a set of vibational quantum numbers. Thus, introducing the expansion (Eq.(18)) into Eq.(17), we obtain

$$(\alpha_{\rho\sigma})_{gi,gj} = \sum_{e,u}{}' \left[\frac{\langle gi|R_\sigma|eu\rangle\langle eu|R_\rho|gj\rangle}{E_{eu} - E_{gi} - h\nu - i\Gamma_{eu}} + \right.$$

(19)

$$\left. \frac{\langle gi|R_\rho|eu\rangle\langle eu|R_\sigma|gj\rangle}{E_{eu} - E_{gj} + h\nu - i\Gamma_{eu}} \right]$$

Using the Herzberg-Teller expansion[15] of an electronic wavefunction in a Taylor series of the displacement of the nuclear coordinate from the equilibrium position in the ground state, and keeping only zero and first order terms, the electronic wavefunctions are given by

(20)

$$|g\rangle = |g^o\rangle + \sum_K \sum_{t\neq g} \frac{(h_K)^o_{gt}\Delta Q_K}{E^o_g - E^o_t}|t^o\rangle$$

$$|e\rangle = |e^o\rangle + \sum_K \sum_{s\neq e} \frac{(h_K)^o_{es}\Delta Q_K}{E^o_e - E^o_s}|s^o\rangle$$

with $Q_K = Q_K - Q^o_K$, E^o_e, E^o_g are electronic energies of states e and g at equilibrium position (Q_K=0). The coefficient of the first order term is the electronic nuclear coupling matrix defined by $(h_K)^o_{es} = \langle e^o|(\frac{\partial H}{\partial Q_K})_0|s^o\rangle$ Insertion of Eq.(20) to (19) yields

$$(\alpha_{\rho\sigma})_{gi,gj} = A_{\rho\sigma} + B_{\rho\sigma}$$

$$A_{\rho\sigma} = \sum_{e}{}' \sum_{u} \frac{M^{\sigma}_{ge} M^{\rho}_{eg} \langle gi|eu\rangle\langle eu|gj\rangle}{E_{eu} - E_{gi} - h\nu - i\Gamma_{eu}} \qquad (21)$$

$$B_{\rho\sigma} = \sum_{e}{}' \sum_{u} \sum_{s\neq e} \sum_{K} \frac{(h_K)^{o}_{es}}{(E^{o}_{e}-E^{o}_{s})(E_{eu} - E_{gi} - h\nu - i\Gamma_{eu})} \times$$

$$M^{\sigma}_{ge} M^{\rho}_{sg} \langle gi|eu\rangle\langle eu|Q_K|gj\rangle + M^{\rho}_{ge} M^{\sigma}_{sg} \langle gi|Q_K|eu\rangle\langle eu|gj\rangle$$

with $M^{\sigma}_{ge}=\langle g^{o}|R_{\sigma}|e^{o}\rangle$. In writing Eq.(21), the second term in Eq.(19) is ignored, since near resonance, it has a much larger denominator than the first term. The prime indicates it is summed over resonant states e only.

In Eq.(21), the first term $A_{\rho\sigma}$ is the product of the dipole transition moment and Franck-Condon overlap factors. Hence, it is also referred as Franck-Condon term. The second term, $B_{\rho\sigma}$, is referred as Herzberg-Teller term. In the Tang and Albrecht's formalism[9], an additional $C_{\rho\sigma}$ term results from inclusion of coupling to the ground states. Customarily, the $C_{\rho\sigma}$ term contribution is presumed small and is ignored.

In non-resonance Raman scattering, the excitation frequency is far from resonance. This results in $[E_{eu} - E_{gi} - h\nu - i\Gamma_{eu}]^{-1}$ being nearly constant. The summation in the A term can be carried out explicitly and reduces to $\langle gi|gj\rangle$. The A term contribution to the

scattering tensor will vanish unless i=j, due to orthogonality of vibrational states. Hence, the A term will contribute to Rayleigh scattering only. Raman scattering derives its intensity from the second B term, where $\langle gi|Q_K|gj\rangle$ as well as $(h_K)^o_{es}$ and M^σ_{ge} and M^ρ_{sg} must be non zero. These lead to the selection rules[11] for Raman active vibrations, whose irreducible representation must transform as x^2, y^2, z^2, xy, xz, or yz symmetry in the point group the molecule possess.

Eq.(21) is obtained based on the adiabatic approximation. In the adiabatic approximation, the total wavefunction is expressed as the product of the electronic and vibrational wavefunctions as in Eq.(18). Improvement within the adiabatic approximation includes the Herzberg-Teller expansion of the electronic wavefunction (Eq.(20)). However, the resultant wavefunctions are still within the adiabatic scheme. Improvement of the adiabatic approximation stems on the inclusion of non-adiabatic coupling between excited states. This arises from the coupling between the vibronic excited states induced by the kinetic energy of the nuclei. The significant contribution of this 'D' term has been discussed by various authors[16-20]. Now, correction with inclusion of non-adiabatic coupling to the first order in the scattering tensor gives

$$(\alpha_{\rho\sigma})_{gi,gj} = A_{\rho\sigma} + B_{\rho\sigma} + D_{\rho\sigma}$$

with

$$D_{\rho\sigma} = \sum_{e}{}' \sum_{u} \sum_{s\neq e} \sum_{x} \sum_{K} \frac{(h_K)^{o}_{es}}{(E^{o}_{e}-E^{o}_{s})(E_{eu} - E_{gi} - h\nu - i\Gamma_{eu})} \times$$

$$\left\{ \frac{h\nu^{s}_{K} M^{\sigma}_{ge} M^{\rho}_{sg} \langle gj|eu\rangle\langle eu|Q_K|sx\rangle\langle sx|gi\rangle(\delta_{u,x-1}-\delta_{u,x+1})}{E_{eu} - E_{sx}} \right. \quad (22)$$

$$\left. - \frac{h\nu^{e}_{K} M^{\rho}_{ge} M^{\sigma}_{sg} \langle gj|sx\rangle\langle sx|Q_K|eu\rangle\langle eu|gi\rangle(\delta_{x,u-1}-\delta_{x,u+1})}{E_{eu} - E_{sx}} \right\}$$

Interference effects in resonance Raman scattering have been discussed by Friedmann and Hochstrasser[21]. They arise when two close by states involved are in resonance. The scattering amplitude will contain cross terms, and depending on the phase of the terms involved, they will add or subtract in the scattering amplitude. The simplest case involved can be found in vibrational levels within the same electronic states. The Raman scattering amplitudes will depend on the Franck-Condon overlap factors. In measuring the excitation profile (a plot of Raman intensity vs excitation energy), the A term will give rise to two maxima.

The number of peaks appear in the excitation profile are limited by the overlap factors, which are small with $u \geq 2$. Phasing between u=0 and u=1 scattering gives rise to contructive interference with

$$I = |A|^2 \sim \left| \frac{\langle g1|e1\rangle}{E_{e1}-E_{g0}-h\nu-i\Gamma_{e1}} - \frac{\langle g0|e0\rangle}{E_{e0}-E_{g0}-h\nu-i\Gamma_{e0}} \right|^2 \quad (23)$$

With similar analogy, the B term will give two peaks also. However, the phasing between u=0 and u=1 will depend on the type of symmetry of vibration under consideration. In D_{4h} symmetry, intensity derives from the B term is of the form

$$I = |B|^2 \sim \left| \frac{1}{E_{e0}-E_{g0}-h\nu-i\Gamma_{e0}} \pm \frac{1}{E_{e1}-E_{g0}-h\nu-i\Gamma_{e1}} \right|^2 \quad (24)$$

with destructive interference (+ sign) occuring for a_{1g}, b_{1g} and b_{2g} vibration and constructive interference (- sign) appearing for a_{2g} vibration.

Inclusion of the non-adiabatic D term will modify the overall excitation profile. Contributions from the B and D terms to the scattering intensity will be

$$I = |B + D|^2 \sim \left| \frac{M^{\rho}_{ge} M^{\sigma}_{sg}}{E_{e0}-E_{g0}-h\nu-i\Gamma_{e0}} \left(1 + \frac{h\nu^{e}_{K}}{E_{e0}-E_{s1}}\right) \right.$$

(25)

$$\pm \frac{M_{ge}^{\sigma} M_{sg}^{\rho}}{E_{el}-E_{g0}-h\nu-i\Gamma_{el}} \left(1 - \frac{h\nu_K^s}{E_{el}-E_{s0}}\right)\Bigg|^2$$

The phasing is the same as for B term alone. Since $E_{e0}-E_{s1} < E_{el}-E_{s0} < 0$, non-adiabatic contribution will tend to add intensity at the 0-1 transition.

4. Excited States of Metalloporphyrins

The basic porphyrin ring is a conjugated heterocycle containing four pyrrole groups linked by methine bridges. Metalloporphyrins are formed when two pyrrole hydrogens in the central region are replaced by a metal. Figure 2 shows the basic skeleton of a metalloporphyrin. Depending on the substituents at any of the outer positions on the pyrrole groups or methine bridges, various types of metalloporphyrins are formed. Two very important natural compounds, chlorophyll and heme, are classified as metalloporphyrins. Also, chlorophyll has one ring reduced and contains a fifth ring.

Figure 3 shows an electronic absorption spectrum of a typical metalloporphyrin. It consists of an intense near UV B(Soret) band ($\varepsilon \sim 1\text{-}6\times10^{5} M^{-1}cm^{-1}$) and a weaker ($\varepsilon \sim 1\text{-}4\times10^{4} M^{-1}cm^{-1}$) Q band in the visible. In addition, a vibrationally induced side band Q(0-1) is often observed.

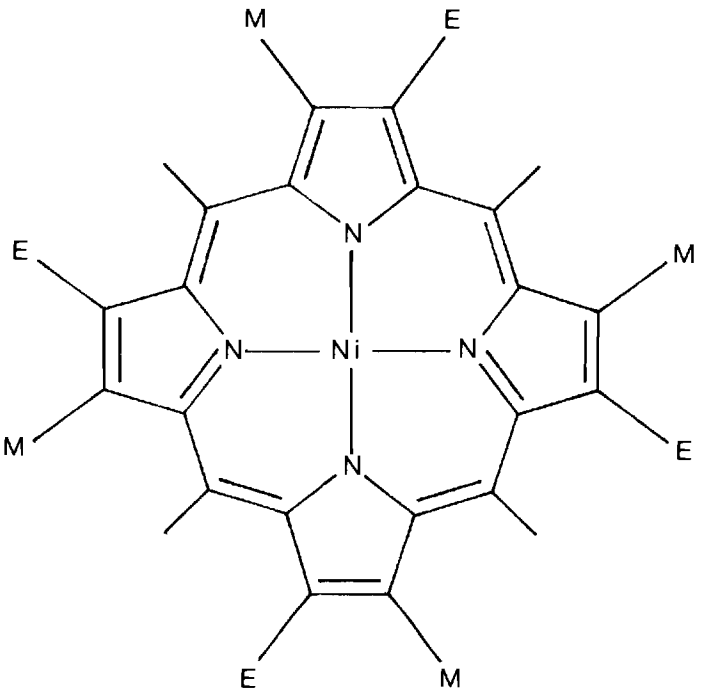

Figure 2. Structure of Nickel(II) Etioporphyrin I.
(M=methyl, E=ethyl)

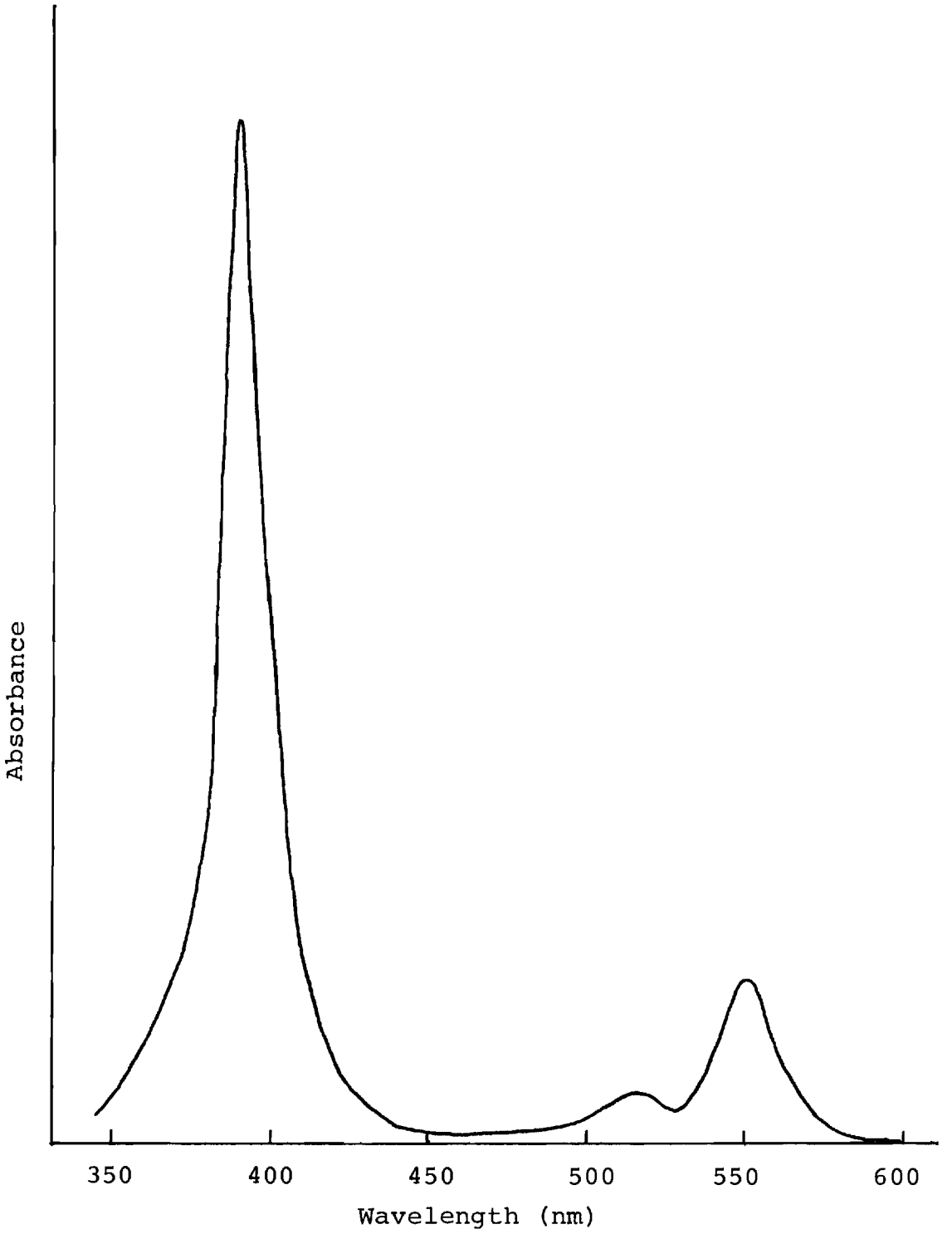

Figure 3. Absorption Spectrum of a Typical Metalloporphyrin. Nickel(II) Etioporphyrin I in Methylene Dichloride.

Q(0-0), Q(0-1) are denoted as α and β bands respectively.

The first successful treatment of the porphyrin spectra was provided by Platt and Simpson[1,2], by treating the molecule as a free electron ring with eighteen electrons. The top filled orbitals have angular momentum around the ring axis of $l_z=\pm 4$ and the lowest empty orbitals have $l_z=\pm 5$. Transition of $l_z=\pm 4 \longrightarrow l_z=\pm 5$ give rise to two pair of excited states with $L_z=\pm 1$ and $L_z=\pm 9$. The former are allowed and can be identified with the strong near UV bands. The latter are forbidden and are assigned to the weaker visible bands. Gouterman[1] has extended this treatment by considering thh top filled a_{1u}, a_{2u} orbitals and the lowest empty e_g orbitals generated by a simple molecular orbital calculation. In square symmetric porphyrin(D_{4h}), a_{1u} and a_{2u} are not necessarily degenerate. However, if they are accidently degenerate, then configuration interaction will give states similar to the free electron model, i.e. the molecule will have strong UV and weak visible bands. Also, he has shown that if the degeneracy between a_{1u} and a_{2u} is lifted, visible bands will gain intensity from the near UV bands.

Molecular orbital calculations of the π system[3] have shown that the highest filled orbitals are nearly degenerate orbitals of a_{1u} and a_{2u} symmetry. The lowest unfilled orbitals are doubly degenerate orbitals of e_g symmetry.

Two singly excited configurations $a_{1u} \longrightarrow e_g$ and $a_{2u} \longrightarrow e_g$ give rise to doubly degenerate states of E_u symmetry. These two states are strongly mixed to yield high intensity of the Soret and the weak intensity of the visible bands. Intensity of the visible Q bands appear primarily by vibronic coupling to the B bands. Vibronic coupling can be treated as a one electron perturbation[103]. An early study of effects of substitution on the absorption spectra of porphin indicated that one electron perturbations of a_{1g}, a_{2g}, b_{1g} and b_{2g} symmetry can couple B and Q bands. In the cyclic polyene model[26], only the non-totally symmetric modes(a_{2g}, b_{1g}, b_{2g}) are vibronically active. However, consideration of the porphyoin ring rather than a sixteen member cyclic polyene shows that it is feasible for the a_{1g} syrmetry vibration to be vibronically active, since it is allowed group theoretically.

CHAPTER III

RESONANCE RAMAN STUDIES OF NICKEL ETIOPORPHYRIN I AND CHROMIUM TETRAPHENYLPOROHYRIN CHLORIDE IN THE VISIBLE REGION

1. Introduction

In the previous Chapter, Albrecht's theory of Raman intensity using the Herzberg-Teller approximation for vibronic coupling and modified by inclusion of non-adiabatic contribution has been described. The calculated Raman excitation profiles will display enhanced intensity when the incident photon frequency is resonant with the 0-1 electronic transition and diminished intensity upon 0-0 resonance. The cited order of enhancement is expected, if the electronic state in resonance is vibronically coupled to an electronic state residing at higher energies. Ideal examples are found in metalloporphyrins, where the resonant state is the Q state and is coupled to the B(Soret) state. Although porphyrins are complex molecules, their absorption spectra have been explained successfully using a simple four-orbital model[2] (Chapter II).

The resonance Raman scattering theory has been applied to the study of manganese porphyrin[20,22], where Raman excitation profiles do show strong 0-1 scattering. However, the visible spectrum of manganese porphyrin is complicated

by charge transfer transitions. It is more appropriate to examine metalloporphyrins that posses a typical absorption spectrum. Nickel etioporphyrin I(NiEtio) and chromium tetraphenylporphyrin chloride (CrTPPCl) are ideal for this study since their Q band absorptions are in a region that can be easily acess by commerical laser systems.

When we examined the Raman excitation profiles of NiEtio, we were surprised to find that depolarized (b_{1g},b_{2g}) and polarized(a_{1g}) modes display strong 0-0 Raman intensity. These profiles are shown in Figure 6. In contrast, inversely polarized modes of a_{2g} symmetry show the anticipated strong 0-1 scattering. The fact that a_{2g} vibrations behave differently from a_{1g}, b_{1g} and b_{2g} modes suggests that a Jahn-Teller effect in the Q state is influencing the excitation profiles. This inference follows, since a_{2g} vibrations are Jahn-Teller inactive in the D_{4h} point group [23]-the symmetry used for discussion of metalloporphyrin electronic states. However, a_{1g}, b_{1g} and b_{2g} modes can couple the degenerate components Q_x and Q_y of the resonant electronic state and, indeed, it is these vibrations which evince abnormally weak 0-1 maxima in the excitation profiles.

Since nondegenerate theories of resonance Raman intensities fail to consider Jahn-Teller coupling, they cannot be applied to the present results. A similar

situation confronted Tusboi and co-workers[24] when they measured the excitation profile of a degenerate vibration in the chromate ion. The resonant electronic state in $CrO_4^{=}$ is triply degenerate. To interpret the profiles, Longuet-Higgins wavefunctions were obtained from a solution of Schrodinger's equation. The vibronic Hamiltonian is restricted to linear coupling within components of the resonant degenerate state. Vibronic wavefunctions are used for intermediate states in the Kramers-Heisenberg-Dirac dispersion expression for the scattering intensity. Recently, Kaya[25] has used a similar approach to assess the effects of a Jahn-Teller distortion on excitation profiles. In both treatments, coupling is restricted to components of the degenerate electronic state.

In this Chapter, Tsuboi et al. and Kayas' treatment are extended for application to Raman scattering in metalloporphyrins. In addition to linear coupling within the resonant manifold(Q_x,Q_y), vibronic interaction with a nearby electronic state (B_x,B_y) is included. The model also derives from Perrin, Gouterman, and Perrins'[26] cyclic polyene representation of excited metalloporphyrin states. In their approach, no coupling terms linear in the nuclear coordinates are supported between Q_x and Q_y states formed from 50/50 mixtures of singly excited configurations. Due to the specific choice of electronic states, not only is the

Jahn-Teller coupling zero but also the electronic transition dipole of the Q state is negligible. Since absorption intensity of the Q(0-0) state in NiEtio is strong, we modify the model to allow borrowing of intensity from the B state by inclusion of a purely electronic interaction between Q and B states. The interaction serves to "unmix" the 50/50 electronic states and thereby introduce linear Jahn-Teller coupling. Profiles calculated with the vibronic wavefunctions display the distinct behavior found experimentally for a_{1g}, a_{2g}, b_{1g} and b_{2g} Stokes fundamentals. The magnitude of the electronic interaction serves to determine the Q(0-0) absorption intensity. Thus, Raman excitation profiles and absorption spectra are related to one another through the vibronic wavefunctions.

After the description of the experimental procedures in Section 2, the vibronic model is outlined in Section 3. Sections 4 and 5 summarize the pertinent results and parameters variations involved in the calculation of excitation profiles. Comparison of computed and experimental profiles for NiEtio and CrTPPCl are discussed in Section 6. Section 7 describes the results in the language of Albrecht's theory.

2. Materials and Methods

Ni(II) etioporphyrin I (NiEtio)

Free base etioporphyrin I and nickel acetate was refluxed in glacial acidic acid until no free base Soret absorption(396nm) was observed in the absorption spectrum. The product was chromatographed on neutal alumina with CH_2Cl_2 and recrystallized from CH_2Cl_2-hexane solution.

Cr(III) 5,10,15,20-tetraphenylporphyrin chloride (CrTPPCl)

1 gm of free base was dissolved in N,N'-dimethylformamide(DMF) under nitrogen. To this solution, 500mg of chromous acetate in 150ml of DMF prepared under nitrogen also, was added slowly as the temperature of the reaction mixture was raised to 110°C. The reaction was monitored spectrophotometrically until the Soret band(416nm) of the free base had disappeared. The product was extracted with CH_2Cl_2, washed with water and dried over sodium sulfate. The porphyrin complex was chromatographed on neutral alumina with (1) benzene and (2) 1% methanol in CH_2Cl_2 to recover chromium porphyrin as its methoxy salt. CrTPPCl was obtained by several recrystallization from a mixture of HCl, methanol and CH_2Cl_2.

Anal. Calculated for CrTPPCl, $C_{44}H_{28}N_4ClCr$: C,75.48 H,4.03 N,8.00 Cl,5.06 for CrTPPCl.CH_3OH, $C_{45}H_{32}N_4OClCr$: C,73.81 H,4.41 N,7.65 Cl,4.84. Found: C,74.24 H,4.33 N,7.91 Cl,5.08.

Raman scattering apparatus

A standard arrangement of the Raman scattering

apparatus is shown in Figure 4. The apparatus consists of an excitation source, a set of optics to direct the incident beam to the sample, optics to collect scattered light, a spectrometer with detector, and photon counting electronics.

The excitation sources were provided by laser lines from the Coherent Radiation Model CR-3,CR-5 argon ion laser(514.5, 501.7, 496.5, 488.0, 476.5, 472.7, 465.8, 457.9nm) or a Model 500K krypton ion laser(520.8, 530.9, 568.2, 647.1nm). An argon ion laser pumped a Coherent Radiation Model 490 dye laser with rhodamine 6G and sodium flourescein as fluorescent dyes provided a tunable range in the region 540-620nm. When pumped with 4 watts all lines of an argon ion laser, the dye laser power with rhodamine 6G was typically 600mW at 600nm and 300mW at 550nm when sodium fluorescein with cyclooctatetraene was used.

An interference filter was employed sometimes to remove plasma lines. This was found necessary if solid samples were used, but not always for solution samples. At times, neutral density filters were used to reduce the incident power in order to avoid excessive heating or possible photodecomposition of samples. A typical laser power measured at the sample region was 50-250mW. The incident laser beam was directed through a set of mirrors and focused into the sample by a 60mm focal length lens. The scattering column was aligned parallel to the vertical entrance slit of the spectrometer.

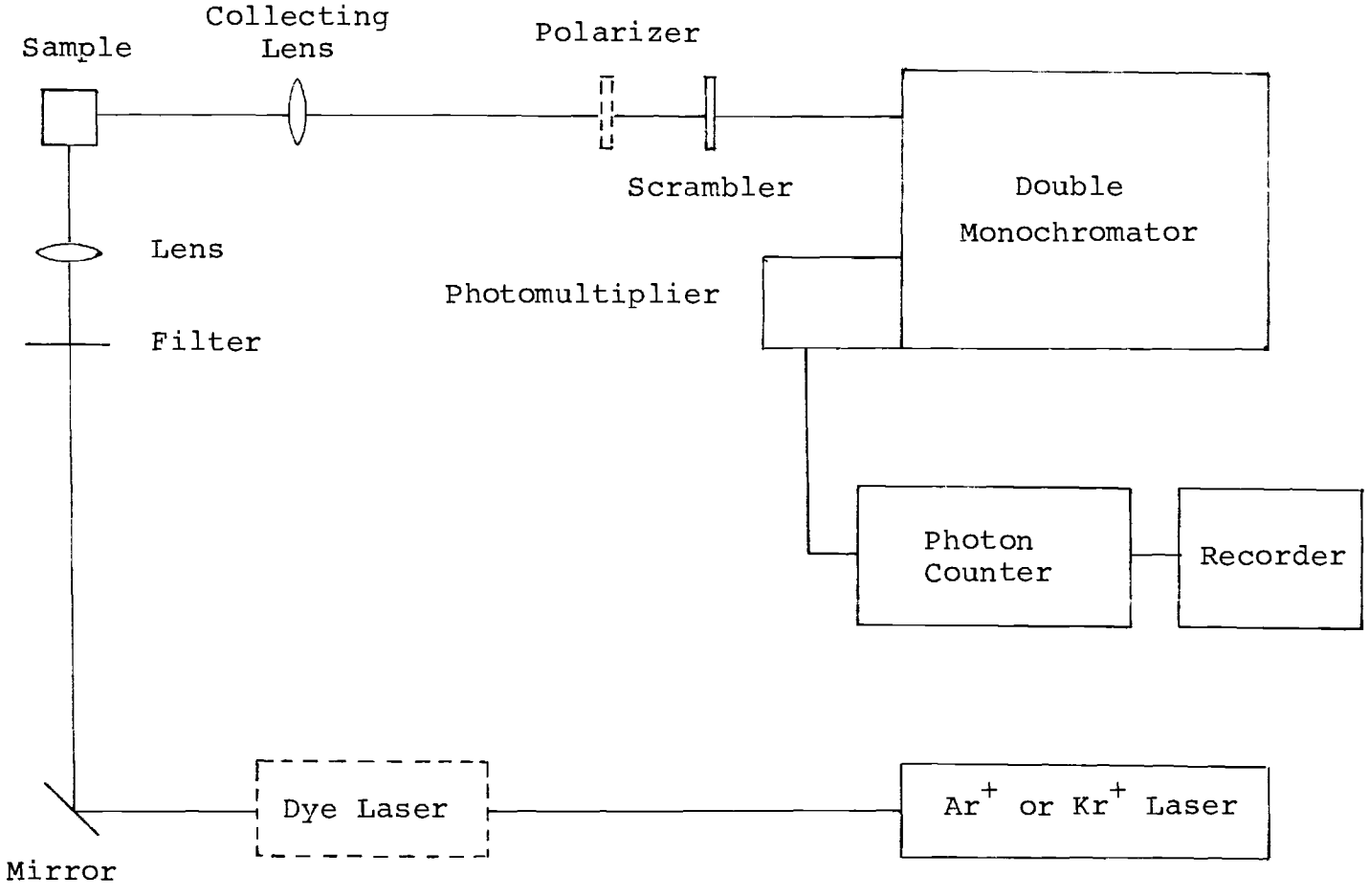

Figure 4. Raman Scattering Apparatus.

For solution sample, a rotating Pyrex sample cell was employed. A Teflon stopper and wax were used to seal the cell in order to prevent a change in concentration through evaporation or to keep the sample under nitrogen atmosphere to avoid photodecomposition. The cell was retained in an aluminum holder by O-rings and rotated at 3600 rpm by a small AC motor. Rotation was necessary to avoid local heating due to sample absorption. The collecting optics for 90° scattering geometry consisted of a set of achromatic lenses with f number of 1.0 and a magnification factor of 6. A polarization scrambler was placed in front of the entrance slit of the spectrometer to insure that the response of the detector and spectrometer was independent of the polarization of the scattered light. For analysis of the parallel and perpendicular components of the scattered light, a polarizer was placed between the collecting lenses and the scrambler.

The spectrometer was a 0.75 meter Spex Czerney-Turner double monochromator (Model 1401). It was equiped with 1200 grooves/mm gratings that were blazed at 500.0nm. The instrument dispersion was .55nm/mm. A typical setting of 250,250 and 250 microns for entrance, intermediate and exit slit widths and an entrance slit height of 10mm produced a spectral resolution of 4-6cm^{-1} with 514.5nm excitation.

The scattered light from the exit slit of the double

monochromator was detected by a thermoelectrically cooled RCA C-31034 photomultiplier. When the phototube was operated at -1680 volts, the dark count was less than 50 counts/sec with a discriminator. The output pulse train from the photomultiplier was processed and counted by the Spex DC-1 photon counting electronics. The results, in the form of intensity (counts/sec) vs. wavenumber were displayed on a X-T recorder with a preset time constant while the double monochromator scanned through the spectral region of interest.

The spectrometer with detector was calibrated by a 45-watt quartz-halogen tungsten helix-coil filament lamp (Optronic Laboratories Model 245C L-124) as a standard of spectral irradiance. Figure 5 shows the relative efficiency curve of the spectrometer with detector. The observed intensities of the rotation lines of D_2 after correction for spectrometer response were comparable to relative intensities calculated theoretically[27] when argon ion laser lines were used for excitation.

Methods

The dye laser using rhodamine 6G or sodium flourescein as fluorescent dyes provided suitable exciting frequencies to cover the Q(0,0) transition of NiEtio and Q(0,0) or Q(0-1) transition of CrTPPCl. Ar^+ and Kr^+ lasers provided isolated lines to irradiate the Q(0-1) absorption of NiEtio

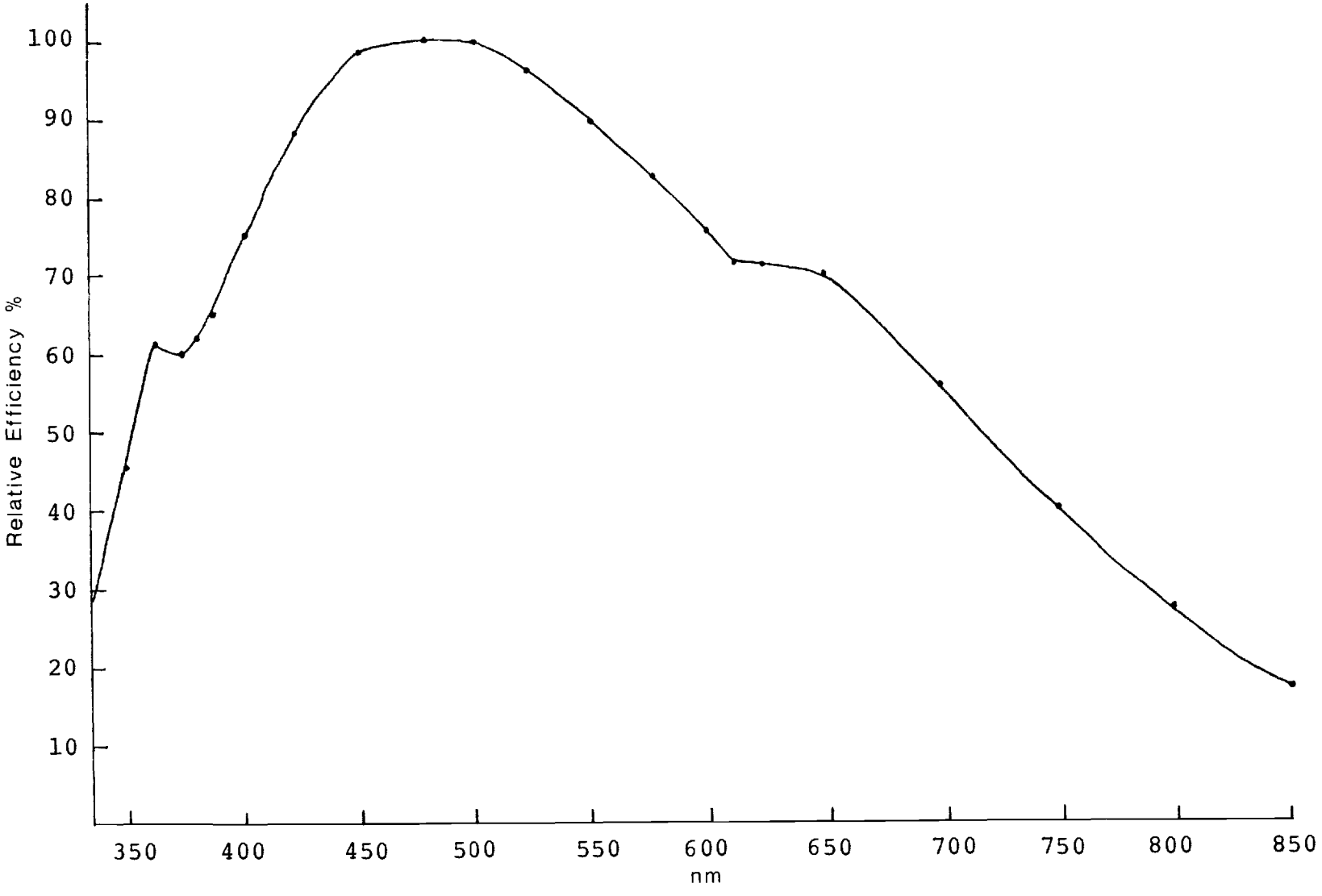

Figure 5. Raman Spectrometer Efficiency Curve in First Order.

and Q(0-2) of CrTPPCl. Excitation profiles, or the intensity of Raman scattering as a function of the frequency of the incident light, were constructed using solvent peaks as internal standards. The profiles were corrected for porphyrin reabsorption[28] as well as relative spectral sensitivity of the spectrometer and detector. For the excitation profiles of NiEtio[29], the 1518 and 1654cm^{-1} bands were obtained in $CDCl_3$:CH_3COCH_3 (2:1) mixed solvent solution using 1709cm^{-1} as reference band. The 342cm^{-1} band was obtained in a CS_2:CH_2Cl_2 (3:1) mixture with 284cm^{-1} serving as a reference. Excitation profiles of other Stokes intensities were obtained in $CDCl_3$ with 907cm^{-1} as the reference band. Finally, all excitation profiles were rescaled such that relative intensities of all Raman lines could be compared at one particular exciting frequency. Using a mixed solvent was necessary in order to get a solvent band which did not overlap with Raman bands. In CrTPPCl, CH_2Cl_2 was used as solvent and it's 1425cm^{-1} band was used as the internal standard.

Absorption spectra were measured before and after laser irradiation. No apparent change in absorption spectrum was observed in NiEtio samples. However, for CrTPPCl samples, it was necessary to seal them under nitrogen atmosphere to avoid photodecomposition.

All absorption spectra were measured on a Cary 14R

spectrophotometer. The concentration of the samples used were $1x10^{-4}$ -$5x10^{-4}$ M.

The excitation profiles of NiEtio were obtained by R.C.C. Chang[29].

3. Theory

In this section, the theory used to interpret metalloporphyrin Raman excitation profiles is described in terms of matrix formulism. The result has included A, B and D terms described in Chapter II automatically. A parallel description in terms of A, B and D terms is given in a following section. Longuet-Higgins wavefunctions obtained here are closely related to those used by Friedman and Hochstrasser[18,30] in a discussion of resonance Raman intensities. Vibronic wavefunctions are expanded in a basis of fixed nuclei electronic states which possess the full molecular geometry(D_{4h}). The nuclear dependence is incorporated as a linear combination of products of harmonic oscillator functions for each normal mode. In the following subsections, the model pertinent to an interpretation of metalloporphyrin Raman band excitation profiles is outlined.

The vibronic Hamiltonian

In the Longuet-Higgins representation[31-34], the solution of the Schrodinger's equation

$$H|i> = E^i|i> \tag{26}$$

is assumed to have the form

$$|i(q,Q)> = \sum_{\ell,\nu,v} C_v^{i\ell_\nu} |\ell_\nu(q)>|v(Q)> \tag{27}$$

where the molecular Hamiltonian is

$$H = T_e + T_N + V(q,Q) \tag{28}$$

T_N, T_e are the nuclear and electronic kinectic energies, q,Q represent the electronic and nuclear coordinate, ν denotes the degenerate set within the ℓth electronic state and $|v(Q)>$ represents the Q dependent vibrational basis. The $C_v^{i\ell_\nu}$ are coefficients to be determined. $V(q,Q)$ is the potential energy. The electronic functions $|\ell_\nu(q)>$ are chosen to satisfy a fixed nucleus Hamiltonian

$$H_e(q,0)\underset{\sim}{\phi}(q) = \underset{\sim}{\varepsilon}\underset{\sim}{\phi}(q) \tag{29}$$

where the electronic Hamiltonian is

$$H_e(q,0) = T_e + V(q,0) \tag{30}$$

and ϕ is the set of $|\ell_\nu(q)>$. The energy matrix, ε, will be a non-diagonal matrix, for depending on the choice of

basis, the fixed nucleus electronic wavefunctions need not be eigenfunctions of $H_e(q,0)$. The equilibrium nuclear configuration of D_{4h} symmetry in the ground state is chosen as Q=0.

Nuclear dependence of the potential energy is expanded in a Taylor series in terms of the normal mode Q_K,

$$V(q,Q) = V(q,0) + \sum_K V^K Q_K + \frac{1}{2}\sum_{K,L} V^{KL} Q_K Q_L \qquad (31)$$

Eq. (31) is regrouped into two terms

$$V_1 = V(q,0) + \sum_K V^K Q_K + \frac{1}{2}\sum_K f^K Q_K^2 \qquad (32)$$

and

$$V_2 = \frac{1}{2}\sum_K (V^{KK} - f^K) Q_K^2 + \frac{1}{2}\sum_{K\neq L} V^{KL} Q_K Q_L \qquad (33)$$

with $V=V_1+V_2$. In V_1, the force constant f^K of the Q_K normal mode in the ground state is introduced. Terms in V_2 will change the composition of the excited states normal coordinates when referred to those of the ground state (Duschinsky effect) [35]. This will not be dicussed and only

linear coupling (V_1) is used to examine the excitation profiles.

Using Equations (26)-(30) and (32) with integration over electronic coordinates lead to a vibronic Schrodinger equation, defined in terms of the electronic basis functions,

$$\sum_{\ell,\mu,\nu}\Big[\delta_{\ell_\nu m_\mu}\Big(T_N + \varepsilon_{m_\mu m_\mu} + \sum_K V^K_{m_\mu m_\mu} Q_K + \frac{1}{2}\sum_K f^K Q_K^2 - E\Big) + (1-\delta_{\ell_\nu m_\mu})\Big(\varepsilon_{m_\mu \ell_\nu} + \sum_K V^K_{m_\mu \ell_\nu} Q_K\Big)\Big] C_v^{\ell_\nu} \,|v(Q)\rangle = 0 \tag{34}$$

with

$$V^K_{m_\mu \ell_\nu} \equiv \langle m_\mu(q) \,|\, (\partial V/\partial Q_K)_0 \,|\, \ell_\nu(q)\rangle \tag{35}$$

$V^K_{m_\mu \ell_\nu}$ is the vibronic coupling matrix induced by Kth normal modes between m and ℓth electronic states. This will be calculated directly in Chapter IV. However, they are treated here as parameters determined by the anaylsis of Raman band excitation profiles. Following specification of the electronic and vibrational basis, Eq. (34) reduces to a matrix eigenvalue equation whose eigenvalues and eigenvectors are the vibronic energies and coefficients

respectively of Eq. (27). In the calculation, the coupling of the ground state to excited states is excluded. Also, because of the limits in dimension of the eigenvalue problem as well as for illustrative purposes, the remaining discussion is developed in terms of two active modes only.

The vibrational basis is the set of harmonic oscillator functions that satisfies

$$(T_N + \varepsilon_{m_\mu m_\mu} + \frac{1}{2}\sum_K f^K Q_K^2)\,|v(Q)> = E_v^{m_\mu}\,|v(Q)> \qquad (36)$$

Here $E_v^{m_\mu} = \varepsilon_{m_\mu m_\mu} + \Sigma_K(v_K + \tfrac{1}{2})\hbar\omega_K$, $|v(Q)>$ is the product of harmonic oscillator with quantum numbers $v=(v_K, v_J....)$ for $Q_K, Q_J.....$

The electronic states composing ϕ are the doubly degenerate, excited states generated from a 50/50 mixture of the excited configurations $4e_g \longleftarrow 1a_{1u}$ and $4e_g \longleftarrow 3a_{2u}$. These states constitute Gouterman's four orbital model[2] describing the porphyrin $\pi^* \longleftarrow \pi$ electronic spectrum. The lowest excited state has components Q_x and Q_y, with a weak 0-0 absorption. At higher energy, the B state with components B_x and B_y is strongly dipole allowed. Even upon inclusion of vibronic coupling, intensity of the Q(0-0) band absorption is negligible due to cancellation of transition dipoles. Since the Q(0-0) band oscillator strength is

pronounced in NiEtio (~0.06 that of B band) and to account for this intensity, matrix elements $\varepsilon_{Q_xB_x} = \varepsilon_{Q_yB_y} = \delta$ are non zero in Eq. (29). These intermanifold elements serve to 'unmix' the 50/50 combination and will introduce dipole intensity into the Q state. The magnitude of δ has been shown to be one-half the energy difference between the filled $3a_{2u}$ and $1a_{1u}$ molecular orbitals[2]. However, δ will be treated as a parameter in this calculation determined by absorption spectrum and experimental excitation profiles.

Vibronic wavefunctions

Determination of the vibronic wavefunctions and energies is reduced to the solution of $\underset{\sim}{H}\underset{\sim}{C}^i = \underset{\sim}{E}\underset{\sim}{C}^i$ with the matrix H-E shown explicitly for two modes,

$$
\begin{array}{c}
\\
\text{H-EI} = \\
\\
\\
\\
\\
\\
\\
\\
\\
\end{array}
\begin{array}{c}
\begin{array}{ccccccccc} |00\rangle & |01\rangle & |10\rangle & |02\rangle & |11\rangle & |20\rangle & |12\rangle & \ldots \end{array} \\
\begin{bmatrix}
\underset{\sim}{E}_{00} & \underset{\sim}{S}_K^{01} & \underset{\sim}{S}_J^{01} & 0 & 0 & 0 & 0 & \ldots \\
\underset{\sim}{S}_K^{01} & \underset{\sim}{E}_{01} & 0 & \underset{\sim}{S}_K^{12} & \underset{\sim}{S}_J^{01} & 0 & 0 & \ldots \\
\underset{\sim}{S}_J^{01} & 0 & \underset{\sim}{E}_{10} & 0 & \underset{\sim}{S}_K^{01} & \underset{\sim}{S}_J^{12} & 0 & \ldots \\
0 & \underset{\sim}{S}_K^{12} & 0 & \underset{\sim}{E}_{02} & 0 & 0 & \underset{\sim}{S}_J^{01} & \ldots \\
0 & \underset{\sim}{S}_J^{01} & \underset{\sim}{S}_K^{01} & 0 & \underset{\sim}{E}_{11} & 0 & \underset{\sim}{S}_K^{12} & \ldots \\
0 & 0 & \underset{\sim}{S}_J^{12} & 0 & 0 & \underset{\sim}{E}_{20} & 0 & \ldots \\
0 & 0 & 0 & \underset{\sim}{S}_J^{01} & \underset{\sim}{S}_K^{12} & 0 & \underset{\sim}{E}_{12} & \ldots \\
\vdots & \vdots & \vdots & \vdots & \vdots & \vdots & \vdots &
\end{bmatrix}
\end{array}
\qquad (37)
$$

Elements of the 4x4 submatrix $S_K^{v,v+1}$ arise from the linear operator described in Eq. (32),viz.,

$$S_K^{v,v+1} = V^K \langle v|Q_K|v+1\rangle \tag{38}$$

Nonzero matrix are found based on the symmetry of one-electron operator. These elements are

$$\begin{aligned}
b_{1g}&: \langle Q_x|S_J^{v,v+1}|B_x\rangle = -\langle Q_y|S_J^{v,v+1}|B_y\rangle = h_J\left[\frac{v+1}{\hbar\omega_J}\right]^{\frac{1}{2}}\\
b_{2g}&: \langle Q_x|S_K^{v,v+1}|B_y\rangle = \langle Q_y|S_K^{v,v+1}|B_x\rangle = h_K\left[\frac{v+1}{\hbar\omega_K}\right]^{\frac{1}{2}}\\
a_{2g}&: \langle Q_x|S_L^{v,v+1}|B_y\rangle = -\langle Q_y|S_L^{v,v+1}|B_x\rangle = h_L\left[\frac{v+1}{\hbar\omega_L}\right]^{\frac{1}{2}}\\
a_{1g}&: \langle Q_x|S_M^{v,v+1}|B_x\rangle = \langle Q_y|S_M^{v,v+1}|B_y\rangle = h_M\left[\frac{v+1}{\hbar\omega_M}\right]^{\frac{1}{2}}
\end{aligned} \tag{39}$$

and

$$\langle Q_x|S_M^{v,v+1}|Q_x\rangle = \langle B_x|S_M^{v,v+1}|B_x\rangle = \langle Q_y|S_M^{v,v+1}|Q_y\rangle$$

$$\langle B_y|S_M^{v,v+1}|B_y\rangle = h_M'\left[\frac{v+1}{\hbar\omega_M}\right]^{\frac{1}{2}}$$

For mass-weighted nuclear coordinates, the quantity labeled h_J is related to V^J by $h_J = 2^{-\frac{1}{2}} V^J_{Q_x B_x}$. The additional linear terms appearing in the a_{1g} matrix elements operate within the Q or B manifold and result from a possible shift in equilibrium geometry of Q or B states referenced to the ground electronic state. All other terms in Eq. (39) couple Q states with B states. As noted earlier, absence of Jahn-Teller coupling by a_{1g}, b_{1g} or b_{2g} modes is a consequence of the electronic basis states chosen. When the purely electronic coupling δ is nonzero, the electronic basis is rearranged and a linear Jahn-Teller coupling is introduced. The energy matrix is defined by

$$\underset{\sim}{E}_{v_J v_K} = \begin{array}{c} \\ |Q_x\rangle \\ |Q_y\rangle \\ |B_x\rangle \\ |B_y\rangle \end{array} \begin{array}{c} \begin{array}{cccc} |Q_x\rangle & |Q_y\rangle & |B_x\rangle & |B_y\rangle \end{array} \\ \begin{bmatrix} E^Q_{v_J v_K} - E & 0 & \delta & 0 \\ 0 & E^Q_{v_J v_K} - E & 0 & \delta \\ \delta & 0 & E^B_{v_J v_K} - E & 0 \\ 0 & \delta & 0 & E^B_{v_J v_K} - E \end{bmatrix} \end{array} \tag{40}$$

where δ is of a_{1g} symmetry. Solution of the eigenvalue problem yields doubly degenerate eigenvalues in molecules possessing a four fold symmetry axis. Convergence in the

harmonic oscillator basis is tested by increasing the maximum vibrational quantum number, v_{max}. With only two modes coupling, convergence is rapid as judged by computed excitation profiles and absorption spectra. In general, $v_{max}=3$ is sufficient. However, with stronger coupling $v_{max}=6$ is required.

Vibronic wavefunctions obtained here in the form of Eq. (27) are

$$|i\rangle = C_{00}^{iQ_x}|Q_x\rangle|00\rangle + C_{00}^{iQ_y}|Q_y\rangle|00\rangle + C_{00}^{iB_x}|B_x\rangle|00\rangle + C_{00}^{iB_y}|B_y\rangle|00\rangle + C_{01}^{iQ_x}|Q_x\rangle|01\rangle + C_{01}^{iQ_y}|Q_y\rangle|01\rangle + \ldots \quad (41)$$

Here, $|v_J v_K\rangle$ is a ket labeled by vibrational quantum number for the Jth and Kth modes. $C_{00}^{iQ_x}$ is the coefficient of the eigenfunctions. The dimension of the eigenvalue problem is given by $d=4(v_{K_{max}}+1)(v_{J_{max}}+1)$.

Calculation of Raman intensity, depolarization ratio and absorption

The vibronic energies E^i and wavefunctions obtained as described in previous section are used to calculate the tensor elements, $\alpha_{\rho\sigma}$. For near resonance, the Raman scattering tensor is expressed as Eq. (17)

$$\alpha_{\rho\sigma}^{n\,n'} = \sum_{i} \frac{\langle n'|R_\sigma|i\rangle\langle i|R_\rho|n\rangle}{E^i - E^n - \hbar\omega - i\Gamma_i} \qquad (42)$$

where $|n'\rangle$ and $|n\rangle$ are final and initial molecular eigenstates, with eigen energies $E^{n'}$ and E^n, respectively. R_ρ is the ρth component of the dipole operator and $\hbar\omega$ is the incident photon energy. The sum is over all vibronic states excepting n. Γ_i is the homogeneous level width of the intermediate state $|i\rangle$.

A stokes fundamental transition is characterized by $|n\rangle = |G\rangle|00\rangle$ and $|n'\rangle = |G\rangle|01\rangle$ for the Kth mode. Since harmonic oscillator functions used in the excited states are referenced to the equilibrium configuration of the ground state $|G\rangle$, orthogonality between these functiions limits contribution to a few terms of the excited states wavefunctions. In the model, all absorption intensity to say $|1\rangle$, the vibronic wavefunction corresponding to one component of Q(0-0), arises from admixture of $B_x|00\rangle$ or $B_y|01\rangle$ into $|1\rangle$. To account for the possibility that some Franck-Condon transition dipole strength to Q(0-0) caused by incomplete cancellation of transition dipoles $\langle a_{1u}|ex|e_g\rangle$ and $\langle a_{2u}|ex|e_g\rangle$, we have included this feature in terms of the ratio $r=R_Q/R_B$, where $R_Q = R_{Q_x} = R_{Q_y} = \langle G|ex|Q_x\rangle$ is included in the scattering tensor. Thus, from Eqs.(41) and (42), the scattering tensor for the Kth fundamental becomes

(43)

$$\alpha_{\rho\sigma}^{00,01} = \sum{}' \frac{R_B^2}{E^i - E_{00}^G - \hbar\omega - i\Gamma_i} \left[r^2 C_{00}^{iQ_\sigma} C_{01}^{iQ_\rho} + C_{00}^{iB_\sigma} C_{01}^{iB_\rho} + r\left(C_{00}^{iQ_\sigma} C_{01}^{iB_\rho} + C_{00}^{iB_\sigma} C_{01}^{iQ_\rho}\right) \right]$$

where E_{00}^G is the ground state energy and ρ,σ represent x,y component of the tensor. The total Raman intensity collected at 90° is

$$I \sim I_o(6\delta_G + \delta_F + \delta_H) \tag{44}$$

where δ_F, δ_G, δ_H are the McClain scattering tensor invariants[12], expressible in terms of $\alpha_{\rho\sigma}$. The depolarization ratio for linearly polarized incident light is Eq. (15)

$$\rho_\ell = \frac{4\delta_G - \delta_F - \delta_H}{2(\delta_G + \delta_F + \delta_H)} \tag{45}$$

and the absorbance (ε) is proportional to

$$\varepsilon \sim \sum_\sigma \sum_i \left| \frac{rC_{00}^{iQ_\sigma} + C_{00}^{iB_\sigma}}{E^i - E_{00}^G - \hbar\omega - i\Gamma_i} \right|^2 \tag{46}$$

4. Results

In Figure 6, the NiEtio excitation profiles of most polarized (p) and depolarized (dp) Stokes fundamentals are characterized by the dominant 0-0 maximum. This feature is found for the 342(p), 1139(p), 752(dp), and 1654(dp) cm^{-1} bands. In addition, the profiles of the 805(p), 986(dp), 1228(dp), and 1271(dp) cm^{-1} modes[29] also show the same feature. Four modes shown in Figure 6 do not fit this classification: the 1518(p) and 1159(dp) cm^{-1} scattering intensities are largest with 0-1 excitation, as are the inversely polarized (ip) modes at 1118 cm^{-1} in h_4-NiEtio and 1205cm^{-1} in d_4-NiEtio.

Other features which are noteworthy include: (1) profiles of the 1118(ip) and 1205(ip) cm^{-1} modes display relative 0-0 to 0-1 maxima intensities of 1:2-3 and constructive interference between the maxima (constructive interference is manifested by appreciable Raman intensity in the region between 0-0 and 0-1 maxima); (2)by comparison, depolarized modes at 1159(dp) and 1654(dp) cm^{-1} exhibit destructive interference between the maxima; and (3) the peak-to-peak separation is close to the vibrational frequency of the fundamental in the ground electronic state.

In CrTPPCl (Figure 7), marked constructive interference for inversely polarized modes at 831, 1244, 1339, and 1518cm^{-1} is found. The excitation profile of the

Figure 6. Resonance Raman Excitation Profiles of Ni(II) Etioporphyrin I. Vibrations at 1205 and 1118cm^{-1} are inversely polarized(ip); 1654, 1159 and 752cm^{-1} are depolarized(dp); 1518, 1139 and 342cm^{-1} are polarized(p). Raman intensity is corrected for chromophore absorption. Profiles and baselines are displaced vertically for clarity of presentation; $-h_4$ denotes meso-proto NiEtio, and $-d_4$ is meso-deutero NiEtio. The frequency of the exciting light is given in kK=1000cm^{-1}. The ^1Q absorption is shown at the bottom of the figure. (Experimental data were obtained by Dr. R.C.C. Chang, Ph.D. Thesis, Georgia Institute of Technology, 1976).

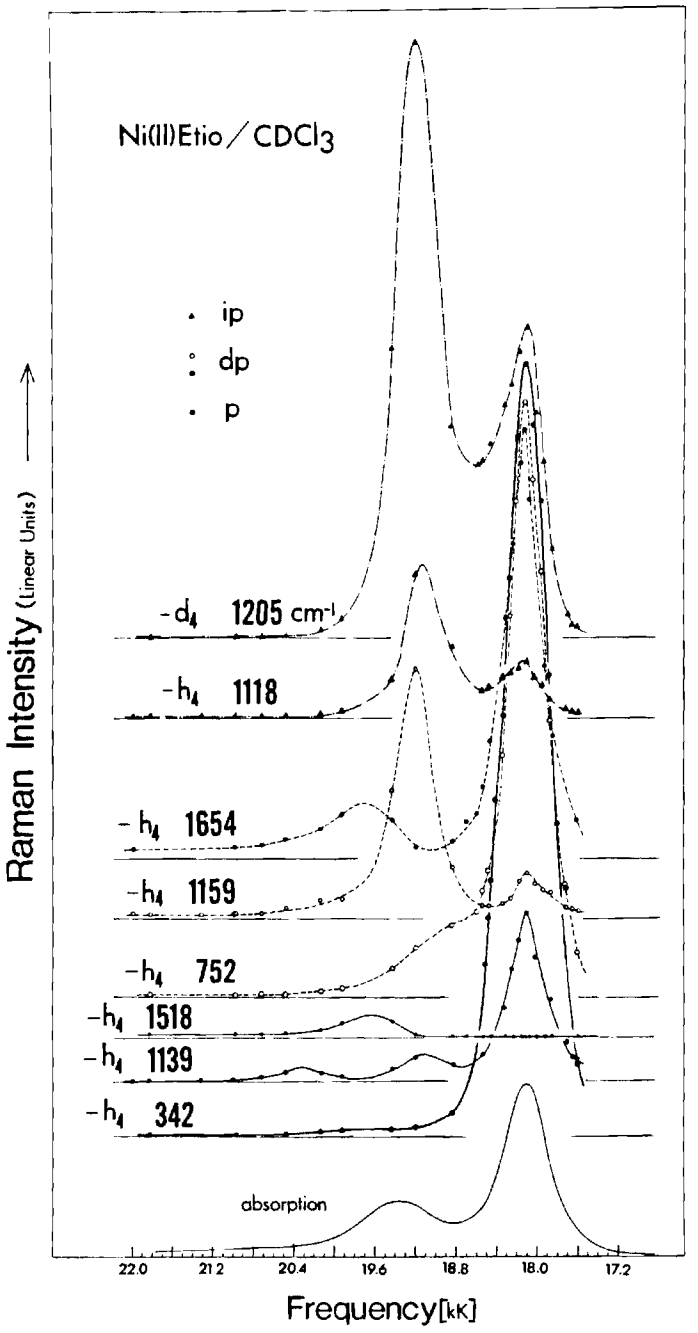
Ni(II)Etio / CDCl3
ip
dp
p
-d4 1205 cm-1
-h4 1118
-h4 1654
-h4 1159
-h4 752
-h4 1518
-h4 1139
-h4 342
absorption
Raman Intensity (Linear Units)
22.0
21.2
20.4
19.6
18.8
18.0
17.2
Frequency[kK]

Figure 7. Resonance Raman Excitation Profiles of Cr(III) Tetraphenylporphyrin Chloride. Lines at 831, 1244, 1339, and 1518cm^{-1} are inversely polarized; 1498, 1025, and 1088cm^{-1} are depolarized; 1365 and 400cm^{-1} are polarized. Profiles are corrected for samples absorption and representative error bars are shown. The ^{1}Q absorption in CrTPPCl is shown at the bottom of the figure.

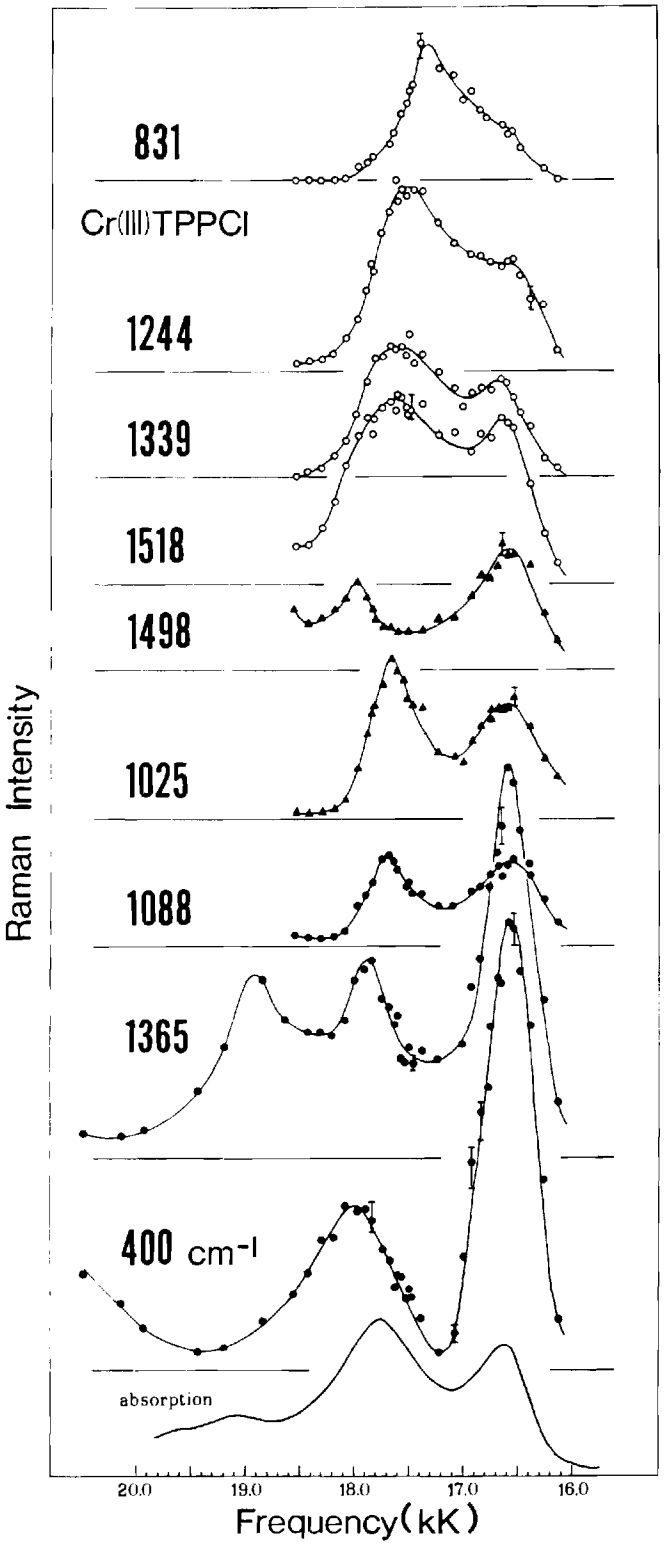
831
Cr(III)TPPCl
1244
1339
1518
1498
1025
1088
1365
400 cm⁻¹
absorption
Raman Intensity
20.0
19.0
18.0
17.0
16.0
Frequency(kK)

low frequency polarized at $400cm^{-1}$ shows a supernumerary maximum at $1400cm^{-1}$ above the 0-0 maximum. In conjunction with this feature (absent in NiEtio), the $1365(p)cm^{-1}$ profile has an extra maximum located at an energy $\sim 2x1365cm^{-1}$ above the 0-0 maximum. The absorption spectrum of the CrTPPCl Q band has a relatively intense 0-2 absorption, which is not found in NiEtio. Dominant 0-0 maxima are not observed for depolarized modes.

The depolarization ratio $\rho_\ell = I_\perp/I_\parallel$ displays no dispersion. For Raman spectra of both porphyrins, no $I_\perp$ components for inversely polarized modes are observed. The depolarization ratio for modes classified as depolarized is 0.75 ± 0.05 with no evidence of dispersion.

In both Figures 6 and 7, the relative Raman intensities of the bands are shown on a linear scale of intensity. However, comparison of Raman intensities between CrTPPCl and NiEtio is not possible with the data shown, due to the differing porphyrin concentrations and solvents.

5. Calculated Excitation Profiles

Effect of parameter variation

The computation of an excitation profile requires that a number of parameters be estimated. Each mode requires one vibronic coupling constant h_K, and an additional parameter h'_K is present for a_{1g} modes due to an origin shift of $|Q>$

and $|B\rangle$ relative to the ground electronic state. Values of (1) δ, (2) the unperturbed B-Q energy separation, and (3) r are properties of the electronic states and are independent of the normal modes examined. Vibrational frequencies ν_i are those of the ground electronic state and are taken from the Raman spectra. The level width Γ_i is $250cm^{-1}$ for all Raman profiles and is obtained from the experimental profiles shown in Figs. 6 and 7.

For NiEtio the unperturbed B-Q separation is fixed at $6500cm^{-1}$-a value found in CuTPP, which displays negligible Q(0-0) absorption. It is useful to recall from Section 3 that small Q(0-0) absorption implies a 50/50 mixture of singly excited configurations for the Q and B states. Excepting small vibronic shifts, $6500cm^{-1}$ is an accurate estimate of the average, unperturbed separation. Gouterman cites $6700cm^{-1}$ for a series of metallotetraphenylporphyrins[1]. The number of parameters is reduced by expressing all energies appearing in Eq. (37) in units of δ.

The coefficient vector C^i is a function of definite parity in δ or h_K, when a_{1g} coupling within the degenerate manifolds is absent. Therefore, the sign of δ or h_K will have no influence upon the excitation profiles, if r=0 and intramanifold a_{1g} coupling is not included. The effect of $r=R_Q/R_B$ is minimal, since it is chosen to be small

in accord with the four-orbital model however, larger values of $r \sim 0.1$ naturally altered the Q(0-0) dipole strength. Excitation profiles calculated for $r \neq 0$ change slightly when the sign of δ is changed. The coefficients are used to generate Q-band excitation profiles characterized by 0-1/0-0 Raman intensity ratio, relative Raman intensities of the modes, and Q(0-0)/B or Q(0-1)/B absorption ratios. There is a further restriction that the separation between 0-0 and 0-1 profile maxima be consistent with the data. For the Q and B band excitation profiles shown and Fig. 8, a total of nine parameters were used. If we were to fit only the profiles of the Q state and the absorption spectrum phhnomenologically, 14 parameters are required(two for each profile and an aditional two for the absorption ratios). The vibronic wavefunctions obtained by fitting the Q-band profiles allow us to predict excitation profiles behavior in the B band(Fig. 8) and could yield approximate combination and overtone profile behavior. Excitation profiles exhibited in Figs. 8 and 9 are calculated with the parameter set listed in Table I. Values are obtained by trial and error comparison of computed and experimental profiles.

δ -variation

We list changes in the excitation profile of a Jahn-Teller mode as $|\delta|$ increases with weak vibronic coupling [$h_K(\hbar\omega)^{-\frac{1}{2}} < 500 cm^{-1}$]. The alterations are as

follows: (1) when $\delta=0$, no Jahn-Teller coupling is present. The 0-1/0-0 Raman intensity ratio is ~2 and is predicted by nondegenerate perturbation theories of Raman scattering(Chapter II). The stronger 0-1 intensity reflects non-adiabatic coupling in these theories. (2)For $\delta\sim500cm^{-1}$ the 0-1/0-0 is ~2, but falls rapidly until $\delta\sim1000\text{-}1300cm^{-1}$ where the 0-1/0-0 ratio is $\ll1$.(3)For $\delta>1300cm^{-1}$ the 0-1/0-0 intensity ratio again increases.

Vibronic coupling variation

For fixed δ, the Raman intensity of the Kth vibration is approximately proportional to h_K^2 . A change of 10% in h_K will markedly alter the Raman intensity, but not the shape of the excitation profile. When vibronic coupling is weak, interference between the 0-0 and 0-1 scattering for the Q state reflects the vibration symmetry as described by Friedmann and Hoschstrasser[18,30] b_{1g}, b_{2g} and a_{1g} (Q-B vibronic) coupling leads to destructive interference; a_{1g} (Franck-Condon) and a_{2g} excitation profiles display constructive interfernce.

As the vibronic interaction increases, contributions to low-lying vibronic states from basis states representing overtones, combinations, and other fundamentals increase. The result is an apparent broadening of the excitation profiles, which obscures the interference effects evident for weak vibronic coupling. In addition, the amount of

$|B_\rho>|00>$ in higher vibronic states grows, and the excitation profiles display supernumerary maxima as these states come into resonance with excitation radiation. Not only is a maximum at the energy of a 0-2 transition observed, but also profiles of two strongly coupling modes will envince maxima at approximately the 0-1 frequencies of both modes and at the combination frequency, although Raman intensity from only one vibration is monitored. Thus the Jth mode may act as a "helping" mode for the Kth vibration. The phenomenon occurs when strong coupling within an electronic manifold results in appreciable magnitudes for $<Q_K>$ and $<Q_J>$. The helping mode phenomenon is briefly discussed in terms of Albrecht's theory in another section.

For metalloporphyrin Raman excitation spectra, the vibronic model predicts additional features: (1)When the vibronic coupling is weak, resonance Raman intensity in the Soret region will be dominated by polarized modes and by depolarized modes which participate in the Jahn-Teller distortion. Inversely polarized vibrations will scatter weakly(Fig.5); (2)If an a_{2g} mode interacts with another mode of any symmetry, we find energies of the vibronic levels are quite sensitive to the magnitude of coupling. Generally, as the coupling strength increases, the energy gap diminishes between the lowest vibronic level and the level containing the largest contribution from the a_{2g} mode. Concomitant with

this change, excitation profiles exhibit and apparent decrease in excited state frequency determined from the 0-0 and 0-1 maxima separation, and intensity in the 0-1 maximum approaches that of 0-0 maximum a situation quite distinct from weak coupling(Fig. 8).

Remarks concerning resonance Raman scattering under strong coupling conditions are qualitative. The linear coupling model employed here is valid for small displacements from Q=0. Neglected quadratic contributions to the vibronic Hamiltonian may be significant. Ziegler and Albrecht[36] find that the linear approximation is valid for transition moments in benzene, when the displacement does not exceed the rms value Q_K^* of a mode. However, the transition moment for 1595cm^{-1} vibration in benzene exhibits nonlinearity for $|\langle Q_K \rangle| > Q_K^*$. Displacements of this size are calculated for CrTPPCl.

6. Comparison of Calculated and Experimental Excitation Profiles

A. NiEtio

Results of paramter variations lead to the excitation profiles shown in Fig. 8, computed for selected NiEtio Raman lines. The corresponding parameters are listed in Table I. For $|\delta| = 1550$cm^{-1}, all computed depolarized mode profiles exhibit the observed weak 0-1 intensity and enhanced 0-0 intensity. This value of δ results in a displacement of approximately 0.5 Q_K^* in the lowest vibronic state. The

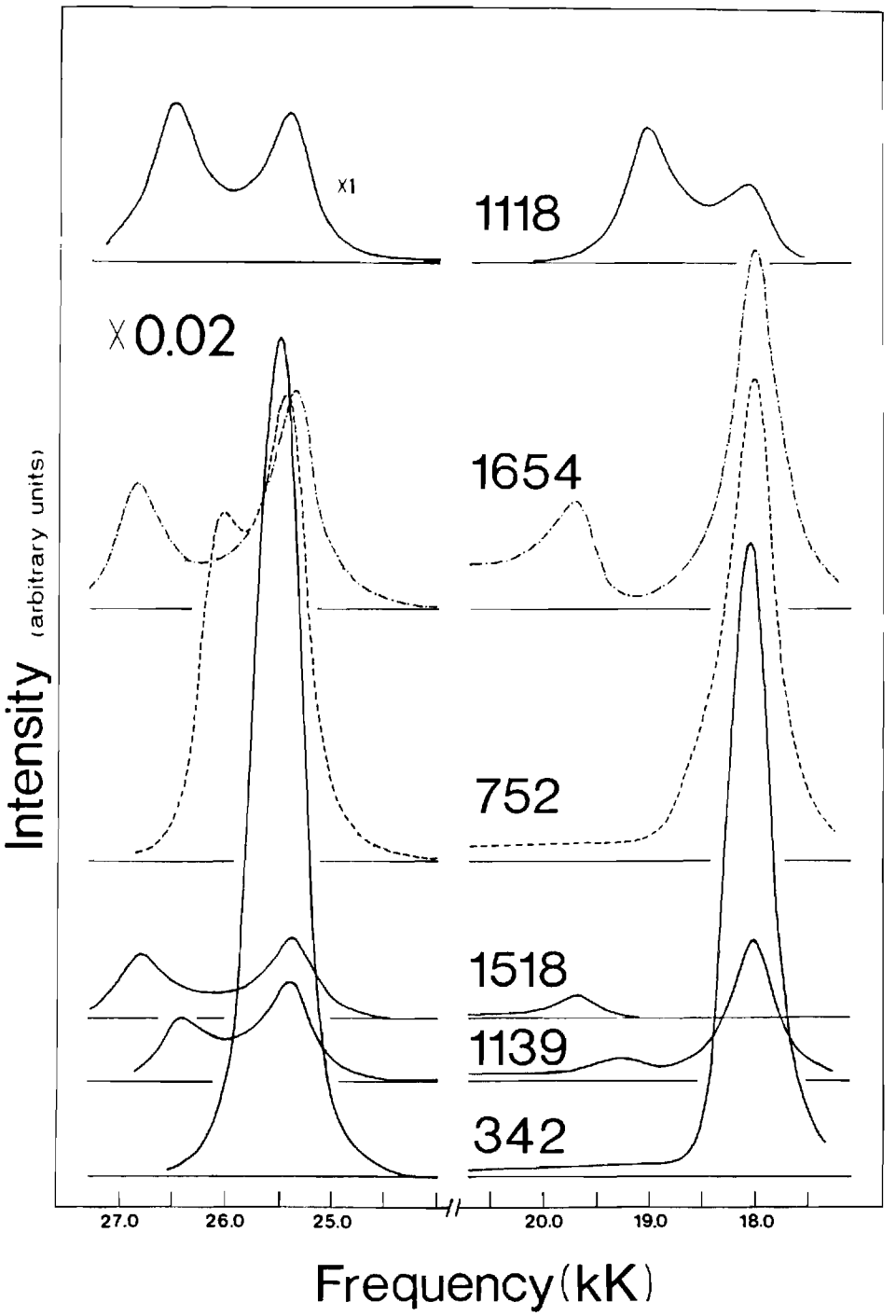

Figure 8. Calculated Excitation Profiles of Selected Vibrations of NiEtio. Vibronic parameters employed are listed in Table I. Raman scattering intensity in the B(Soret) region between 24.0 and 27.0 kK is multiplied by 0.02, excluding the 1118cm^{-1} a_{2g} mode.[Reference to Fig.6]

Table I. Vibronic Parameters

$\bar{\nu}$(cm^{-1})	Q-B coupling[a] $h_K(h\omega)^{-1/2}$ (cm^{-1})	Q-B coupling[a] $V^K\times10^5$ (dynes amu$^{-1/2}$)	Q-Q coupling $V^K\times10^5$ (dynes amu$^{-1/2}$)	Displacement[b] $\langle Q\rangle$	Displacement[b] $Q^*\equiv\langle Q^2\rangle^{1/2}$ (A amu$^{1/2}$)
NiEtio: $E^B_{00}-E^Q_{00}=6500\text{cm}^{-1}$; $\lvert\delta\rvert=1550\text{cm}^{-1}$; r = 0.045					
342(p)	250	2.2		0.15	0.15
752(dp)	375	5.0		0.067	0.10
1118(ip)	400	6.4		0	0.086
1139(p)	220	3.6		0.021	0.084
1518(p)	75	1.4	-1.4	0.0057	0.07
1654(dp)	500	9.8		0.030	0.068
CrTPPCl: $E^B_{00}-E^Q_{00}=5200\text{cm}^{-1}$; $\lvert\delta\rvert=550\text{cm}^{-1}$; r = 0.045					
400(p)	360	3.5	-1.2	0.27	0.15
1365(p)	-700	-12.7	2.9	0.079	0.066
1339(ip)	760	13.7		0	0.079
1518(ip)	770	14.7		0	0.074
1339(ip)	440	7.8		0	0.079
1518(ip)	460	8.8		0	0.074

[a]Coupling is presented both as a matrix element energy and as a force.

[b]$\langle Q\rangle = \langle 1|Q|1\rangle$, $(Q^*)^2 = \langle 1|Q^2|1\rangle$ [see Eq.(41)].

Jahn-Teller displacements are strikingly small; nonetheless, Raman intensity distribution is strongly influenced by the distortion, and a majority of depolarized modes (756,986,1271,1228 and 1654cm^{-1}) display excitation profiles with 0-1/0-0 ratio similar to the polarized modes.

A consequence of Jahn-Teller distortion in the B(Soret) state is that active b_{1g} and b_{2g} modes are predicted to have Raman intensity only slightly less than that of totally symmetric modes. Examination of Fig. 8 and data of Ref.[29] suggest that 1654(dp), 1228(dp) and 752(dp)cm^{-1} modes should be prominent in the Soret state. In ferrocytochrome c depolarized lines are observed[37] at 1622, 1231, and 753(dp) cm^{-1} upon excitation at 363.8nm. Similarly, the 1498 and 1088(dp) cm^{-1}lines of CrTPPCl are discernable upon excitation near the Soret maximum[20]. In the instance of CrTPPCl with a strict fourfold axis, only a Jahn-Teller distortion can give rise to appreciable depolarized mode Raman intensity in the Soret(see Chapter IV). Finally, excitation with the 441.6nm line of a He-Cd laser is close to the Soret maximum of ZnEtio and VOTPP, and Raman spectra show appreciable scattering by depolarized modes: 757 and 1613cm^{-1} for ZnEtio, and 1493cm^{-1} in VOTPP[38].

A key point in support of the interpretation of Jahn-Teller distortion being exhibited by excitation

profiles of a depolarized vibrations is that Jahn-Teller inactive inversely polarized modes, in contrast, show agreement between computed and experimental excitation profiles. The behavior of the 1118(ip) and 1205(ip)cm^{-1} profiles shown in Fig. 8 is in full agreement with no a_{2g} mode coupling between Q_x and Q_y; instead, vibronic coupling must arise from intermanifold, linear coupling of the Q state with the B state. Therefore, Raman intensities of weakly coupled a_{2g} vibrations display the behavior given by the nondegenerate perturbation theory result[Eq.(25)], viz.,

$$I_{Raman} \propto \left| \frac{1}{E^Q_{00} - E^G_{00} - \hbar\omega - i\Gamma_{00}} \left(1 + \left(\frac{\hbar\omega_K}{E^Q_{00} - E^B_{01}}\right)\right) - \frac{1}{E^Q_{01} - E^G_{00} - \hbar\omega - i\Gamma_{01}} \left(1 - \left(\frac{\hbar\omega_K}{E^Q_{01} - E^B_{00}}\right)\right) \right|^2 \quad (47)$$

Since $E^Q_{00} - E^B_{01} < E^Q_{01} - E^B_{00} < 0$, Eq. (44) yields stronger 0-1 scattering due to nonadiabatic terms of $0(\hbar\omega_K / E^Q_{v'} - E^B_v)$.

Unfortunately, this vibronic model is unable to explain the stronger 0-1 maximum of the 1159(dp)cm^{-1} excitation profile. Abe et al. [39] assign this mode as the only b_{2g} vibration seen above 100cm^{-1}[40]. Possibly, neglect of the quadratic potential V_2 in Eq.(33) is unwarranted.

The polarized mode excitation profiles are comparable to the depolarized mode profiles. The 342cm^{-1} peak is composed of overlapping 0-0 and 0-1 scattering. The 1139cm^{-1} band exhibits both a well defined 0-0 and 0-1 peak. The 0-2 maximum is not necessarily as pronounced as that drawn in Fig. 6; nonetheless, there is definitely some 0-2 scattering intensity. An excitation profile of the 1518cm^{-1} Stokes line displays virtually no 0-0 intensity and weak 0-1 intensity. Recently, Friedman and Hochstrasser[30] have assigned a Raman line at 1504cm^{-1} in reduced ferrocytochrome c to an overtone of 752cm^{-1} band at the 0-1 maximum of the fundamental on the other hand, the 1518cm^{-1} band represents a fundamental and is not to be confused with 1504cm^{-1} vibration discussed by Friedman and Hochstrasser. Indeed, Friedman et. al.[41] has observed two polarized bands near 1500cm^{-1} in ferrocytochrome c. In the present study, the excitation profile of the NiEtio polarized fundamental at 1518cm^{-1} requires addition of a diagonal term to the vibronic Hamiltonian. The overall weakness of the Raman intensity for the 1518cm^{-1} (Fig. 6) may permit this manifestation of the cited interference effect. By contrast, strongly scattering polarized modes can be interpreted as possessing either dominant inter- or intra-manifold coupling terms. We are unable to apportion vibronic coupling between inter- and intramanifold interactions. However a study of

Raman excitation profiles in CuTPP suggests that origin shifts in the excited Q state lead to large intramanifold contributions for strongly scattering polarized modes[42]. In the CuTPP spectrum, Q band Raman scattering intensity from depolarized modes is much weaker than from polarized modes; in NiEtio, Raman scattering of comparable intensities observed from polarized, depolarized, and inversely polarized vibrations.

Absence of dispersion in persists even though the excited state is subjected to a Jahn-Teller distortion. Dispersion will occur, however, if degeneracy in the Q state is lifted by an external potential. With a crystal field splitting of $100cm^{-1}$ between Q_x and Q_y electronic energies(found in cytochrome c)[43] and $\Gamma_i=250cm^{-1}$, changes in the calculated depolarization ratios are smaller than 5%, which is less than experimental error. Calculated dispersion in the inversely polarized modes is more dramatic, ranging from $\rho_\ell=30$ to $\rho_\ell=9$ at the 0-0 and 0-1 maxima, respectively. This latter finding agrees with recent conclusions of Collins et al.[44], who explain $1585(ap)cm^{-1}$ dispersion in ferrocytochrome c by zero field splitting. Lack of dispersion in NiEtio and CrTPPCl indicates negligible crystal field splitting in CH_2Cl_2, CS_2 and $CHCl_3$.

B. CrTPPCl

Excitation profiles of this molecule (Fig. 7) bear

little resemblance to those of NiEtio. Depolarized modes at 1498, 1088 and 1025cm^{-1} display nearly equal 0-0 and 0-1 maxima in their excitation profiles. A pronounced 0-2 maximum is noted on the 1365(p)cm^{-1} vibration, and the 400(p)cm^{-1} profile shows a supernumerary maximum at $\sim$1400cm^{-1} above the 0-0 energy. A striking effect is seen with the inversely polarized modes at 1339 and 1518cm^{-1}; the separations in energy between excitation profile maxima no longer correlate with the ground state vibrational frequencies. Also the ratio of 0-1/0-0 Raman intensity is not that predicted by Eq.(47).

Using the parameters given in Table I, calculated excitation profiles, shown in Fig. 9, exhibit these features of the CrTPPCl experimental profiles. The reduction of δ to 550cm^{-1} is consistent with the lower 0-0 absorption (cf. NiEtio). We interpret the behavior shown by the 400 and 1365cm^{-1} polarized mode as exemplifying stronger vibronic coupling than encountered in NiEtio. Appearance of an additional maximum in 400cm^{-1} profile results from vibronic states whose energies are at 1365 and 1365+400cm^{-1} above the lowest vibronic state. Under strong coupling conditions these states contain sufficiently large contribution from $|B_\rho>|00>$ and $|B_\rho>|01>$ to yield scattering intensity. As an ancillary feature to strong coupling, there is appreciable displacement along the 1365cm^{-1} mode of the equilibrium

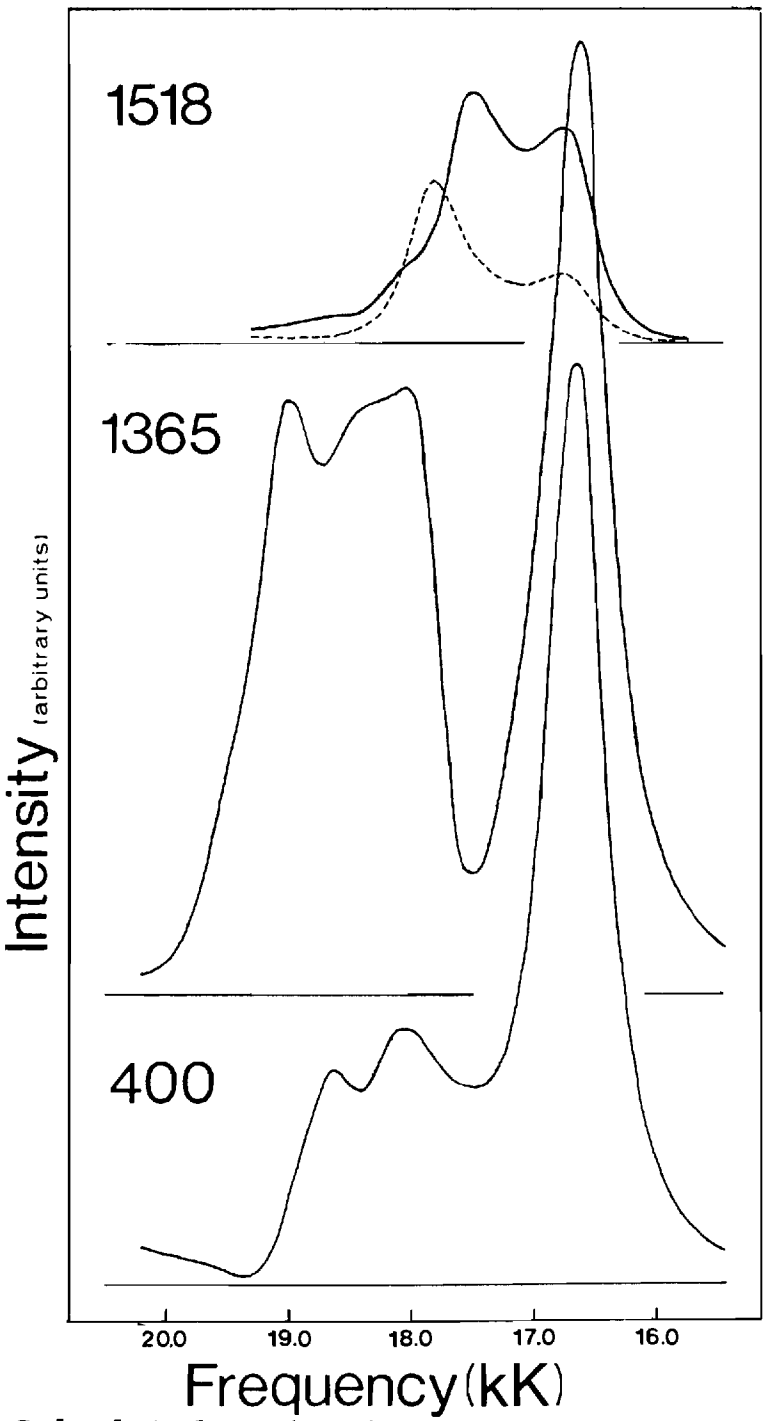

Figure 9. Calculated Excitation Profiles of Selected Vibrations of CrTPPCl. Vibronic parameters employed are listed in Table I. The effect of increasing coupling is displayed for the 1518cm^{-1} a_{2g} mode: weak coupling (-----), strong coupling ($\frac{2g}{\quad\quad}$).

internuclear separation in the Q state, and it is not surprising to see a 0-2 maxiumum in the 1365 (p)cm^{-1} vibration. These two polarized modes are dominant features in Q-band excitation of CrTPPCl. In contradistinction, weaker coupling obtains in NiEtio and no "helping" modes are seen.

If a calculation is performed wherein the 1339 and 1518cm^{-1} a_{2g} modes interact with increasing vibronic coupling, the effect upon the excitation profile of the 1518cm^{-1} is shown in Fig. 9. Energies of the 0-1 or 0-2 vibronic transition differ by 480cm^{-1}, and the 0-1 energy is 970cm^{-1} above the lowest vibronic level. Vibronic wavefunctions associated with these energies are dominated by comparible contributions from $|01\rangle$ and $|10\rangle$ harmonic basis functions. We believe the decreased maxima separation found experimentally in the 1339(ip) and 1518(ip)cm^{-1} profiles is caused by (1) decreased vibronic energies noted above, (2) overlapping 0-1 and 0-2 transitions and (3) the constructive phasing of a_{2g} vibrations. As the coupling strength is reduced, the a_{2g} profile assumes the shape found in NiEtio.

A calculation in which the 1498(dp) and 1518(ip)cm^{-1} vibration are coupled strongly shows eigenvector compositions and vibronic energies comparable to that described for two interacting a_{2g} modes. A major difference

appears in the excitation profile of the depolarized mode which does not exhibit a pronounced reduction in the energy separation of 0-0 and 0-1 maxima. This seems to result from destructive interference of depolarized mode scattering from 0-0 and 0-1 modes.

The coupling constants deduced from the Raman data may be compared with that estimated from the cyclic polyene model. If we employ the CH fragment as an effective mass for a skeletal vibration, then the cyclic polyene model coupling[45] V^K is 24×10^{-5} dynes-amu$^{-\frac{1}{2}}$. The value is 2-20 times greater than those listed in Table I for NiEtio, but is only twice that of intermanifold coupling used to simulate high frequency excitation profiles in CrTPPCl. General agreement between calculated and Raman-derived coupling forces supports the vibronic model. In Chapter V, the coupling contstants are calculated from semi-empirical formulism.

7. Interpretation in Terms of Albrecht's Theory

The effect of a δ variation can be described in the language of Albrecht's A and modified B term[8]. At resonance with the Q state, the A term for Stokes' fundamental scattering is

$$A_{\rho\sigma} = \sum_{Q=Q_x,Q_y} \frac{R_Q^\rho R_Q^\sigma \, {}_G\langle 1|\upsilon\rangle_{QQ}\langle\upsilon|0\rangle_G}{E_\upsilon^Q - E_0^G - \hbar\omega - i\Gamma_Q} \qquad (48)$$

$|v>_Q$ being a vibrational state of the Q manifold. Albrecht's B term is modified in an adiabatic Born-Oppenheimer calculation[17,18], and results in stronger 0-1 scattering of inversely polarized modes of NiEtio. This behavior arises from non-adiabatic coupling via the action of the nuclear momentum operator upon the adiabatic electronic states. If the Herzberg-Teller expansion is employed to evaluate matrix elements of $\partial/\partial Q$ and the transition dipole, we are again within the Longuet-Higgins representation; nevertheless, the difference in resonance enhancement at the 0-0 and 0-1 frequencies persists[17,20]. The modified B term is, excluding the vibrational overlaps and the transition dipoles, the expression in Eq. (47) when there is no displacement of excited state potential energy curves.

In the absence of electronic degeneracy, only totally symmetric modes contribute to the scattering via the A term. However, linear coupling within the degenerate Q states induces displacements of the electronic potential curves along the active normal coordinates. Both a_{1g} and b_{1g}, b_{2g}(Jahn-Teller) modes can couple components of the Q state. Potential curve minima are displaced in the same direction for totally symmetric modes and in opposite directions for Jahn-Teller active modes. This displacement is shown schematically in Fig. 10 for a single b_{1g} mode, as are the initial vibrational wavefunctions for the ground and excited

electronic states potential curves. Now, Franck-Condon overlaps of this non-totally symmetric vibration no longer vanish, and the A term as well as B term will contribute to the Raman intensity. For the case of small displacements displayed in Fig. 10, the Franck-Condon factors of the A term can be seen to satisfy the phase relationship

$$G\langle 1|\upsilon\rangle Q_x Q_x \langle\upsilon|0\rangle_G = -G\langle 1|\upsilon\rangle Q_y Q_y \langle\upsilon|0\rangle_G \tag{49}$$

Therefore, A term components of the scattering tensor A_{xx} and A_{yy} differ inphase. Combining with scattering tensor from B term Eq.(12) , the Raman scattering tensor assumes the pattern

$$\alpha_{\rho\sigma} = \begin{array}{c} \begin{matrix} x & y & z \end{matrix} \\ \begin{bmatrix} A+B & 0 & 0 \\ 0 & -A-B & 0 \\ 0 & 0 & 0 \end{bmatrix} \end{array} \tag{50}$$

and the intensity derived from $\alpha_{\rho\sigma}$ is

$$I_{Raman} \sim (A + B)^2 = A^2 + B^2 + 2AB \tag{51}$$

Due to the Franck-Condon factor, there is a further relative phasing of 0-0 and 0-1 resonance terms of the scattering

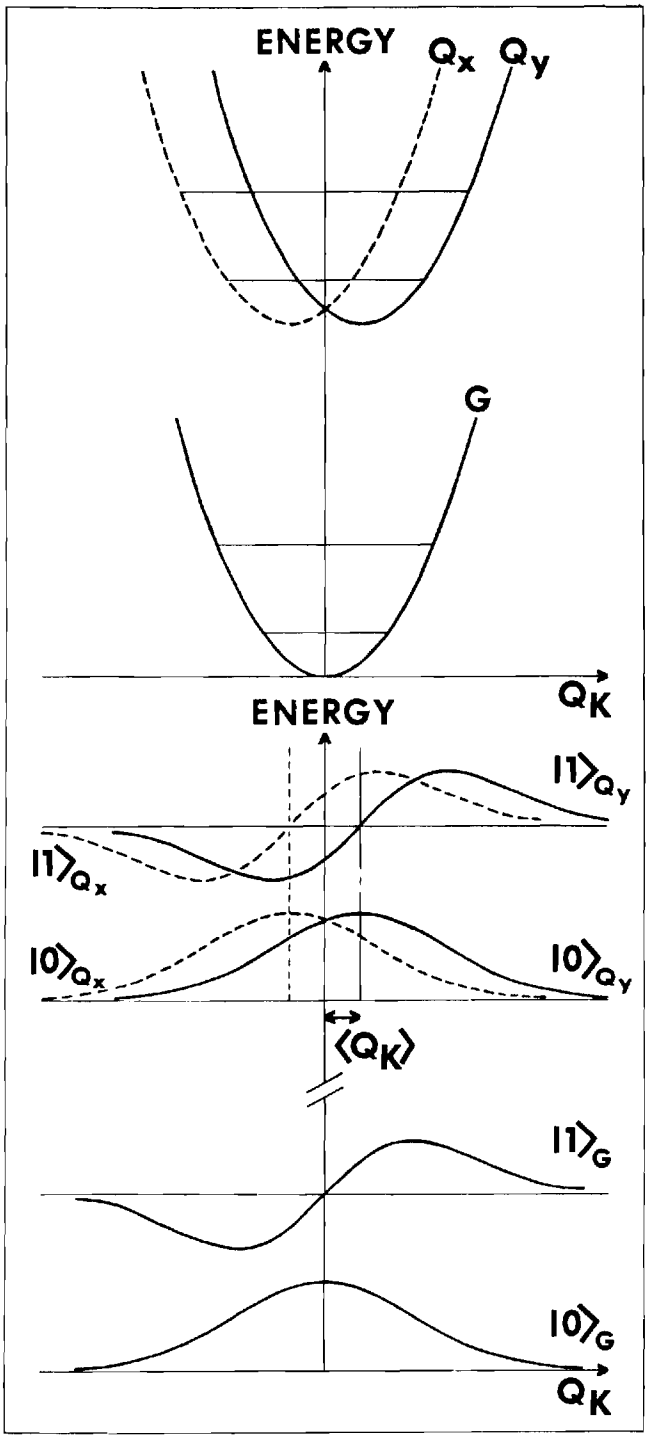

Figure 10. Effect of a Jahn-Teller Distortion on the Q State. The phase relation cited in Eq.(49) can be verified by examination of Franck-Condon overlaps between ground and Q vibrational wavefunctions.

tensor, and this phase differs for A and B contributions. Friedman and Hochstrasser noted a similar phase difference for totally symmetric modes[21]. Thus, for small displacements the interference term 2AB in Eq.(51) may be constructive (destructive) upon 0-0 excitation and destructive (constructive) with 0-1 excitation, depending upon the sign of 2AB. When the four-orbital basis set is chosen, only constructive interference at the 0-0 frequency occurs. To establish the connection between the δ variation and the 0-1/0-0 Raman intensity ratio, we note that as $|\delta|$ increases the Jahn-Teller coupling increases, and consequently, so do excited state origin shifts and Franck-Condon factors in the A term. For $|\delta|$ small, the B term contribution dominates the Raman scattering; larger values of $|\delta|$ yield interfering A and B contributions as the magnitude of the A term grows. Finally, the A term dominates the Raman scattering when excited state displacements are large. Interference between the 0-0 and 0-1 maxima of the profiles also reflects the dominant scattering contribution. Recently, Galluzzi and Garozzo have discussed interference between A and B scattering contributions for totally symmetric vibrations[46].

Interestingly, the depolarization ratio is unaltered irrespective of molecular distortion in the excited state. For example, a b_{1g} mode has a scattering tensor pattern

given by Eq.(50). The McClain tensor invariants are $\delta_F = 0$ and $\delta_G = \delta_H \sim (A+B)$, so ρ_ℓ given by Eq.(45) remains 3/4.

The helping mode phenomenon can also be discussed from the viewpoint of Albrecht's theory. Large origin shifts of excited state potential curves induce additional Franck-Condon contributions to the scattering. Consider the Jth and Kth normal modes. When the excited state origin shifts are small, Franck-Condon factors $_G\langle 0_J 1_K | 0_J 0_K\rangle_Q$ $_Q\langle 0_J 0_K | 0_J 0_K\rangle_G$ and $_G\langle 0_J 1_K | 0_J 1_K\rangle_{QQ}\langle 0_J 1_K | 0_J 0_K\rangle_G$ control the A term contribution to the resonance Raman intensity; other terms from the sum [Eq.(49)] over vibrational states are negligible. However, as the origin shift increases, term with Franck-Condon factors $_G\langle 0_J 1_K | 1_J 0_K\rangle_{QQ}\langle 1_J 0_K | 0_J 0_K\rangle_G$ and $_G\langle 0_J 1_K | 1_J 1_K\rangle_{QQ}\langle 1_J 1_K | 0_J 0_K\rangle_G$ cannot be neglected. Therefore, resonance scattering at the frequency of the Jth mode and its combination with the Kth mode is anticipated, in addition to the usual A terms with resonance as the 0-0 and 0-1 frequency of the Kth mode. In this case, Raman intensity for the Kth mode is helped by additioal A terms involving intermediate vibrational states with one quantum excitation in the Jth mode, and supernumerary maxima in the profile of the Kth mode appear. In a similar way, one can show that the modified B term is augmented by origin shift-induced Franck-Condon contributions. Origin shifts $\langle Q_K\rangle \simeq Q_K^*$ are sufficient for observation of the helping mode phenomenon.

In addition to the results reported for CrTPPCl, Liang et al.[47] have notes additonal maxima in excitation profiles of azulene. Their results are interpreted similarly in terms of the additional Franck-Condon contribution to the A terms.

8. Conclusion

Raman excitation profiles of metalloporphyrins are interpreted within the framework of Longuet-Higgins representation. Restricting the electronic basis to Q and B states and vibronic coupling to linear terms allows a convenient treatment of Jahn-Teller instability in the ^1Q state of NiEtio and CrTPPCl. The resulting dynamical nuclear distortion causes excitation profiles of depolarized modes to exhibit interference between Franck-Condon and intermanifold vibronic contributions to the Raman intensity. A similar influence upon profiles of totally symmetric mode scattering is possible however, inversely polarized vibrations cannot participate in the Jahn-Teller distortion. Their Raman profiles are in accord with nondegenerate perturbative treatment and fully support non-adiabatic modifications to the Albrecht's B term.

A disadvantage of this approach of interpretation is the restriction to two or three modes. The broad helping mode in the 400(p)cm^{-1} excitation profile of CrTPPCl is not

fit well by interaction with only the 1365cm^{-1} vibration, although it is dominant. Likely, additional modes contribute to the resonant states. An increase in the vibrational basis within the constraint of a reasonalbe dimension is readily accommodated by inclusion of symmetry operations on the vibronic Hamiltonian, which allow generation of the partner vibronic wavefunctions[45]. Inclusion of additional modes is not expected to change markedly the parameter set found for NiEtio, but may alter considerably the set advanced for CrTPPCl.

It is interesting to compare excitation profiles in the Q band of NiEtio with those reported earlier for band V of MnEtio[21]. Profiles of the 756 and 1641cm^{-1} depolarized vibrations of the manganese complex are quite disparate from the corresponding Stokes intensities shown in Fig. 6. Instead of strong 0-0 Raman intensity, the MnEtio profiles exhibit weak 0-0 intensity. Unlike the Q band, band V is dipole allowed, perhaps due to the excited state containing the allowed B state and a charge transfer state with a minor admixture of the Q state. We interpreted the stronger 0-1 intensity displayed in depolarized modes of MnEtio in terms of the non-adiabatic contribution to Albrecht's B term, since we assumed that the state corresponding to band V does not exhibit a Jahn-Teller distortion. The 1641(dp) and 756(dp)cm^{-1} profiles do not display marked 0-0 Raman

intensity, which lends credence to this assumption. Indeed, the 0-1/0-0 Raman intensity ratios of the few nontotally symmetric modes for which data is available agree with the predicted ratio, if band V_a is the coupled state. The behavior of band V profiles of polarized modes is now explicable in terms of varying contributions to Raman scattering from Franck-Condon and intermanifold coupling. For these modes either 0-0 or 0-1 scattering dominates. On the other hand, the suggestion of Asher and Sauer[22], that excitation profiles exhibiting more than a single maximum are indicative of an underlying electronic state between bands V and V_a finds no support in this study.

CHAPTER IV

RESONANCE RAMAN STUDIES OF NICKEL ETIOPORPHYRIN I, CHROMIUM TETRAPHENYLPORPHYRIN CHLORIDE, AND COPPER TETRAPHENYLPORPHYRN IN THE SORET REGION

1. Introduction

In the previous Chapter, resonance Raman excitation profiles of nickel etioporphyrin I(NiEtio) and chromium tetraphenylporphyrin chloride(CrTPPCl) have been interpreted as evidence for Jahn-Teller distortion in the visible Q state and for non-adiabatic coupling of this state to the intense Soret(B) band. The vibronic theory of the doubly degenerate, $\pi \longrightarrow \pi^*$ electronic states, using four electronic states, predicts in Soret-excited Raman spectra that (1) totally symmetric modes will be dominant, (2) the depolarized modes of b_{1g} or b_{2g} symmetry (in D_{4h}) that are found to be Jahn-Teller active in the Q state will scatter quite strongly, and (3) the appearance of depolarized mode scattering will correlate with the Q(0-0) absorption intensity.

Raman spectra have been obtained in CrTPPCl[20] and VOEtio[38] on the low frequency side near Soret region. These results have confirmed the predominance of totally symmetric modes. However,in order to examine all predictions carefully, it is necessary to measure Raman spectra with

excitation frequency in the Soret region. In this Chapter, a pulsed laser source is used to obtain the Soret excited Raman spectra of CuTPP, CrTPPCl and NiEtio and the excitation profiles of NiEtio. The results are compared with the prediction outlined in the previous chapter.

2. Methods

A Molectron nitrogen laser(Model UV1000) pumped dye laser(Model DL200) was used as a source for excitation radiation of wavelength near UV region. A set of six different dyes provided by Molectron were used to cover the wavelength range 375-425nm in order to obtain maximum stability in the dye laser output. The nitrogen laser operating at 337.1nm had a peak power of one megawatt and pulse length of 10 nanoseconds. The UV pumping pulse was focused into a dye cell where it was absorbed. The resulting fluorescence covered a broad spectral range from which the lasing output wavelength was selected by a diffraction grating. The nitrogen laser was operated at 10Hz, since a higher repetition rate was unfavorable for a non-flowing dye cell. The output from the dye laser was partially polarized. However, with the insertion of an intracavity polarizer, the polarization was better than 50:1. Typical pulse energy measured at the sample was 0.05mj (Measured with a joulemeter(Molectron Model J302DW) and oscilloscope).

The laser beam was 0.5mm in diameter when it emerged from the dye laser output mirror. A 2mm diameter aperture was used to remove non-lasing light caused by the grating. The laser beam was directed through a set of mirrors and a cylinderical lens of focal length 20cm was used to provide a diffuse line image at the sample, which was placed 2cm from the focal plane.

Scattered radiation was collected in the back scattering geometry[48] (angle between incident and collected radiation was ca. 160°). Collecting optics, spectrometer, and detector were the same as those described in Chapter III. A photomultiplier preamplifier(Molectron Model LP143) was coupled to the output of the phototube. It integrated the anode current pulse and produced as a standard nuclear pulse with an amplitude proportional to the total charge collected. The pulse was then integrated and averaged by a boxcar integrator (Molectron Model LP20). A small fraction of the incident laser beam (~4%, using a glass slide as beam splitter) was processed by a photodiode detector/preamplifier (Molectron Model 141) and was used as the trigger pulse for reference channel of the integrator. The reference channel provided a signal which monitored the power decay of the laser beam. The time constant used was 10 sec. or 30 sec. Spectra were obtained as plots of integrated intensity vs wavenumber.

The sample was ~1mM metalloporphyrin dissolved in carbon disulfide(CS_2) and contained in either a non-rotating, sealed ampoule or capillary. The CS_2 line at $658cm^{-1}$ was used as internal reference. To account for possible preresonance enhancement, an excitation profile of the solvent line was measured vs the $703cm^{-1}$ band of CH_2Cl_2 in a 1:1, CS_2:CH_2Cl_2 mixture.

The excitation profiles obtained for NiEtio were corrected for porphyrin reabsorption[28] as well as the preresonance effect of the reference line and spectrometer response. Assignment of a Raman line as polarized or depolarized was based upon previous assignments measured with cw excitation of these porphyrins in visible region or of VOEtio[38].

Total intensity ($I_{||} + I_{\perp}$) of a Raman line was recorded with partially polarized incident radiation. No significant differences in the excitation profile were found when linearly polarized exciting light was used. Reduction of the incident pulse energy caused a directly proportional reduction in the scattered intensity, showing that spontaneous Raman was observed.

3. Results and Discussion

Figure 11 displays Raman spectra, excited at the respective Soret maxima of NiEtio, CrTPPCl and CuTPP in CS_2.

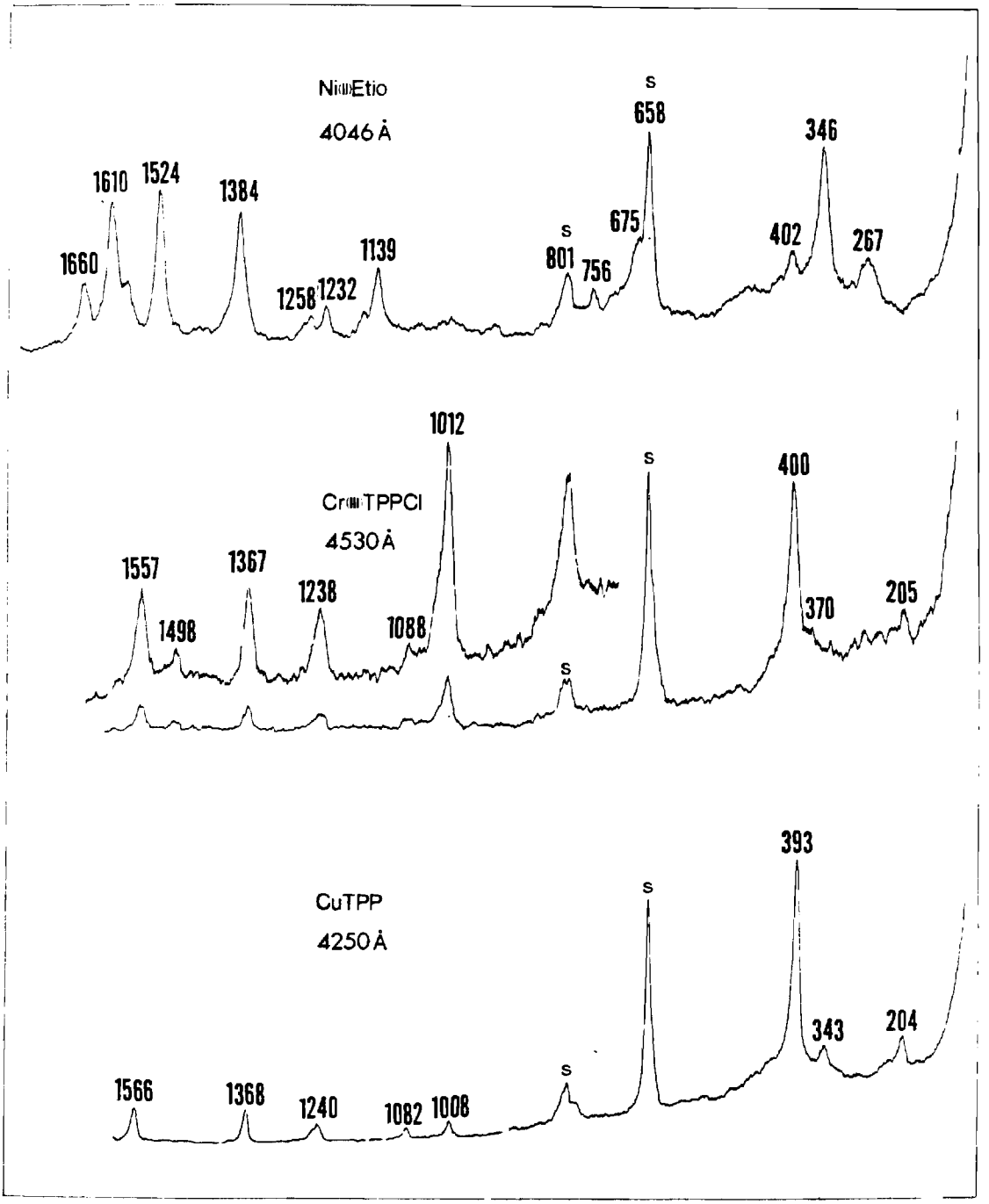

Figure 11. Resonance Raman Spectra of Metalloporphyrins with excitation at the Soret Absorption Maxima. Depolarized modes are 1660, 1258, 1232, and 756cm^{-1} in NiEtio, and 1498 and 1088cm^{-1} in CrTPPCl. Other prominent Stokes lines are polarized. Solvent is CS_2.

In all cases, polarized mode scattering caused by totally symmetric modes is dominant. This is expected since the B transition (Soret) is Franck-Condon allowed. The spectra obtained are comparable with those obtained with an excitation wavelength near the Soret region, e.g. CrTPPCl[20] (with λ_e =457.9nm) and VOEtio[38] (with λ_e=441.6nm).

In the Raman spectrum of NiEtio, depolarized modes at 1660, 1258, 1232 and 756cm^{-1} are observed, as are modes at 1498 and 1088cm^{-1} in the spectrum of CrTPPCl. In contrast no depolarized modes are found in CuTPP. The decrease in depolarized scattering upon B state excitation correlates well with the decrease in Q(0-0) absorption intensity in the order: NiEtio >CrTPPCl >CuTPP (see Figure 12).

The vibronic theory of metalloporphyrin excited states applied to resonance Raman scattering provides an explanation for the proceeding observations. The Q and B states are formed from $\pi \longrightarrow \pi^*$ promotions: $a_{1u} \longrightarrow e_g$ and $a_{2u} \longrightarrow e_g$. If a reference state is chosen in which the a_{1u} and a_{2u} levels are accidently degenerate, then configuration interaction leads to excited states containing equal contributions of the pure configurations[1]. These are

$$|Q_x^0\rangle = [(a_{2u}e_{gx}) + (a_{1u}e_{gy})]/\sqrt{2}$$

$$|Q_y^0\rangle = [(a_{2u}e_{gy}) - (a_{1u}e_{gx})]/\sqrt{2}$$

(52)

$$|B_x^0\rangle = [(a_{2u}e_{gx}) - (a_{1u}e_{gy})]/\sqrt{2}$$

$$|B_y^0\rangle = [(a_{2u}e_{gy}) + (a_{1u}e_{gx})]/\sqrt{2}$$

with $(a_{2u}e_{gx})=[(a_{2u}\bar{e}_{gx})-(\bar{a}_{2u}e_{gy})]/\sqrt{2}$, etc. Phasing of these states and equality of transition dipole intensities to the pure configurations lead to zero electric dipole intensity to $|Q_x^0\rangle$ and $|Q_y^0\rangle$. Coincident with the negligible Q(0-0) intensity, matrix elements of the one electron vibronic operator of the Q_K normal coordinate ($K=b_{1g},b_{2g}$) that couple electronic and nuclear motion in the linear approximation are

$$\langle Q_x^0|\left(\frac{\partial H}{\partial Q_K}\right)_0|Q_y^0\rangle = \langle B_x^0|\left(\frac{\partial H}{\partial Q_K}\right)_0|B_y^0\rangle = 0 \qquad (53)$$

The vanishing of matrix elements in Eq. (53) implies the excited states cannot suffer a Jahn-Teller distortion. Consequently, Raman intensity of depolaried modes in the Q states is derived by vibronic coupling (Albrecht's B term) to the allow B state. In contrast, as the B band is excited, there are no other intense electronic states from which to borrow intensity, and non-totally symmetric scattering via the B term is weak in comparison to scattering by totally symmetric modes. The Raman spectrum of CuTPP exemplifies this case: weak Q(0-0) absorption and no observed depolarized mode scattering in the Soret (Fig. 11).

Suppose that the accidental degeneracy of the a_{1u},a_{2u} orbitals is removed either by interaction with metal orbitals or by an inductive effect of peripheral substituents on the porphyrin ring. The reference states of Eq. (52) will interact via a D_{4h} perturbation[1], H', where the coupling is

$$\langle B_x^0|H'|Q_x^0\rangle = \langle B_y^0|H'|Q_y^0\rangle \equiv \delta \tag{54}$$

New states formed are, e.g.,

$$|Q_x^0\rangle = -\sin\nu|B_x^0\rangle + \cos\nu|Q_x^0\rangle \tag{55}$$

and

$$|B_x^0\rangle = \cos\nu|B_x^0\rangle + \sin\nu|Q_x^0\rangle$$

with $\tan 2\nu = 2\delta/(E_B^0 - E_Q^0)$ and exhibit Q(0-0) dipole intensity proportional to $\sin^2\nu$. Similarly, the matrix elements of Eq. (53) are no longer zero in the rotated electronic basis, and the excited states undergo an origin shift relative to the ground electronic state caused by a dynamic Jahn-Teller distortion involving the depolarized modes. Now, both vibronic and Franck-Condon intensity mechanisms contribute to the Jahn-Teller active modes in the Q state. The phasing between the two sources of intensity and its appearance in Q

state excitation profiles has been discussed in the previous chapter.

According to Eq. (55) both Q and B states will experience distorting forces. In the distorted B states with shifted origins at $\pm\langle Q_K \rangle$ for $|B_x\rangle$ and $|B_y\rangle$, depolarized modes exhibiting Jahn-Teller activity in addition to polarized modes gain Raman intensity by the Franck-Condon mechanism. Indeed, the data shown in Figs. (11) and (12) fully support this assertion: NiEtio has pronounced Q(0-0) absorption and several depolarized modes are noted. CrTPPCl has a weaker Q(0-0) absorption and fewer depolarized modes are seen.

Fig. (12) exhibits B band excitation profiles of selected Stokes lines in NiEtio. Raman intensities are corrected for the significant chromophore absorption and for the slight pre-resonance enhancement of the CS_2 line at $658cm^{-1}$ which serves as internal standard. The FWHM linewidth of ca. $1000cm^{-1}$ in the B state profiles is larger than the $500cm^{-1}$ value found previously for the Q state. Therefore resolution of the Raman scattering maximum at B state is seen only in profiles of the high frequency vibrations. In agreement with the cited predictions of the vibronic theory which are based solely upon a Raman study of the visible band, the $345cm^{-1}$ (p) line is most intense, the $1660cm^{-1}$ (dp) line is about one-fourth the intensity of the

Figure 12. Resonance Raman Excitation Profiles of Selected Vibrations of Ni Etioporphyrin in the Soret Region(upper figure). Lines are drawn through points for purposes of visualization. Absorption spectra are A) NiEtio, B) CrTPPCl, and C) CuTPP in CS_2. Scale factor on the Soret band is referenced to Q band absorption in the visible. Absorptions are not normalized among different porphyrins. $^1Q(0-0)$ maxima are at 17.9kK for NiEtio, 16.6kK for CrTPPCl and 17.3kK for CuTPP.

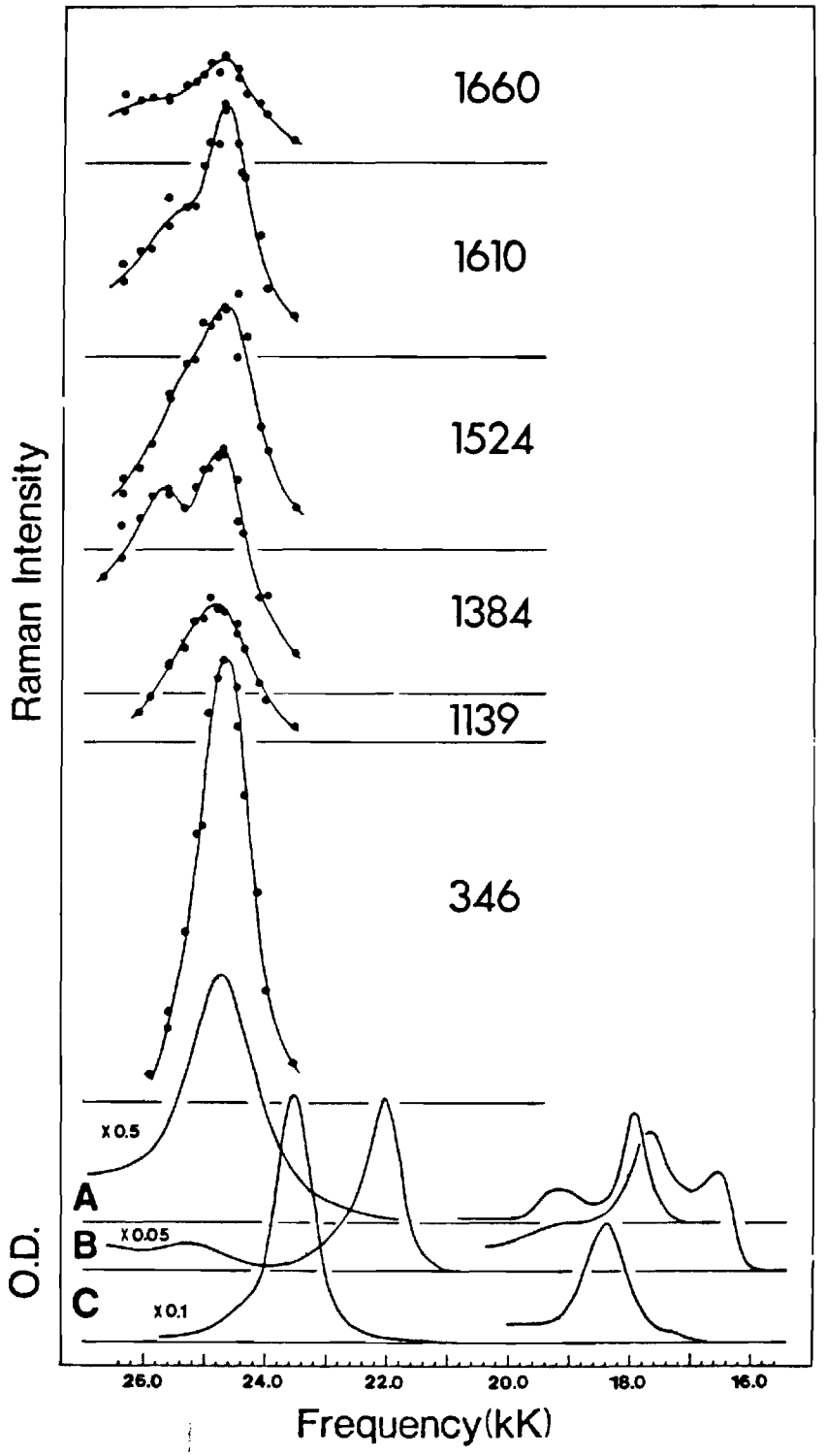
1660
1610
1524
1384
1139
346
Raman Intensity
O.D.
X 0.5
A
X 0.05
B
C
X 0.1
26.0
24.0
22.0
20.0
18.0
16.0
Frequency(kK)

345cm^{-1} band and shows weaker scattering at B(0-1), and no scattering attributed to the antisymmetric (a_{2g}) scattering tensor component is found. In disagreement with the predictions is the weak 756cm^{-1} (dp) scattering and the 2-4 times stronger scattering of the 1140 (p) and 1525cm^{-1} (p) vibrations cf. 345cm^{-1} intensity. The reasons for the discrepancies possibly lie in the quality of the B vibronic wavefunctions derived in previous Chapter, e.g., neglect of higher electronic states or more than two vibrations simultaneously coupling. With the present data at hand, refinement of the electron-phonon coupling strengths is desirable.

In Fig. (13), we note that an effect of focusing the incident beam on a NiEtio sample is quenching of the Raman scattering from most vibrations. Depopulation of the ground state in the laser flash is a likely cause for this observation[50]. In NiEtio and CrTPPCl FWHM linewidths of the Stokes lines are 15-20cm^{-1}, which is larger than the 10-12cm^{-1} set by instrumental conditions and found for CS_2. Peculiar to NiEtio are the following features: (1) the 1384cm^{-1} (p) line shifts to 1375cm^{-1}, and (2) this line does not decrease in intensity with tight focusing. Non-linear processes such as stimulated Raman scattering, direct or transfer scattering[49], and scattering from a metastable, charge transfer state[50] are possible events in this

Figure 13. Effect of Focusing Incident Radiation on NiEtio Resonance Raman Spectra. A) Focused beam, B) sample placed 1 cm from focal plane of cylindrical lens, C) sample placed 2 cm from focal plane. Intensities are not normalized on different runs.

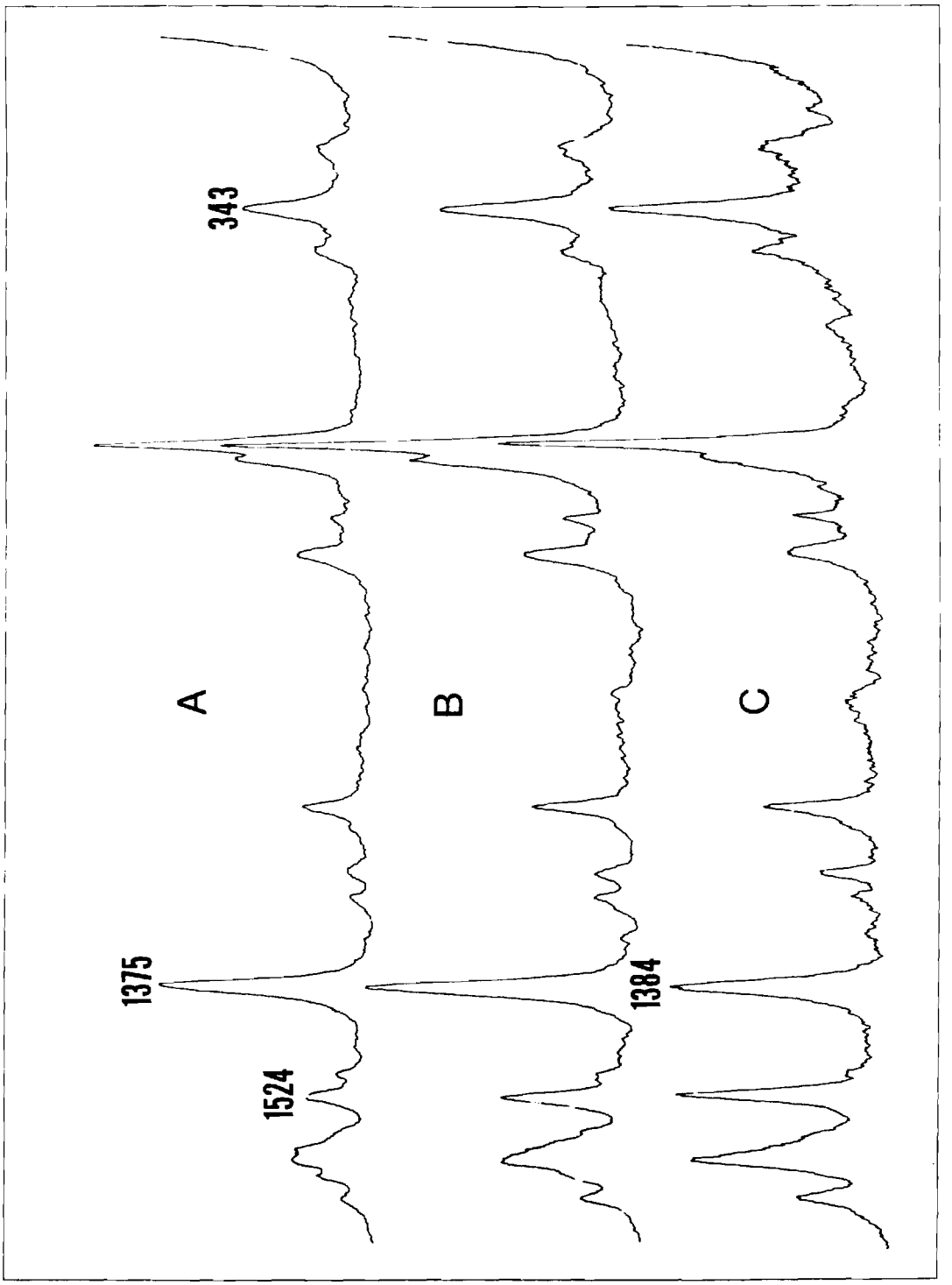
A
B
C
1375
1524
1384
343

non-fluorescing porphyrin. At present, limited data do not warrant speculation if one of these is responsible for the unique behavior exhibited the 1384cm^{-1} line.

CHAPTER V

VIBRONIC COUPLING CONSTANT CALCULATION OF METALLOPORPHYRINS

1. Introduction

The resonance Raman studies of NiEtio, CrTPPCl and CuTPP in previous Chapters have produced interesting results. Especially, in the study of NiEtio and CrTPPCl, some approximate estimation on the vibronic coupling strength between QB and QQ states is made. Although these estimations were made after extensive trial and error fitting various excitation profiles, general agreement has been found between Raman-derived coupling strength with those calculated from the cyclic polyene model[45]. However it is desirable to calculate these coupling constants directly from the properties of molecular wavefunctions and the normal mode of vibrations. These results will provide one method of comparison between observed data and the vibronic model for interpretating resonance Raman spectra.

Lee et al.[51] have outlined the method for vibronic coupling calculation for benzene. They considered only π-electrons and single electronic excitations. For numerical calculations, they used conventional Slater type orbital functions for $2p\pi$ atomic orbitals. Integrals are calculated by Gaussian integral transform methods[52], where

multicenter integrals are calculated exactly. In this calculation, we consider also only π-electrons and single electron excitations. However, we use an even-tempered Gaussian expansion of atomic orbitals[104] and molecular orbitals are obtained from a Pariser-Parr-Pople(PPP) calculation for π-electron system of metalloporphin[3]. All integrals are calculated exactly using formulas derived by Zivkovic, based on Hermite-Gaussian functions[53,54].

In the following sections, the vibronic coupling calculation is outlined and the formulas for calculating various molecular integrals are described. The results are compared with Raman-derived vibronic coupling strength described in Chapter III.

2. Method of Calculation

A. Vibronic coupling

If V represents the interaction energy between electrons and nuclei with

$$V = -\sum_{i} \sum_{m} \frac{Z_m e^2}{r_{im}} \tag{56}$$

where m and i indicate nucleus and electron respectively, then the Hamiltonian for vibronic coupling can be expressed by

$$H'_{VC} = \sum_{\beta} \frac{\partial V}{\partial Q_\beta} Q_\beta + \cdots\cdots$$

$$= \sum_{\beta} \sum_{i} \sum_{m} Z_m e^2 \left(\frac{\vec{r}_{im}}{r_{im}^3} \cdot \frac{\partial \Delta \vec{r}_m}{\partial Q_\beta} \right) Q_\beta + \ldots . \tag{57}$$

where Q indicates the normal coordinate and

$$r_{im} = |\vec{r}_i - \vec{r}_m| \tag{58}$$

with

$$\Delta \vec{r}_m = \vec{r}_m - \vec{r}_m = \hat{i} \Delta x_m + \hat{j} \Delta y_m + \hat{k} \Delta z_m \tag{59}$$

and $\vec{r}$ being the coordinate of the mth nucleus at equilibrium.

The $2p_z$ type Gaussian atomic orbitals ϕ_i are used as atomic basis function for the construction of molecular orbitals. These Gaussian atomic orbitals are kindly provided by Dr. H.Sambe. They are of the even tempered type and four Gaussian type orbitals are fitted by least-squares to repspective Hartree-Fock atomic orbitals of carbon, and nitrogen p orbitals. These orbitals and Pople's atomic orbitals[55] give essentially the same results. For ease in computation, the even-tempered form of Gaussian atomic orbitals are used throughout the calculations. The exponents and coefficients employed are listed in Table II.

Within the π-electron approximation, the molecular orbitals, Ψ_M are expressed as

$$\Psi_M = \sum_m c_m^M \phi_m$$

Table II. p Orbitals for Carbon and Nitrogen

carbon

α = 0.0427550 a.u. β = 0.342326
c_1 = -0.05944476
c_2 = -0.28870492
c_3 = -0.62995620
c_4 = -0.86298140

nitrogen

α = 0.0631498 a.u. β = 0.344283
c_1 = -0.09957703
c_2 = -0.46873552
c_3 = -1.05769860
c_4 = -1.40191192

$$= \sum_m c_m^M \sum_{k=1}^{4} c_{km} z e^{-\alpha\beta^k r^2} \tag{60}$$

where c_m^M are coefficients obtained from PPP molecular orbital calculation of metalloporphin[3].

For single electronic excitation only and considering one mode, the Hamiltonian for vibronic coupling becomes

$$H'_{vc} = - \sum_m (z_m e^2)_o \left(\frac{\partial \Delta \vec{r}_m}{\partial Q_\beta}\right)_o \left(\frac{\vec{r}_i - \vec{r}_m}{|\vec{r}_i - \vec{r}_m|^3}\right)_o Q_\beta \tag{61}$$

Using Eq. (60) and (61), the vibronic coupling matrix elements are

$$\langle \Psi_K | \hat{H}'_{vc} | \Psi_L \rangle$$

$$= - \left\langle \sum_k c_k^K \phi_k \left| \sum_m z_m e^2 \left(\frac{\partial \Delta \vec{r}_m}{\partial Q_\beta}\right)_o \left(\frac{\vec{r}_i - \vec{r}_m}{|\vec{r}_i - \vec{r}_m|^3}\right)_o \right| \sum_l c_l^L \phi_l \right\rangle \tag{62}$$

$$= - \sum_m z_m e^2 \left(\frac{\partial \Delta \vec{r}_m}{\partial Q_\beta}\right)_o \sum_k \sum_l c_k^K c_l^L \langle \phi_k | \frac{\vec{r}_i - \vec{r}_m}{|\vec{r}_i - \vec{r}_m|^3} | \phi_l \rangle$$

Since

$$\frac{\vec{r}_i - \vec{r}_m}{|\vec{r}_i - \vec{r}_m|^3} = \hat{i}\frac{r_{ix} - r_{mx}}{|\vec{r}_i - \vec{r}_m|^3} + \hat{j}\frac{r_{iy} - r_{my}}{|\vec{r}_i - \vec{r}_m|^3} + \hat{k}\frac{r_{iz} - r_{mz}}{|\vec{r}_i - \vec{r}_m|^3} \tag{63}$$

and

$$\frac{\partial \Delta \vec{r}_m}{\partial Q_\beta} = \hat{i}\frac{\partial \Delta x_m}{\partial Q_\beta} + \hat{j}\frac{\partial \Delta y_m}{\partial Q_\beta} + \hat{k}\frac{\partial \Delta z_m}{\partial Q_\beta} \tag{64}$$

the matrix elements can be expressed as

$$\langle \Psi_K | H'_{vc} | \Psi_L \rangle = -\sum_m \sum_{\alpha=x,y,z} z_m e^2 \frac{\partial \Delta \alpha_m}{\partial Q_\beta} \times$$

$$\sum_k \sum_l c_k^K c_l^L \langle \phi_k | \frac{r_{i\alpha} - r_{m\alpha}}{|r_i - r_m|^3} | \phi_l \rangle \tag{65}$$

The calculations of vibronic coupling matrix elements $\langle \Psi_K | H'_{vc} | \Psi_L \rangle$ thus depend on the calculation of the integral which appears on the right hand side of Eq. (65). The integral can be decomposed further into one-center, two-center and three-center integrals.

B. Integral calculation

The formulas used to calculate integrals involving Gaussian functions have been developed by various authors [56,57]. However, formulas for molecular integrals over Hermite-Gaussian functions developed by Zivkovic[53,54] are chosen since conventional differentiation method for

generating integrals of higher Gaussians is tedious and not easy for actual programming. By a choice of appropriate function, which incoporates differentiation in the very definition of the Gaussian function, Zivkovic has shown that explicit formulas can be derived to calculate integrals to any order of Gaussians. Also, based on the derivatives of molecular integrals, formulas for matrix elements of new operators can be derived easily.

A Gaussian function relative to a point A is defined as

$$f(\bar{n},a,\vec{r}_A) = \partial_A^{n_1}\, \partial_A^{n_2}\, \partial_A^{n_3}\, \exp(-ar_A^2) \tag{66}$$

where $\bar{n}$ denotes the set of three numbers: n_1, n_2, n_3;

$$\begin{aligned} \vec{A} &= (A_x, A_y, A_z) \\ \vec{r}_A &= (x - A_x, y - A_y, z - A_z) \end{aligned} \tag{67}$$

and

$$\begin{aligned} r_A^2 &= x_A^2 + y_A^2 + z_A^2 \\ &= (x-A_x)^2 + (y-A_y)^2 + (z-A_z)^2 \end{aligned} \tag{68}$$

Using the definition of the Hermite polynomial

$$H_n(x) = (-1)^n \exp(x^2) \frac{d^n}{dx^n} \exp(-x^2) \tag{69}$$

the function defined in Eq.(66) becomes

$$f(\bar{n},a,\vec{r}_A) = a^{n/2} H_{n_1}[(a)^{\frac{1}{2}}x_A]H_{n_2}[(a)^{\frac{1}{2}}y_A]H_{n_3}[(a)^{\frac{1}{2}}z_A] \times \exp(-ar_A^2) \tag{70}$$

where $n=n_1+n_2+n_3$. For a $2p_z$ orbital, $n_1=n_2=0$, $n_3=1$, and the Gaussian function can be expressed as

$$\frac{1}{2a} f(\bar{n},a,\vec{r}_A) = z \exp(-ar_A^2) \tag{71}$$

These functions are called Hermite-Gaussian functions. Calculation of integrals can then be separated into three steps: (1) differentiation operators are placed in front of the integral sign (2) the remaining integral is calculated by Boys' method[58] and (3) differentiation with respect to the position parameters to give the final result for the integrals.

1. Overlap integral

Using Boys's relation[58], the overlap integral for s function on atoms A and B is

$$\langle aA|bB\rangle = \left(\frac{\pi}{a+b}\right)^{\frac{3}{2}} \exp\left(-\frac{ab}{a+b}\overline{AB}^2\right) \tag{72}$$

where $aA=\exp(-ar_A^2)$ and $\overline{AB}^2=\sum_{x,y,z}(A_x-B_x)^2$. With Eq.(66) and (70), the overlap integral between two Hermite-Gaussian functions becomes

$$\begin{aligned}\langle \bar{n},a,\vec{A}|\bar{n}',b,\vec{B}\rangle &= \int f(\bar{n},a,\vec{r}_A)f(\bar{n}',b,\vec{r}_B)d^3\vec{r} \\ &= \left(\frac{\pi}{a+b}\right)^{\frac{3}{2}} \partial_A^n \partial_B^{n'} \exp\left(-\frac{ab}{a+b}R^2\right) \qquad (73) \\ &= (-1)^{n'}\left(\frac{\pi}{a+b}\right)^{\frac{3}{2}} f(\bar{n}+\bar{n}', \frac{ab}{a+b}, \vec{R})\end{aligned}$$

with $\vec{R}=\vec{B}-\vec{A}$ and $n'=n_1'+n_2'+n_3'$. The overlap of the two functions considered is another Hermite-Gaussian function with vector $\vec{R}$.

2. Nuclear attraction integral

The nuclear attraction integral is defined by

$$\langle \bar{n},a,\vec{A}|\frac{1}{|\vec{r}-\vec{C}|}|\bar{n}',b,\vec{B}\rangle = \int f(\bar{n},a,\vec{r}_A)\frac{1}{|\vec{r}-\vec{C}|}f(\bar{n}',b,\vec{r}_B)d^3\vec{r} \qquad (74)$$

The Boys' relation for 1s orbital is

$$\langle aA|\frac{1}{r-C}|bB\rangle = \frac{2\pi}{a+b}\exp\left(-\frac{ab}{a+b}R^2\right)g(K) \qquad (75)$$

where

$$g(x) = \int_0^1 \exp\ (-x^2t^2)\,dt \tag{76}$$

$$\vec{K} = (a + b)^{\frac{1}{2}} \{\vec{C} - \frac{a\vec{A} + b\vec{B}}{a + b}\} \tag{77}$$

and $K=|\vec{K}|$. By differentiation with respect to Cartesian components of A and B vectors and using formulas for the derivatives of a product of function, Zivkovic has shown that the general formula for the nuclear attraction integral is reduced to

$$\langle \bar{n},a,\vec{A}|\frac{1}{|\vec{r} - \vec{C}|}|\bar{n}',b,\vec{B}\rangle = (-1)^{n'} \frac{2\pi}{a+b} \sum_{k_1}\sum_{k_2}\sum_{k_3}$$

$$\times\left(\frac{b}{(a+b)^{\frac{1}{2}}}\right)^{k} h(n_1,n_1',k_1,-\tfrac{a}{b})h(n_2,n_2',k_2,-\tfrac{a}{b})h(n_3,n_3',k_3,-\tfrac{a}{b})\times \tag{78}$$

$$g(\bar{k},\vec{K})\,f(\bar{n}+\bar{n}'-\bar{k},\ \frac{ab}{a+b},\ \vec{R})$$

where $k=k_1+k_2+k_3$. Each summation over k_1, k_2, k_3 is from zero to n_1+n_1', n_2+n_2', n_3+n_3' respectively. The auxiliary function $h(p,r,s,x)$ and $g(k,r)$ are

$$h(p,r,s,x) = \sum_{\max(0,s-r)}^{\min(p,s)} \binom{p}{i}\binom{r}{s-i} x^i \tag{79}$$

and

$$g(\bar{k},\vec{r}) = \partial_x^{k_1}\,\partial_y^{k_2}\,\partial_z^{k_3}\int \exp\,(-r^2t^2)\,dt$$
$$= (-1)^k \int f(\bar{k},t^2,\vec{r})\,dt \tag{80}$$

In Eq.(69), the Hermite polynomial can be expanded in a series as

$$H_n(x) = \sum_{i=0}^{[n/2]} (-1)^i \frac{n!}{i!(n-2i)!}(2x)^{n-2i} \tag{81}$$

with [n/2]=n/2 or (n-1)/2 for even or odd n. Combining Eq.(70), (80) and (81), auxiliary function g(k,r) becomes

$$g(\bar{k},\vec{r}) = (-1)^k k_1!k_2!k_3! \sum_{i_1}\sum_{i_2}\sum_{i_3} (-1)^i \frac{(2x)^{k_1-2i_1}}{i_1!i_2!i_3!} \times$$
$$\frac{(2y)^{k_2-2i_2}(2z)^{k_3-2i_3}}{(k_1-2i_1)!(k_2-2i_2)!(k_3-2i_3)!} F(\bar{k}-\bar{i},r) \tag{82}$$

with i_1, i_2, i_3 summed over integers between zero and $[k_1/2]$, $[k_2/2]$, $[k_3/2]$ respectively. The function F(i,x) has the form

$$F(i,x) = \int_0^{\infty} t^{2i} \exp(-x^2 t^2)\, dt \tag{83}$$

This integral commonly occurs in molecular orbital calculation with Gaussian basis functions can be calculated accurately by the formulas developed by Schaad and Morrell[59].

3. Vibronic coupling matrix element

In deriving Eq.(57), $\left(\frac{\partial V}{\partial Q_\beta}\right)_0$ is expressed as

$$\left(\frac{\partial V}{\partial Q_\beta}\right)_0 = \left(\frac{\partial V}{\partial \Delta\vec{r}_m}\right)_0 \left(\frac{\partial \Delta\vec{r}_m}{\partial Q_\beta}\right)_0 \tag{84}$$

where

$$d(\Delta\vec{r}_m) = d(\vec{r}_m - \vec{r}_{m_0}) = d\vec{r}_m \tag{85}$$

and

$$\frac{\partial V}{\partial \Delta\vec{r}_m} = \frac{\partial V}{\partial \vec{r}_m} = \hat{i}\,\frac{\partial V}{\partial x_m} + \hat{j}\,\frac{\partial V}{\partial y_m} + \hat{k}\,\frac{\partial V}{\partial z_m} \tag{86}$$

Using Eq.(56) the coupling operator becomes

$$\frac{\partial V}{\partial x_m} = \frac{\partial}{\partial x_m}\left(\sum_i \sum_m - \frac{Z_m e^2}{\vec{r}_{im}}\right)$$

$$= -\sum_i \sum_m Z_m e^2 \frac{(x_i - x_m)}{|r_i - r_m|^3} \tag{87}$$

Eq.(87) shows that the vibronic coupling matrix element can be obtained by taking the derivatives of the matrix elements of the nuclear attraction energy integral with respect to the postion vector $\vec{C}$ in Eq.(78). The results are

$$\partial_{C_x}^{i_1}\partial_{C_y}^{i_2}\partial_{C_z}^{i_3} \langle \bar{n},a,\vec{A}|\frac{1}{|\vec{r}-\vec{C}|}|\bar{n}',b,\vec{B}\rangle$$

$$=(-1)^{n'}\frac{2\pi}{a+b}\sum_{k_1}\sum_{k_2}\sum_{k_3} b^k(a+b)^{(i-k)/2} \times \tag{88}$$

$$h(n_1,n_1',k_1,-\frac{a}{b})h(n_2,n_2',k_2,-\frac{a}{b})h(n_3,n_3',k_3,-\frac{a}{b}) \times$$

$$g(\bar{k}+\bar{i},\vec{K})f[\bar{n}+\bar{n}'-\bar{k},\ \frac{ab}{a+b},\vec{R}]$$

where the auxiliary functions are defined in Eq.(79) and (80).

Alternatively, this integral can be expressed directly in terms of the nuclear attraction integral. The translation of point $\vec{C}$ in a direction $\vec{e}$ by an amount λ is equivalent to translation of points $\vec{A}$ and $\vec{B}$ by the same amount λ but in opposite direction $-\vec{e}$. By analogy, operators ∂_{C_x} and $-(\partial_{A_x}+\partial_{B_x})$ are equivalvent. Eq.(88) can be reexpressed as

$$\partial_{C_x}^{i_1}\ \partial_{C_y}^{i_2}\ \partial_{C_z}^{i_3}\langle \bar{n},a,\vec{A}|\frac{1}{|\vec{r}-\vec{C}|}|\bar{n}',b,\vec{B}\rangle \tag{89}$$

$$= (-1)^{i} \sum_{s_1=0}^{i_1} \sum_{s_2=0}^{i_2} \sum_{s_3=0}^{i_3} \binom{i_1}{s_1}\binom{i_2}{s_2}\binom{i_3}{s_3} \langle \bar{n}+\bar{i}-\bar{s}, a, \vec{A} | \frac{1}{|\vec{r}-\vec{C}|} | \bar{n}'+\bar{s}, b, \vec{B} \rangle$$

For one center integral, with A=B=C, the matrix element is zero. Hence the vibronic coupling matrix element depends on two-center and three-center integrals.

C. Numerical calculation

The molecular orbitals of metalloporphin from PPP type calculation are kindly provided by G.F.Kuipers. The coefficients are listed in Table III with the numbering system within the porphyrin ring shown in Figure 14. For single electronic excitations, only the two highest filled orbitals ($a_{1u}(\pi)$, $a_{2u}(\pi)$) and the two lowest unfulled orbitals ($e_{gx}(\pi^*)$, $e_{gy}(\pi^*)$) are used. These constitute Gouterman's four orbital model[1], in which excited configurations arise from the $\pi \longrightarrow \pi^*$ promotions, $a_{1u}(\pi)$, $a_{2u}(\pi) \longrightarrow e_g(\pi^*)$. These nearly degenerate excited states of E_u symmetry mix by configuration interaction to yield the intense B band at higher energies and the weaker Q band. An early treatment[1] of substituent effects represented by one-electron perturbation required that the one electron operator possess certain symmetries properties. In D_{4h} symmetry, one electron perturbations of a_{1g}, a_{2g}, b_{1g} and b_{2g} can couple B and Q states. The one-electron operators have properties[1] expressed by

Table III. Molecular Orbital Coefficients

	a_{1u}	a_{2u}	e_{gx}	e_{gy}
1	.0000	-.2088	.2150	.0000
2	.0000	-.2088	.0000	.2150
3	.0000	-.2088	-.2150	.0000
4	.0000	-.2088	.0000	-.2150
5	-.3120	.0906	-.1635	-.2382
6	.3120	.0906	-.1635	.2382
7	-.1663	-.1469	.1084	-.2387
8	.1663	-.1469	.1084	.2387
9	-.3120	.0906	.2382	-.1635
10	.3120	.0906	-.2382	-.1635
11	-.1663	-.1469	.2387	.1084
12	.1663	-.1469	-.2387	.1084
13	-.3120	.0906	.1635	.2382
14	.3120	.0906	.1635	-.2382
15	-.1663	-.1469	-.1084	.2387
16	.1663	-.1469	-.1084	-.2387
17	-.3120	.0906	-.2382	.1635
18	.3120	.0906	.2382	.1635
19	-.1663	-.1469	-.2387	-.1084
20	.1663	-.1469	.2387	-.1084
21	.0000	.3832	-.2732	.2732
22	.0000	.3832	-.2732	-.2732
23	.0000	.3832	.2732	-.2732
24	.0000	.3832	.2732	.2732

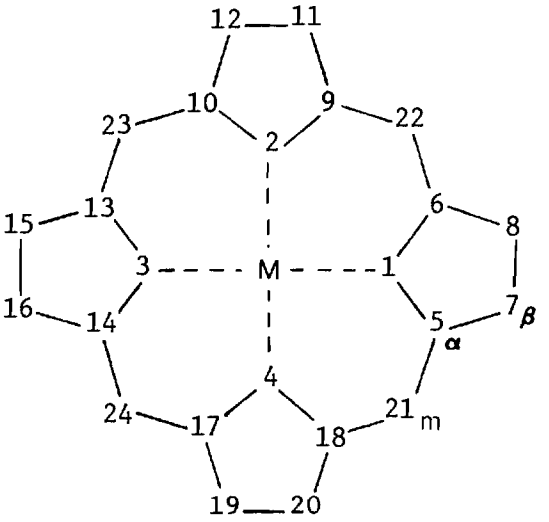

Figure 14. Numbering System of Porphyrin Skeleton.

$$A_{1g} = \frac{1}{2}[-(a_{2u}|a_{2u}) + (a_{1u}|a_{1u})]$$

$$A_{2g} = -(a_{2u}|a_{1u})$$

$$B_{1g} = \frac{1}{2}[(e_{gy}|e_{gy}) - (e_{gx}|e_{gx})] \qquad (90)$$

$$B_{2g} = (e_{gy}|e_{gx})$$

$$A'_{1g} = \frac{1}{2}[(e_{gy}|e_{gy}) + (e_{gx}|e_{gx}) - (a_{2u}|a_{2u}) - (a_{1u}|a_{1u})]$$

respectively where the symbol (a|b) indicates one electron interaction between orbitals a and b. The A'_{1g} term is the additional term that operates within the Q or B states.

In Eq.(60), the atomic orbitals used should be orthogonalized atomic orbitals, since the PPP method is based on the zero differential overlap approximation. The orthogonalized atomic orbitals ϕ^{o}_{m}, can be expressed in terms of Gaussian atomic orbitals ϕ_{m}, by use of the Lowdin transformation[105], as

$$\phi^{o}_{m} = \phi_{m} \vec{S}^{-\frac{1}{2}} \qquad (91)$$

where $\vec{S}$ is the overlap matrix calculated using Gaussian atomic orbitals. Hence the matrix element in Eq.(60) can be reexpressed in terms of orthogonalized atomic orbitals. However for numerical calculation, the Gaussian atomic orbitals are used to calculate the matrix elements. The

results are then transformed into matrix elements in terms of orthogonalized atomic orbitals by multiplication with the appropriate transformation matrix.

For numerical calculation, an effective nuclear charge of 1.50 and 1.00 is used for N and C atoms respectively. All interactions are calculated exactly, with one-center integrals calculated equal to zero. To insure that the integral calculations are calculated correctly, Eq.(88) and (89) have been used in separated calculations. The integrals calculated are exactly the same. Atomic units are used throughout the calculation with mass-weighted Cartesian displacement coordinates. The calculated vibronic coupling constants have units of dynes-amu$^{-\frac{1}{2}}$.

The mass weighted cartesian displacement coordinates $(\partial \Delta \vec{r}_m / \partial Q_\beta)_0$ are generated using Gwinn's program[60] for normal coordinate analysis. The structural parameters used in the calculation are listed in Table IV. Two sets of force constants are used to obtain the displacement coordinates. The first set is the valence force constants used by Sunder and Bernstein[61] in the study of copper octamethylporphyrin(CuOMP). The second set is the modified Urey-Bradley force constants used by Abe et al[62]. in the study of nickel octaethylporphyrin(NiOEP).

3. Results and Discussion

Table IV. Structural Parameters

Bond Distance (Angstrom)

M - N	2.004
N - C_α	1.384
C_α - C_β	1.444
C_β - C_β	1.358
C_α - C_m	1.393
C_β - C_{Me}	1.500
C_β - C_{Et}	1.500
C_m - H	1.090

Bond Angle (Degree)

N - M - N	90.0
M - N - C_α	127.3
C_α - N - C_α	105.4
N - C_α - C_β	110.3
N - C_α - C_m	125.6
C_α - C_β - C_β	107.0
C_α - C_β - C_{Me}	126.5
C_β - C_β - C_{Me}	126.5
C_α - C_m - H	117.9
C_α - C_m - C_α	124.2

Table V and VI list the vibronic coupling constants calculated for CuOMP and NiOEP. The normal mode frequencies obtained in this calculation together with those published by Sunder and Bernstein[61], and Abe et al.[62] are listed for comparision. The frequencies calculated for CuOMP are in good agreement with the published data. The small discrepancy obtained is probably due to a slight variation in the structural parameters being used. In NiOEP, the difference in frequencies is significant. The reason for these large variations is not understood; however, a plot of of the normal modes showed that they are very similar to those published by Abe et al.[62]. This may indicate that the force constants published may not be accurate enough for reproduction. The result is reflected on the large change in the frequencies, but does not affect the overall picture of the normal mode of vibrations.

In CuOMP and NiOEP, we note that in A_{1g} vibrations, the calculated on-diagonal coupling constants are in general smaller in magnitude than the off-diagonal coupling strength. This is anticipated since the shifts in equilibrium geometry of the Q or B states are expected to be small. Only the relative sign between the off- and on-diagonal coupling constants is important. If one of the coupling constant changes sign, the shape of the excitation profile will differ drastically. An overall sign change will

Table V. Calculated Vibronic Parameters for CuOMP

Mode	Frequency (cm^{-1}) from literature[a]	Frequency (cm^{-1}) this calculation	Q-B coupling $V^K \times 10^5$ ($dynes\text{-}amu^{-1/2}$)	Q-Q coupling $V^K \times 10^5$ ($dynes\text{-}amu^{-1/2}$)
A_{1g}	264	261	-2.50	4.77
	357	355	3.59	5.46
	661	653	4.67	4.36
	878	874	-22.65	.03
	1073	1070	-23.03	6.81
	1386	1384	28.27	5.89
	1532	1537	10.32	5.05
	1630	1634	8.80	-1.28
	3072	3073	-2.15	2.15
A_{2g}	295	294	0.04	
	561	545	0.70	
	759	757	7.06	
	986	990	11.66	
	1085	1091	5.51	
	1318	1331	-16.70	
	1488	1503	-12.98	
	1600	1602	23.15	
B_{1g}	185	174	16.58	
	322	321	-7.12	
	692	687	-10.65	
	718	713	2.09	
	1077	1077	-14.46	
	1177	1176	-13.47	
	1458	1456	-11.39	
	1547	1555	8.89	
	1578	1582	16.24	
B_{2g}	174	174	-9.41	
	226	226	18.79	
	519	507	-1.88	
	820	815	9.27	
	1094	1090	5.53	
	1190	1210	5.28	
	1441	1450	15.24	
	1619	1624	2.87	
	3072	3073	3.88	

a) from Ref.61

Table VI. Calculated Vibronic Parameters for NiOEP

Mode	Frequency (cm^{-1}) from literature[a]	Frequency (cm^{-1}) this calculation	Q-B coupling $V^K X10^5$ (dynes-amu$^{-½}$)	Q-Q coupling $V^K X10^5$ (dynes-amu$^{-½}$)
A_{1g}	230	220	4.13	4.28
	326	308	-5.57	-5.33
	655	646	2.77	3.15
	809	793	28.40	-1.87
	1048	1041	-16.49	7.50
	1386	1372	-2.24	3.14
	1517	1513	30.03	7.21
	1591	1568	4.74	1.53
	3072	3076	-2.39	1.99
A_{2g}	289	268	0.15	
	528	512	-0.76	
	723	698	5.83	
	1022	1003	11.50	
	1118	1080	4.44	
	1281	1261	-7.54	
	1409	1395	-12.12	
	1600	1575	-28.44	
B_{1g}	187	181	-15.27	
	299	274	7.72	
	741	726	3.27	
	754	749	24.97	
	1095	1077	12.36	
	1262	1213	10.69	
	1351	1354	-7.79	
	1587	1562	5.16	
	1656	1638	-21.41	
B_{2g}	182	160	4.62	
	232	224	-20.52	
	536	521	-3.59	
	789	750	9.21	
	1016	1005	5.83	
	1157	1151	-6.75	
	1409	1384	7.06	
	1469	1461	-11.53	
	3072	3076	3.89	

a) from Ref.62

not affect the calculated profile, since a change in the direction of the normal mode will reverse the sign in the coupling constants.

The vibronic coupling constants calculated are not very sensitive to the molecular orbital coefficients. A ~5% change in the composition of the molecular orbital coefficients produces a change of ~5% in the calculated vibronic coupling constants. However, for a change in the normal mode composition that alters the directions and magnitude of the Cartesian displacments of each atom, calculated coupling strength will then differ significantly.

Direct comparision between observed Raman intensity and the calculated vibronic coupling constant is inappropriate for A_{1g} modes, since, depending on the admixture between the off- and on-diagonal coupling constants, the calculated excitation profiles will differ. This has been demonstrated in Chapter III in an attempt to fit the 1518(p)cm^{-1} band in NiEtio. The excitation profile of this band shows no 0-0 intensity and weak 0-1 intensity. An attempt to fit the profile with only the off-diagonal coupling gives incorrect result. When excitation profiles are determined only by intermanifold interaction (A_{2g}, B_{1g} and B_{2g} modes), the scattering strength in observed Raman intensities will correlate with the vibronic coupling constants. In CuOMP, large coupling constants calculated in

1331, 1503 and 1602cm^{-1} A_{2g} modes correlate with strong Raman bands observed at 1306, 1411 and 1583cm^{-1}[106].

The overall weakness in calculated coupling constants for B_{2g} modes agrees well with the assignment of all depolarized modes as B_{1g} vibrations, except the calculated lines 1441cm^{-1} in CuOMP and 1461cm^{-1} in NiOEP. A depolarized band has been observed at 1467cm^{-1} in CuOMP. This band has been assigned as a B_{1g} mode by Sunder and Bernstein[106]. However, Kitagawa et al.[107] have assigned a strong band at 1409cm^{-1} in NiOEP to a B_{2g} vibration.

It is interesting to note that in both CuOMP and NiOEP, two low frequency B_{1g}(174, 181cm^{-1}) and B_{2g}(226, 224cm^{-1}) bands have large calculated coupling constants. In solution spectra of both porphyrins, no discernable strong depolarized bands are observed below 300cm^{-1} with Q band excitation. In low temperature Shpolskii spectra, however, intense depolarized bands have been observed in the low frequency region[108,109]. Based on the potential energy distribution calculations of Sunder and Bernstein[61] and Abe et al.[62], these two vibrations primarily involved in $C_\alpha C_m C_\alpha$ and MNC_α deformation modes. Inabiity to observed strong low frequency modes in solution spectra as compared to Shpolskii spectra is not understood.

In conclusion, the calculated vibronic coupling constants are a factor of two to three larger than those

deduced (Table I) from analysis of NiEtio or CrTPPCl excitation profiles. Given the uncertainty in the correct normal coordinate composition in terms of Cartesian displacements of each atom, the neglect of higher electronic state, and the possible inappropriateness in fitting experimental data to just two modes at a time, the agreement is encouraging. It provides a key datum in support of the vibronic approach, in contrast to the adiabatic[116] calculation of Warshel. Had the calculated values been in error by an order of magnitude or more, then the vibronic approach advanced in this thesis might be justly criticized. Additionally, several features of the experimental Raman spectra are reproduced here. These are 1) of the eight a_{2g} fundamentals, only four of these should dominate upon Q(0-0) or Q(0-1) excitation and these will be high frequency modes. 2) Totally symmetric Stokes fundamentals, residing between 800-1550cm^{-1} will be the most intense. This is not completely correct, since the synthetic octaalkyl-poophyrins possess the most intense scattering in the 350-400cm^{-1} band, however, protoporphyrin is a poor scatterer at low-frequencies. Since a major difference between the two skeletons is introduction of two vinyllic groups in protoporphyrin IX, the assumption of a point mass to simulate the alkyl groups may be inadequate. Nontheless, the relative weakness of the highest frequency a_{1g} mode at

ca. 1600cm^{-1} is borne out in the computation. 3) The normal modes used in calculating the results of Table VI, appear superior in accounting for the strong depolarized mode seen between 1620 to 1654cm^{-1} in every octaalkylporphyrin or protoporphyrin IX studied. Perusal of that Table shows strong Q-B coupling with this b_{1g} mode and that at 754cm^{-1}, and in the Raman spectra excited at the Q or B band maxima, these are the mose intense depolarized modes. The next strongest depolarized mode appears at 1228cm^{-1} in NiEtio[29] and there is moderate viboonic coupling predicted for this b_{1g} vibration. With the exception of the 1460cm^{-1} b_{2g} vibration, scattering from b_{2g} vibrations is calculated to be smaller than from b_{1g} vibrations and is observed experimentally[107]. 4) Generally, the off- diagonal Q-B coupling dominates that of the intramanifold Q-Q coupling. Thus excitation profiles of a_{1g} modes will tend to show the strongest maxima at Q(0-0). In conflict with the paramters derived in Chapter III for NiEtio, the relative sign of the 1513 or 1537cm^{-1} a_{1g} vibration is the same for Q-B and Q-Q coupling constants.

CHAPTER VI

RESONANCE RAMAN STUDIES OF CYTROCHROME P-450 AND PROTOCATECHUATE 3,4-DIOXYGENASE

1. Introduction

In Chapters II & III, resonance Raman spectroscopy is described and applied to the study of metalloporphyrins. While some aspects of the theories remain unclear, these do not prevent its use as a spectroscopic tool to probe biological molecules, where selective enhancement of chromophore vibrations is definitely an advantage. In fact, it was the report of resonance Raman spectra for hemoglobin[63,64] and cytochrome c[65,66] that led to the extensive study of metalloporphyrins. Since chromophores are often the active biological site, this allows one to obtain information directly related to structural changes that are pertinent to their biological activities, and is in contrast to normal Raman spectroscopy, which is primarily used to study the secondary and tertiary structures. Detailed reviews of both normal and resonance Raman spectroscopy are available[67-72]. In this chapter, the resonance Raman studies of two biological molecules--cytochrome P-450 and protocatechuate 3,4-dioxygenase are described and serve to illustrate the potentials of resonance Raman spectroscopy for the investigation of biological compounds on a molecular

level.

Cytochromes P-450 are enzymes found in microsomal or mitochrondrial fractions of mammalian liver and adrenal cortex as well as in insects, plants, bacteria and yeast[73]. They belong to a unique class of hemeproteins that catalyze the hydroxylation of a variety of organic compounds through the activation of molecular oxygen. They are characterized by a unique Soret maximum(ca.450nm) when the reduced form is complexed with carbon monoxide. A vast amount of research has been done, resulting in substantial information about the functional aspects of the catalytic reactions[73-74]. Recently, a comparison of MCD spectra between bacterially derived cytochrome P-450cam and a thiolate ligated model compound, Fe(III)(PPIXDME)·$SC_6H_4(p\text{-}NO_2)$, has shown a distinct similarity in the Soret region[110]. In both compounds, a strong negative ellipticity is observed at 400nm. In other species with nitrogen or oxygen ligation, a strong positive ellipticity is observed in this region instead. The similarity between the enzyme and the thiolate model complex in the visible region is less exact. This is probably due to the use of an aromatic thiolate ligand rather than the aliphatic one found in a cysteine residue. In the absence of a definitive X-ray structure of cytochrome P-450, researchers are limited to the approach of synthesizing model compounds[76-78] and

attempting to mimic the spectroscopic properties of the native enzyme. Results from resonance Raman scattering of other hemeproteins have indicated some high frequency bands are sensitive to the geometry about and oxidation state of the heme iron[79,80]. Also, it has been shown that the metal ligand vibration will be selectively enhanced[81,82] when excitation is made within the metal ligand charge transfer band. In light of these observations, a study of cytochrome P-450 by this method is made. Our objectives are to interpret the changes in the anomalously polarized band at ca. 1590cm^{-1} and the oxidation state marker at ca. 1360-1370cm^{-1} in terms of the local environment about the iron. Additionally, we wish to examine the Raman spectrum between 300-400cm^{-1} to ascertain if the ν(Fe-S) vibration[76,91] is enhanced by direct excitation of the z-polarized charge transfer transition.

Protocatechuate 3,4-dioxygenase (PCD) is a non-heme ferric enzyme. It catalyzes the cleavage of protocatechuate acid to β-carboxy cis-cis muconic acid. It has been shown that this enzyme has a molecular weight of 7×10^5 and is composed of eight subunits each of which contains one iron atom and one substrate binding site[89]. The enzyme is red in color and has a broad absorption between 400 and 650nm which is attributable to the ferric iron as the sole co factor, since removal of the iron deactivates the enzyme and

gives a colorless apoenzyme. Extensive studies have been made on its composition and binding parameters with various substrates and inhibitors[83-85]. Thus far, little is known about the coordination sphere around the iron. The absorption maximum is near 460nm and likely arises from a ligand to metal charge transfer transition. Upon addition of the inhibitor, 3-fluoro-4-hydroxybenzoic acid[3-FHB], the maximum is shifted to 420nm. Kinetic measurements by May et al.[83] have indicated 3-FHB acts as a simple competitive inhibitor. Here, resonance Raman spectra for PCD and its complexes with inhibitors are reported. A comparison with recently published studies of Fe(III) transferrin[86-88] is discussed.

2. Materials and Methods

Camphor bound bacterial cytochrome P-450 from Pseudomonas putida and metyrapone were kindly provided by Dr.J.A.Peterson in purified form. For measurement of Raman spectra, 300µl of 0.15mM cytochrome P-450cam in 50mM potassium phosphate buffer, pH 7.4, containing 100mM KCl and 0.5mM camphor, was placed in a small volume rotating cell. The sample was allowed to stay in the laser beam for a period of 3-6 hours before any attempt was made to record the spectra. This treatment reduced fluorescence of the sample. Reduced cytochrome P-450cam was prepared by adding a

minimum amount of sodium dithionite, and the mixture was placed in a capillary where subsequently it was sealed. The metyrapone complex of cytochrome P-450cam was prepared by adding 10µl of 20mM metyrapone into 300µl of 0.15mM P-450cam. Reduced metyrapone complex was prepared similarly by adding sodium dithionite to the oxidized complex.

KNO_3 was added as internal standard(60mM), and excitation profiles were reported as the ratio of the peak height vs that of the NO_3^- band at 1050cm^{-1}. The ratios were corrected for self absorption[28] and spectrometer response. Absorption spectra were obtained before and after Raman spectra were measured so as to confirm that no changes had occured during irradiation.

Protocatechuate 3,4-dioxygenase from Pseudomonas aeruginosa was isolated by the method of Fujisawa and Hayaishi[89] with some modification. Apoenzyme was prepared according to Fujiwara and Nozaki[89]. 3-fluoro-4-hydroxybenzoic acid was synthesized by the method of May et al.[83] and 3-chloro-4-hydroxybenzoic acid was obtained from Aldrich and recrystalized once from water. All materials described above were kindly provided by R.S.Phillips and Dr.S.W.May.

The Raman spectrometer used has been described in Chapter III. Illumination employed discrete lines of the argon ion laser and cw dye laser with sodium fluorescein or rhodomine 6G as dyes.

3. Results

Cytochrome P-450

Resonance Raman spectra of camphor-bound cytochrome P-450, the metyrapone complex of cytochrome P-450 and their reduced forms are shown in Figure 15. In Table VII, their respective Raman peak positions are listed. Qualitative intensities for the Raman bands and their states of polarization: (p), polarized, $\rho_\ell < 3/4$ (dp), depolarized, $\rho_\ell = 3/4$ and (ap), anomalously polarized $\rho_\ell > 3/4$ are reported. Here ρ_ℓ, the depolarization ratio for linearly polarized light with scattered light collected at 90° is the ratio of scattered intensity perpendicular and parallel to the incident radiation. All spectra were taken at 5145Å excitation. The low frequency bands observed in reduced P-450cam·Mp complex is probably due to excess dithionite added. Except in oxidized P-450cam, no attempts were made to obtain spectra at longer wavelength although different vibrational modes may come into resonance, especially in the reduced form where Q(0-0) band resided at 566nm for reduced P-450cam·Mp complex.

Figure 16 shows the excitation profiles for two polarized bands 351 and 756cm^{-1} from 488 to 600nm. The spectral region covers the Q(0,0) visible absorption of P-450cam band. Polarized absorption spectra from a single crystal[117] is shown at the bottom of this Figure. The

Figure 15. Resonance Raman Spectra of A) Cytochrome P-450cam, B) Cytochrome P-450cam·Mp C) Reduced Cytochrome P-450cam, D) Reduced Cytochrome P-450cam·Mp at 5145Å. Each trace consists of a $I_{\parallel}$ (upper) and $I_{\perp}$ (lower) Raman spectrum.

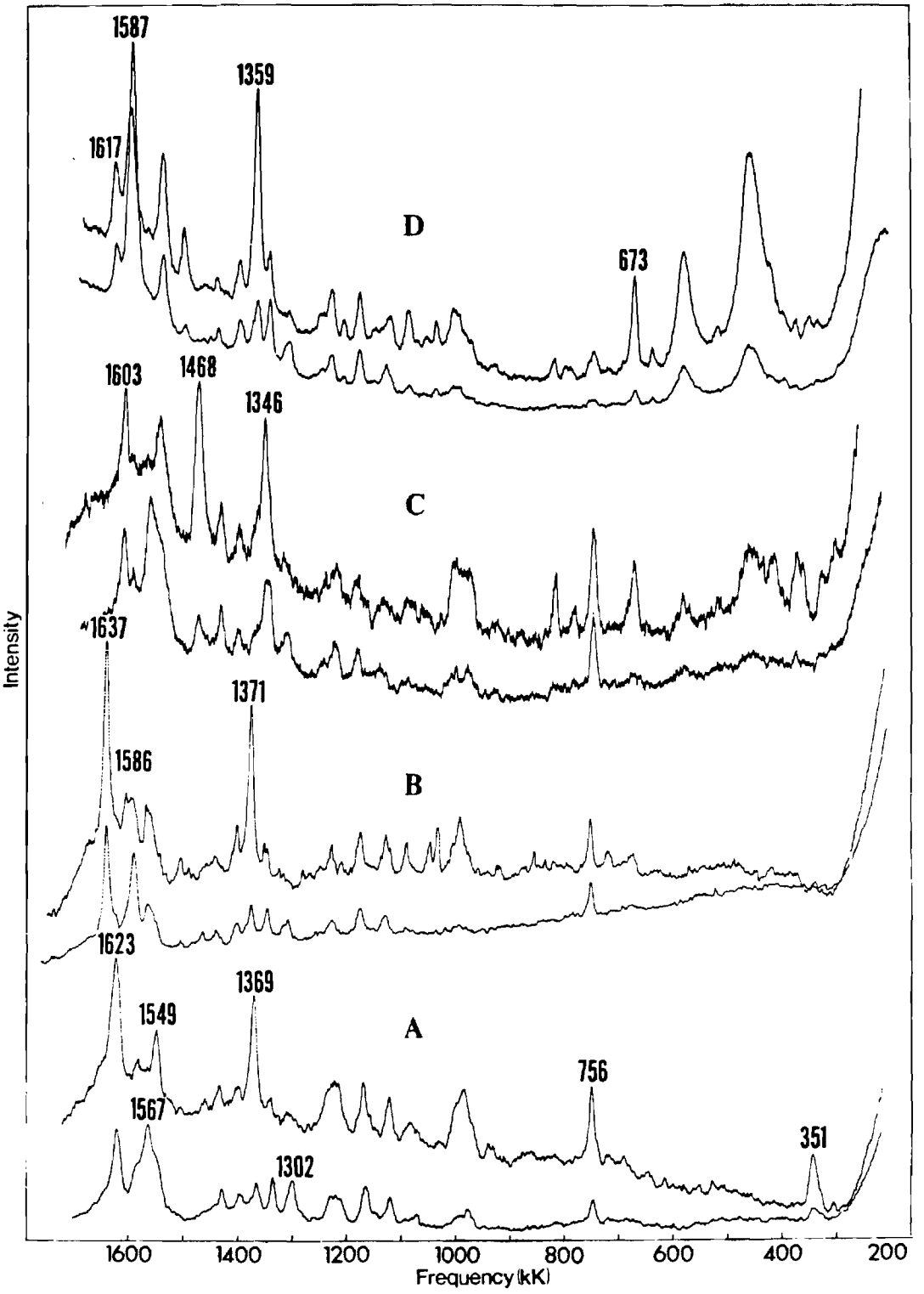
1587
1359
1617
D
673
1603
1468
1346
C
1637
1371
1586
B
1623
1369
1549
A
756
1567
351
1302
Intensity
1600
1400
1200
1000
800
600
400
200
Frequency (kK)

Table VII. Raman Frequencies of P-450cam with Irradiation at 514.5nm.

P-450cam	red-P-450cam	P-450+Mp	red-P-450+Mp
351(m, p)			
	674(m, p)		673(m, p)
756(m, p)	748(m, p)	753(m, p)	747(w, p)
	784(w, p)		
	817(m, p)		819(w, ?)
981(o, p)	978(w, p)	990(m, p)	
1004(o, p)	1003(w, p)		1000(w, p)
		1030(w, ?)	1035(w, ?)
1124(m,dp)		1126(w, ?)	1119(w, ?)
1169(m,dp)	1179(w,dp)	1173(w,dp)	1173(w,dp)
1215(o, ?)	1216(w, ?)		1203(w, ?)
1224(o, ?)		1223(w, ?)	1224(w, ?)
1233(o, ?)			1242(w, ?)
1302(m,ap)	1309(w,ap)	1302(w,ap)	1302(w,ap)
1338(m,dp)		1344(w,dp)	1336(w,dp)
1369(s, p)	1346(s, p)	1371(s, p)	1359(s, p)
1399(w,dp)	1395(w,dp)	1399(w,dp)	1392(w,dp)
1431(w,dp)	1426(w,dp)		1433(w, ?)
	1468(s, p)		1492(m, p)
1549(m,dp)	1539(m,dp)	1560(w, ?)	1532(m,dp)
1567(m,ap)	1556(w,ap)	1586(m,ap)	1587(s,ap)
1584(w,dp)	1588(w,dp)		1590(w, ?)
1623(s,dp)	1603(s,dp)	1637(s,dp)	1617(m,dp)

a) w, weak m, medium s, strong o, overlapping
b) p, polarized dp, depolarized ap, anomalously polarized

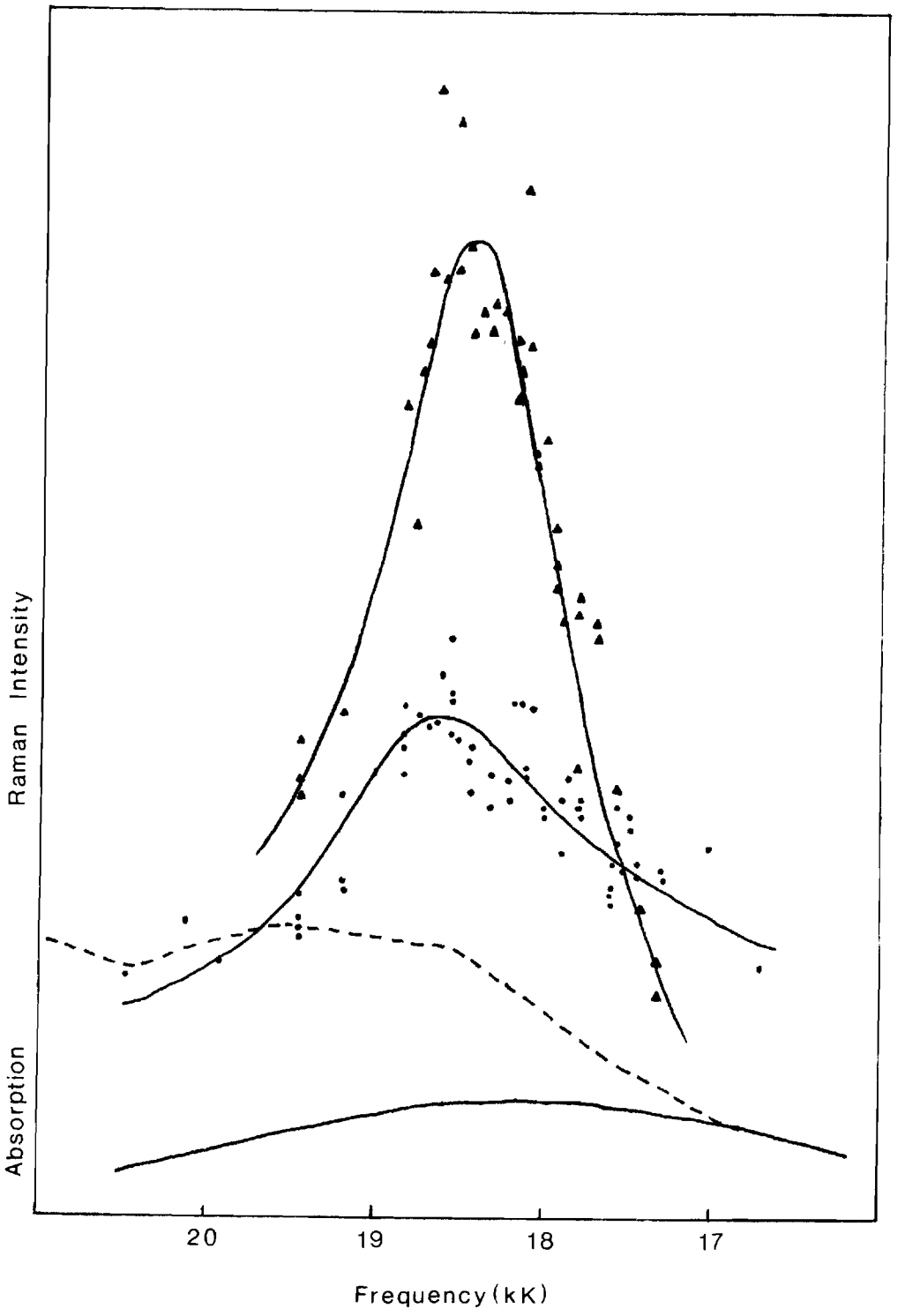

Figure 16. Resonance Raman Excitation Profiles of Lines at 351(•) and 756(▲)cm^{-1} of Cytochrome P-450cam and the single Crystal Polarized Absorption Spectra of Cytochrome P-450cam. (---) Heme-plane (x,y) polarized, (——) z polarized.

excitation profile contours differed slightly with the 351cm^{-1} band having a broader width at half width maximum. Both profiles peaked at 538nm and were close to the Q(0-0) maximum. These profiles were constructed from two different samples. Data points are rescaled such that overlapping region from different samples had the same Raman intensity. The Z polarized absorption maximum appeared at 567nm.

Protocatechuate 3,4-dioxygenase

Spectra of protocatechuate 3,4-dioxygenase(PCD), complexes of 3-fluoro-4-hydroxybenzoic acid, 3-chloro-4-hydroxybenzoic acid with PCD and apo-PCD are compared in Figure 17. Raman bands observed in apo-PCD are typical of a normal, non-resonance protein spectrum[67], with the appearance of a phenylalanine ring mode at 1003cm^{-1}, a broad CH_2 deformation mode near 1450cm^{-1}, and a broad band near 1662cm^{-1}, resulting from the overlapping of the amide I mode with the water deformation mode. The 758cm^{-1} band observed in all spectra is assigned to tryptophan. Additional bands observed in PCD spectrum are listed in Table VIII together with their tentative assignments based on non-resonance Raman data of amino acids. The 981cm^{-1} band in PCD is due to $SO_4^{=}$ which disappeared when the enzymes were purified. Figure 18 displays the non-resonant Raman spectra of 3-FHB, 3-ClHB, and the monopotassium and dipostassium salts of 3-ClHB as well as the solution spectrum of the disodium salt

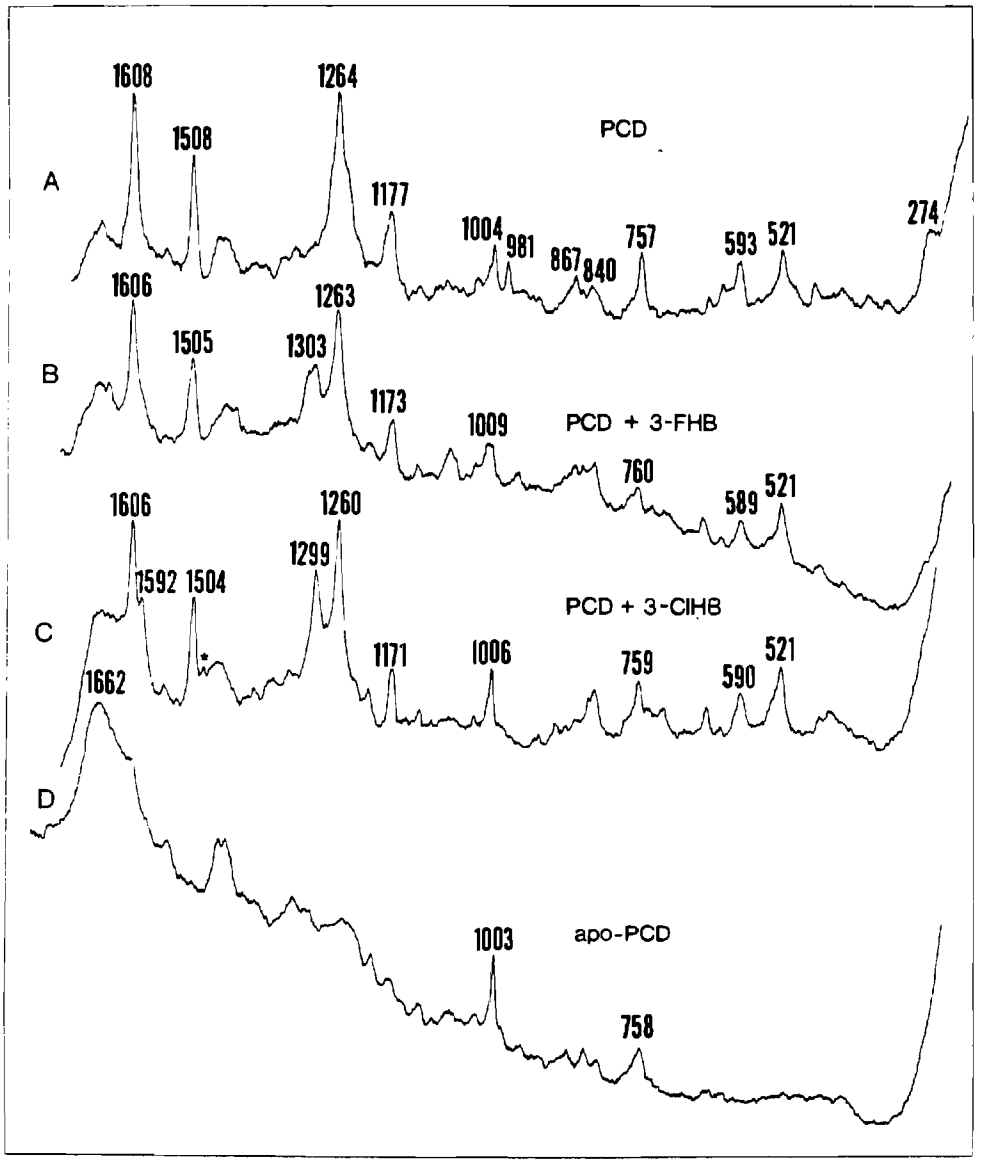

Figure 17. Raman Spectra of Protocatechuate 3,4-Dioxygenase with 514.5nm Radiation. A) PCD in pH 7.5 tris-chloride buffer, B) inhibited complex with 3-fluoro-4-hydroxybenzoic acid, C) inhibited complex with 3-chloro-4-hydroxybenzoic acid. The 1487cm^{-1} band, discussed in the text, is indicated with an asterisk. D) Non-resonant Raman spectrum of the apoenzyme.

Table VIII. Raman Frequencies[a] (cm^{-1}) of PCD, PCD·3-FHB, PCD·3-ClHB, apo-PCD and Their Assignments

PCD	PCD+3-FHB	PCD+3-ClHB	apo-PCD	tentative assignment
274(w,sh)				
521(m)	521(m)	521(w)		
593(m)	589(w)	590(m, b)		
		647(w)		
757(m)	760(w)	759(w)	758(w)	Trp
840(w, b)	833(w, b)	834(w, b)		Tyr
867(w, b)	866(w, b)	834(w, b)		Tyr
1004(m)	1009(m, b)	1006(m)	1003(m)	Phe
1177(m, b)	1173(m, b)	1171(m)		Tyr
	1211(w)	1211(w)		
1250(m,sh)				
1264(s)	1263(s)	1263(s)		Tyr
	1303(m, b)	1299(s)		inhibitor vibration
1460(m, b)	1460(m, b)	1460(m, b)		CH_2-deformation
		1487(w, o)		His(?)
1508(s)	1505(s)	1504(s)		?
		1592(m,sh)		inhibitor vibration
1608(s)	1606(s)	1606(s)		Phe & Tyr
			1662(s, b)	Amide I + H_2O

[a] w, weak; m, medium; s, strong; b, broad; o, overlapping; sh, shoulder

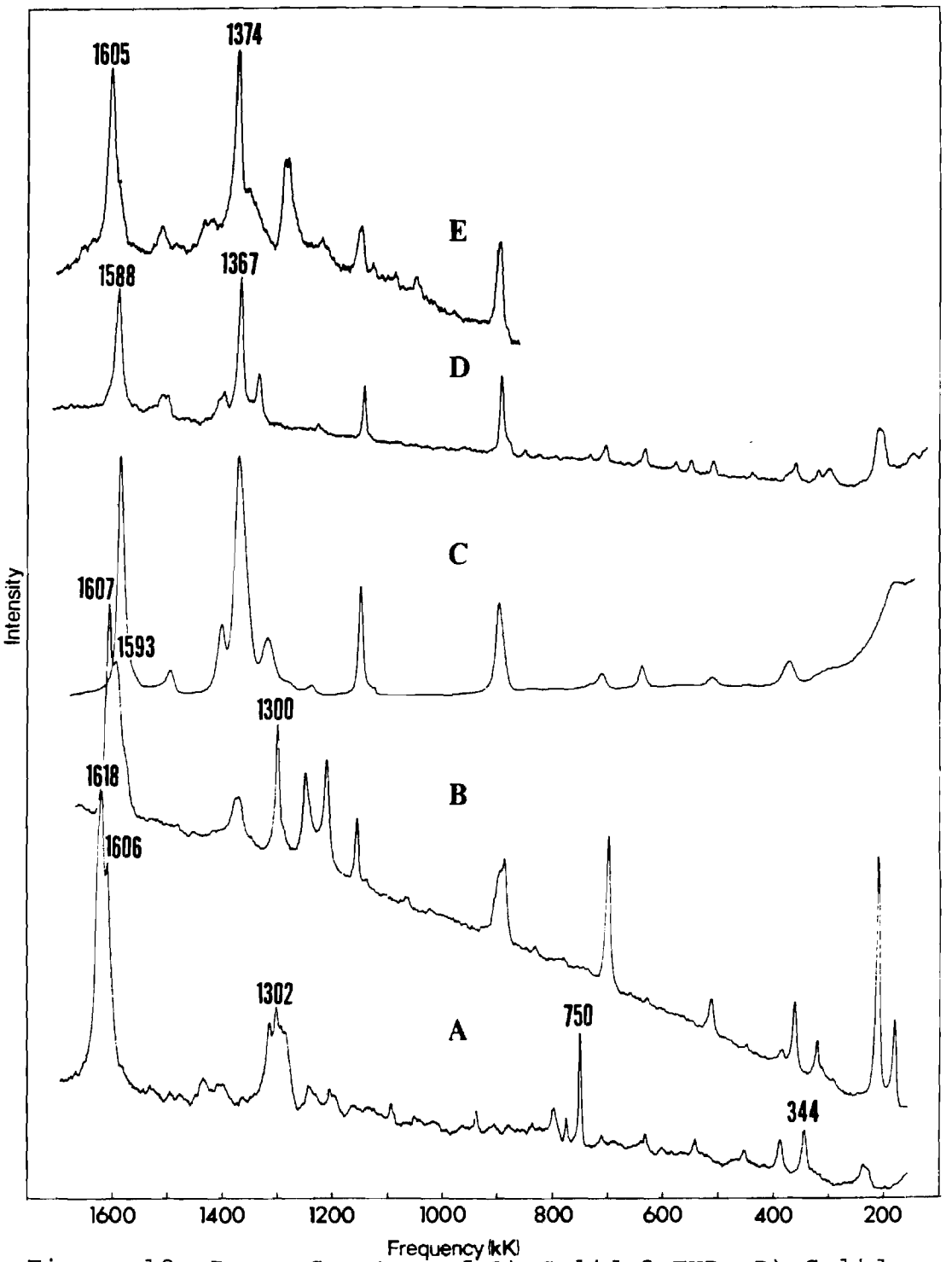

Figure 18. Raman Spectra of A) Solid 3-FHB, B) Solid 3-ClHB, C) Aqueous Di-sodium Salt of 3-ClHB, D) Solid Dipotassium Salt of 3-ClHB, and E) Solid Monopotassium Salt of 3-ClHB.

of 3-ClHB. A listing of all the Raman bands observed are found in Table IX. The main difference between 3-FHB and 3-ClHB is the overlapping bands observed around 1300cm^{-1} in 3-FHB are resolved into distinct bands in 3-ClHB. In 3-FHB-PCD complex spectrum, an extra band not found in PCD is observed at 1303cm^{-1}. This band coincided with a broad overlapping band observed in the solid 3-FHB spectrum. In 3-ClHB-PCD complex, a sharper band is observed at 1300cm^{-1} and an additional band at 1592cm^{-1} appeared as a shoulder on 1606cm^{-1}. These two bands are found in the solid 3-ClHB spectrum also. However a band at 1487cm^{-1} which cannot be assigned to 3-ClHB is also observed.

4. Discussion

Native cytochrome P-450 at ambient temperature contains a mixture of high spin and low spin ferric ion. Upon addition of the substrate, camphor, electron spin resonance results indicate that iron is in high spin form[74]. On the other hand, metyrapone is classified as a type II substrate and induces the conversion of iron in hemeprotein from high spin state to a low spin state[74]. It has been demonstrated that some of the vibrational modes in resonance Raman scattering are found to be sensitive to electronic and structural changes[79,80,92,118]. Using camphor and metyrapone as substrates and with reduction of

Table IX. Frequencies (cm^{-1}) of Substituted Hydroxybenzoic Acids and Their Salts.

3-FHB	3-ClHB	$K^+(3\text{-ClHB})^-$	$(K^+)_2(3\text{-ClHB})^=$
	180(m)		
237(w, b)	210(s)		226(m, b)
344(w)	320(w)		
387(w)	360(w)		
	384(w)		
750(m)			549(w)
776(w)	512(w)		649(w)
798(w)	699(s)		703(w)
938(w)	888(m, o)		878(w,sh)
1093(w)	899(m, o)	898(m)	893(m)
1196(w, o)	1156(m)	1151(m)	1142(m)
1205(w, o)			
1242(w, b)	1212(m)	1282(m, o)	
1288(m, o)	1250(m)	1288(m, o)	1333(m)
1302(m, o)	1300(s)	1353(w,sh)	1367(s)
1313(m, o)	1374(m, b)	1374(s)	1397(w)
1431(w)			
	1577(w,sh)		1502(w, b)
	1593(m,sh)	1587(w,sh)	
1606(m, o)	1607(s)	1605(s)	1588(s)
1616(s, o)			

a) w, weak m, medium s, strong o, overlapping
sh, shoulder
b) solid samples

Fe(III) to Fe(II), a set of distinct Raman bands so obtained can be used to probe the structural parameters(oxidation state, spin state, metal displacement distance) characteristic of P-450 and compared with those from other hemeproteins.

In P450cam (ferric,high spin), the polarized band at 1369cm^{-1} is shifted 5cm^{-1} lower than the normal value of 1374cm^{-1}. No discernable band is observed around the Band II region of 1482cm^{-1}[80]. This may due to the excitation frequency used in this study being on the high frequency side of Q(0,0) band of the absorption spectrum. However a band at 1488cm^{-1} is observed when excitation is made within the Soret region[93]. The anomalously polarized band observed at 1567cm^{-1} is low in frequency when compared with the typical high spin value of 1572cm^{-1}. From the correlation of Spaulding et. al.[118], the frequency implies a 2.03Å distance from the pyrrole nitrogen to the center of the porphyrin ring. The last marker band at 1623cm^{-1} is also lower than the normal value of 1632cm^{-1}. It is worth noting that in catalase[92], ap and dp lines are observed at 1567 and 1624cm^{-1}. In the low frequency region, 351 and 756cm^{-1} are the only two distinct bands observed in P-450cam. Champion and Gunsalus[91] have tentatively assigned 351cm^{-1} as Fe-N vibration, based on the assumption that a charge transfer band is in the neighborhood of the excitation

wavelength(3638Å). Indeed z-polarized absorption has been observed at 567 and 323nm in single crystal polarization study[117]. However, these two transition are of out of plane type. This implicates that direct axial ligand type charge transfer cannot be ruled out. In this case, 351cm^{-1} may well be an axial ligand-metal type vibration.

In P-450-Mp complex(ferric,low spin), bands observed at 1371,1560,1586, 1637cm^{-1} are in general lower than those of typical porphyrin bands. No polarized band is observed around 1500cm^{-1}. The 1586(ap)cm^{-1} line is consistent with an in-plane iron, as expected for metyrapone bound to iron.

In reduced-P450(ferrous,high spin), the spectrum obtained is similar to Ozaki et al.[94] with 4880Å excitation. A strong polarized band is observed at 1346cm^{-1}. Since this is the only strong polarized band observed between 1200-1450cm^{-1}, it can be grouped as a Band I type and shound be an oxidation state marker band. A typical Band I type for high spin Fe(II) is found as 1355cm^{-1}. It has been pointed out by Brunner and Sussner[102] that this band is sensitive to charge at the center of the porphyrin ring. The anomaly found may indicate an unusual ligand iron interaction in the axial position. Champion et al.[95] have found chloroperoxidase possesses a similar Raman spectrum to that of cytochrome-P450. Although these two enzymes have different functional properties, Raman spectra indicate the

coordination around heme moiety is very similar with a bound mercaptide in both enzymes. This is also confirmed by the similarity in optical absorption, electron spin resonance and Mossbauer spectroscopy[96].

In reduced P-450 metyrapone complex(ferrous,low spin), the spectrum obtained is similar to that of Ozaki et al.[96] A close similarity to that of ferrous cyto-b , where two histidyl imidazoles are coordinated to the heme moiety, has been pointed out by them. The Raman bands positions of red-P-450-Mp are typical of a low spin ferrous hemeprotein.

Resonance Raman excitation profiles of the 351 and 756cm^{-1} Stokes fundamentals in P-450cam

The 351(p)cm^{-1} band, whose excitation profile is exhibited in Fig. 16 is the most pronounced band in the low frequency Raman spectrum. By comparision, the 756(dp)cm^{-1} band loses intensity more rapidly when the excitation wavelength is to the red of the major Q band absorption at ~18.5kK however, the width of the 351cm^{-1} profile is greater than that of 756cm^{-1} profile. It is believed that the 756cm^{-1} vibration is a typical in-plane porphyrin vibration, which couples the Q and B state in P-450 in a manner analogous to that found for NiEtio in Chapter III. As such, if the 351cm^{-1} profile followed the Z-polarized absorption, while the 756cm^{-1} behaved differently, then this difference could provide evidence that the 351cm^{-1} Raman intensity arose, not from the Q band absorption, but from the charge

transfer state. Thus, one could assign the 351cm^{-1} band to an out-of-plane stretch of Fe-S . The assignment would depend upon the observation that (Fe-S) vibrations appear at this frequency in rubredoxin(311cm^{-1})[119,120]. The data in Fig. 16 are ambiguous in this regard. For example, the profiles of both Raman lines peak approximately at the same position, and this finding would suggest that the 351cm^{-1} vibration is coupling to the $\pi \longrightarrow \pi^*$ transition. However, this similarity may reflect also the approximate coincidence of absorption maxima, shown in Fig. 16, of both transitions.

The appearance of the 351cm^{-1} band, in itself, cannot be construed in favor of a ν(Fe-S) assignment. It is known that ferric protoporphyrin IX chloride has a ring mode at this frequency[121]. In Q band spectra of MetHbF$^-$ or OH$^-$, ferric mesoporphyrin IX, or spectra of Mb, Hb, and cytochrome c, excited at 441.6nm, a prominent 350(p)cm^{-1} Raman line is found. The cited species are known to contain no axially ligated cysteine.

The present study does not permit us to assign a porphyoin or Fe-S$^-$ vibration to the 351cm^{-1} band. However, in a study of P-450cam, excited at 365.1nm, Champion and Gunsalus have assigned this band to a porphyrin ring mode[91]. They fail to consider that their excitation frequency is close to a second charge transfer band situated at 323nm. It is unlikely that the Raman band observed by

them gains intensity from the Soret band, located 2000cm^{-1} to the red. Indeed, the Soret-excited profile of the authentic ring mode in NiEtio, shown in Fig. 12, obviates the Soret as a source of intensity in the Champion and Gunsalus experiment. With the recent acquistion of a flash lamp pumped dye laser, it is proposed that examination of the visible and 320nm region can provide the necessary data to resolve the ambiguity. If the 351cm^{-1} band appears strongly in both regions, but not in the Soret(N_2 laser excitation), then the Raman scattering intensity correlates with the charge-transfer transition, and it may be assigned to ν(Fe-S).

It is worth noting that in reduced P-450cam, and metyrapone complexes of either the oxidized or reduced forms, no 351cm^{-1} band is observed. Since the charge transfer transition decreases in intensity and shifts to the red upon imidazole binding[122], and in the reduced complex is absent, the failure to observe the 351cm^{-1} Raman line is consistent with but not proof of the assignment to ν(Fe-S).

Protocatechuate 3,4-dioxygenase

Ferric iron has been found as a sole cofactor for intradiol type oxygenases like PCD. It is responsible for the epr signal[97] as well as the visible absorption spectrum of the enzyme. Que et al.[97] show that the Mossbauer data rules out rubredoxin-like tetrahedral sulfur

coordination. To account for the absorption near 460nm, which arises from ligand to metal charge transfer transition, they speculate that tyrosine as the most likely candidate for this charge transfer band. The Mossbauer parameters are similar to those of deoxyhemerthyrin suggesting that iron may be in a similar environment. X-ray structural studies on myohemethyrin[98] and methemerthyrin[99] implicate histidine and tyrosine residues for iron binding. Dunn et al.[100] did not observe any Raman bands in deoxyhemerthyrin. This is probably due to the concentration they used(3.2mM) is much too low for a non-resonant Raman measurement as it has no absorption in the visible.

PCD Raman spectra (Fig. 17) obtained in this study clearly indicate that tyrosine is in proximity to the iron. The characteristic tyrosine-related vibrations 840, 867, 1177, 1264, and 1608cm^{-1} are resonance enhanced when the excitation frequency(514.5nm) is within the charge transfer transition involving iron. Raman bands at 758,1004 and 1662cm^{-1} found in PCD and apo-PCD are typical of a normal protein spectrum[67]. However, in PCD, low frequency bands at 521 and 593cm^{-1} cannot be assigned directly to any typical amino acids residue vibration. Tomimatsu et al.[86] have also observed low frequency bands (510 and 570cm^{-1}) in Fe(III) ovotransferrin. These vibrations may correspond to

ring deformation modes of a chelated iron with a contribution from (Fe-O)[111]. The strong 1508cm^{-1} band is also observed in Fe(III) transferrin and Cu(II) transferrin resonance enhanced Raman spectra. Gaber et al.[88] have assigned this band to a symmetric ring stretch of phenol based on the resonance Raman spectrum of Fe(III) complex of ethylenediamine di(o-hydroxyphenylacetate),EDDHA, a model compound for Fe(III) transferrin. However, the possibility of coordination with an imidazole type ligand cannot be ruled out. In Cobalt(II) complexes of imidazole(Im)[103], vibrations at 1163, 1273, 1489cm^{-1} are assigned to ring vibration of imidazole in Cobalt(II) complex with imidazolate anion, while 1173, 1258 and 1495cm^{-1} are assigned to ring vibration of imidazole in Cobalt(II) complex with imidazole. This can be compared directly with 1177, 1264 and 1508cm^{-1} observed in PCD. However, no marked shifts are observed in Raman spectrum of a PCD sample incubated with 50% $D_2{}^{18}O$ for one week. Assignment of the 1508cm^{-1} Raman band to an imidazole ring vibration is unlikely as noted by Gaber et al.[88], since imidazole vibrations at 1495 and 1535cm^{-1} will shift to 1496 and 1508cm^{-1} with N_1 deuteration and to 1454 and 1508cm^{-1} respectively upon further exhange at C_2[112]. Also, the assignment of low frequency modes to ν(Fe-OH_2) is tentatively excluded.

Addition at pH 7.5 of 5mM 3-fluoro-4hydroxy-benzoic acid (3-FHB, K_I=0.6μM) or 3-chloro-4-hydroxybenzoic acid (3-ClHB, K_I=4μM) to PCD assures saturation of the binding site by these inhibitors 83 . In Fig. 17, the appearance of a broad line at 1303cm^{-1} in PCD 3-FHB and narrower lines at 1592 and 1299cm^{-1} in PCD-3ClHB is caused by resonance enhanced scattering of the bound inhibitors, since these vibrations are found in the unbound inhibitors(Fig. 18). It is suggested that enhanced Raman scattering of tyrosine skeletal modes arises from the $p\pi(Tyr) \longrightarrow d\pi^*(Fe(III))$ nature of the visible charge transfer[88]. Similarly, in the complexes with inhibitors, tyrosine and inhibitors levels presumably act as donors to Fe(III) in the excited states. It is notable that the 1592cm^{-1} of 3-ClHB is derived from the ν_{8a} ring stretch of ortho di-substituted benzene, while vibrations at ca. 1300cm^{-1} appear at frequencies associated with a ν_{14} ring stretch or ν_3 CH deformation[113]. However, the appearance of inhibitor mode scattering in PCD does not imply ligation at iron, rather, it is evidence that 3-FHB or 3-ClHB molecules are situated in the vicinity of Fe(III) in a geometrical arrangement that either provides direct dipole strength to the charge transfer transition or permits significant $p\pi$ overlap between the inhibitor molecule and aromatic residues say, tyrosine, which participate in the charge transfer transition.

The novel suggestion that active site binding of the inhibitor is not via iron ligation by an ionized hydroxyl function arises from comparision between the enhanced Raman frequency of PCD 3-ClHB at 1299cm^{-1} with lines found at 1300cm^{-1} in the solid sample of 3-ClHB; at 1353, 1288, and 1282cm^{-1} in the solid sample of the monopotassium salt of 3-ClHB; and at 1333 and 1367cm^{-1} in the solid sample of the dipotassium salt of 3-ClHB or its disodium salt(aq.). Thus, Raman lines situated between 1200-1300cm^{-1} are clearly sensitive to carboxyl or hydroxyl ionization, and it follows that the agreement in the position of this band in the fully protonated forms of either 3-ClHB or 3-FHB and their respective PCD complexes is compelling evidence against ionization of the p-hydroxyl function. For this reason we rule out the formation of an Fe(III)-O bond. Indeed, the pH dependence of 3-FHB binding to PCD suggestes also preferential binding of the protonated phenolic function[83]. On the other hand, specificity studies favor a picture in which a strong ionic interaction occurs between the carboxylate and a PCD cationic site[87,114]. If this be the case, then the bound inhibitor would exhibit vibrational frequencies, not of the free 3-ClHB monoanion, but that of the protonated form.

The Raman spectrum of PCD 3-ClHB displays an additional peak at 1487cm^{-1} that cannot be assigned to

3-ClHB. In view of its proximity to the ring deformation + $\nu(C_2\text{-}H)$ mode of imidazole(ImH) reported[112] at 1490cm^{-1}, at 1511cm^{-1} in $Co(ImH)_4(ClO_4)_2$ and at 1505cm^{-1} in $Co(ImH)_2Cl_2$, it is possible that a histidyl residue is near the catalytic site. This tentative assignment can be tested by the appearance of a shift in the 1487cm^{-1} band upon deuteration at C_2 in histidine, assuming the residues near the catalytic site are not buries and thus, undergo deuterium exchange.

The present data cannot be construed as evidence aginst iron ligation in substrate of PCD, all of which contain the o-dihyroxy-phenyl grouping. For such metabolized compounds, direct ligation of phenolate to iron is mechanistically attractive, since it would fovor ketonization and activation of the ring towards oxygen attack[115]. Raman studies on E·S and E·S·O_2 complexes are expected to provide comparisons at the molecular level between substrate and inhibitor binding.

BIBLIOGRAPHY

1. M.Gouterman, J. Chem. Phys., 30, 1139 (1959).

2. M.Gouterman, J. Mol. Spectrosc., 6, 138 (1961).

3. C.Weiss, H.Kobayashi, M.Gouterman, J. Mol. Spectrosc., 16, 415 (1965).

4. H.Kobayashi, J. Chem. Phys., 30, 1362 (1959).

5. H.A.Kramers and W.Heisenberg, Z. Physik., 31, 681 (1925).

6. P.A.M.Dirac, Proc. Roy. Soc. (London), 114, 710 (1927).

7. G.Placzek, in "Rayleigh and Raman Scattering", UCRL Trans. 526(L), from "Handbuch der Radiolgie" ed. E.Marx, Akademische Verlagsgesellschaft, Leipzig. 6, P.209 (1934).

8. A.C.Albrecht, J. Chem. Phys., 34, 1476 (1961).

9. J.Tang and A.C.Albrecht, in "Raman Spectroscopy", ed. H.C.Szynmanski, Plenum Press Inc., New York., Vol.2, P.33 (1970).

10. J.Behringer, in "Molecular Spectroscopy", ed. B.F.Barrow, D.A.Long and D.J.Miller, (Specialist Periodical Reports) The Chemical Society, Vol.2, P.100 (1974).

11. E.B.Wilson Jr., J.C.Decius and P.C.Cross, Molecular Vibration, McGraw Hill, 1955.

12. H.M.McClain, J. Chem. Phys., 55, 2789 (1971).

13. J.Behringer, in "Raman Spectroscopy", ed. H.A.Szynmanski, Pleum Press Inc., New York., Vol.1, P.168 (1967).

14. W.Heitler, the Quantum Theory of Radiation, Clarenden Press, Oxford, 3rd Edn., 1954.

BIBLIOGRAPHY (Continued)

15. G.Herzberg and E.Teller, Z. Physik. Chem., B21, 410 (1933).

16. M.Mingardi and W.S.Siebrand, J. Chem. Phys., 62, 1074 (1975).

17. G.J.Small and E.S.Yeung, Chem. Phys., 9, 379 (1975).

18. J.M.Friedman and R.M.Hochstrasser, Chem. Phys., 1, 457 (1973).

19. M.Z.Zgierski, Chem. Phys. Lett., 36, 390 (1975).

20. J.A.Shelnutt, D.C.O'Shea, N.T.Yu, L.D.Cheung and R.H.Felton, J. Chem. Phys., 64, 1156 (1976).

21. J.M.Friedman and R.M.Hochstrasser, Chem. Phys. Lett., 32, 414 (1975).

22. S.Asher and K.Sauer, J. Chem. Phys., 64, 3115 (1976).

23. M.S.Child, Mol. Phys., 3, 601 (1960).

24. M.Tsuboi, A.Y.Hirakawa and S.Muraishi, J. Mol. Spectrosc., 56, 146 (1975).

25. K.Kaya, in "Proceedings of the Fifth International Conference on Raman Spectroscopy" ed. E.Schmid, J.Brandmuller, W.Kiefer, B.Schrader and H.Schrotter, Schulz, Frieberg, P. 237 1976.

26. M.H.Perrin, M.Gouterman and C.L.Perrin, J. Chem. Phys., 50, 4137 (1969).

27. H.Hamaguchi, I.Harada and T.Shimanouchi, Chem. Lett., 1045 (1974).

28. T.C.Strekas, D.H.Adams, A.Packer and T.G.Spiro, Appl. Spectrosc., 28, 324 (1974).

29. R.C.C.Chang, Ph.D. Thesis, Georgia Institute of Technology, 1976.

30. J.M.Friedman and R.M.Hochstrasser, J. Am. Chem. Soc., 98, 4043 (1976).

31. H.C.Longuet-Higgins, Adv. Spectrosc., 2, 428 (1961).

BIBLIOGRAPHY (Continued)

32. R.L.Fulton and M.Gouterman, J. Chem. Phys., 35, 1059 (1961) 41, 2280 (1964).

33. C.J.Ballhausen and A.E.Hansen, Ann. Rev. Phys. Chem., 23, 15 (1972).

34. T.Azumi and K.Matsuzaki, Photochem. and Photobiol., 25, 315 (1977).

35. G.J.Small, J. Chem. Phys., 54, 3300 (1971).

36. L.Ziegler and A.C.Albrecht, J. Chem. Phys., 60, 3558 (1974).

37. L.A.Nafie, M.Pezolet and W.L.Peticolas, Chem. Phys. Lett., 20, 563 (1973).

38. N.M.Ksenofontova, V.Gg.Maslov, A.N.Sidorov and Ya.S.Bobovich, Opt. Spektrosk., 40, 309 (1976) [Opt. Spectrosc. 40, 462 (1976)].

39. M.Abe, T.Kitagawa and Y.Kyogoku, Chem. Lett., 249 (1976).

40. T.Kitagawa, H.Ogoshi, E.Watanabe and Z.Yoshida, J. Phys. Chem., 79, 2629 (1975).

41. J.M.Friedman, D.L.Rousseau and F.Adar, Proc. Natl. Acad. Sci. USA, 74, 2607 (1977).

42. J.A.Shelnutt and D.C.O'Shea, Biophys. J., 17, 252a (1976).

43. J.C.Sutherland and M.P.Klein, J. Chem. Phys., 57, 76 (1972).

44. D.W.Collins, P.M.Champion and D.B.Fitchen, Chem. Phys. Lett., 40, 416 (1976).

45. M.Gouterman, Ann. N. Y. Acad. Sci., 206, 70 (1973).

46. M.Garozzo and F.Galluzzi, in "proceedings of the Fifth International Conference on Raman Spectroscopy", ed. E.Schmid, J.Brandmuller, W.Kiefer, B.Schrader and Schrotter, Schulz, Freiburg, P.322 1976.

47. R.Liang, O.Schnepp and A.Warshel, Chem. Phys. Lett., 44, 394 (1976).

BIBLIOGRAPHY (Continued)

48. D.F.Shriver and J.R.B.Dunn, Appl. Spectrosc., 28, 319 (1974).

49. S.Mukamel and A.Nitzan, J. Chem. Phys., 66, 2462 (1977).

50. G.P.Gurinovich and B.M.Dzhagarov, Luminescence of Crystals, Molecules, and Solutions, ed. F.Williams, Pleum Press, New York, 1973.

51. S.H.Lee, Y.H.Yoon, H.Eyring and S.H.Lin, J. Chem. Phys., 66, 4349 (1977).

52. I.Shavitt, in "Method in Computational Physics", Academic Press Inc., New York, Vol. 2, P.1 (1963).

53. T.Zivkovic and Z.B.Maksic, J. Chem. Phys., 49, 3083 (1968).

54. T.Zivkovic, J. Chem. Phys., 49, 5019 (1968).

55. R.D.Ditchfield, W.J.Hehre and J.A.Pople, J. Chem. Phys., 52, 5001 (1970).

56. J.C.Brown and R.D.Poshusta, J.Chem. Phys., 36, 1933 (1962).

57. H.Takata, S.Huzinaga and K.O-ohata, J. Phys. Soc. Japan, 21, 2313 (1966).

58. S.F.Boys, Proc. Roy. Soc. (London), A200, 542 (1950).

59. L.J.Schaad and G.O.Morrell, J. Chem. Phys., 54, 1965 (1971).

60. W.D.Gwinn, J. Chem. Phys., 55, 477 (1971).

61. S.Sunder and H.J.Bernstein, J. Raman Spectrosc., 5, 351 (1976).

62. M.Abe, T.Kitagawa and Y.Kyogoku, (to be published).

63. T.C.Strekas and T.G.Spiro, Biochim. Biophys. Acta., 263, 830 (1972).

64. H.Brunner, A.Mayer and H.Sussner, J. Mol. Biol., 70, 153 (1972).

BIBLIOGRAPHY (Continued)

65. T.G.Strekas and T.G.Spiro, Biochim. Biophys. Acta., 278, 188 (1972).

66. T.G.Spiro and T.G.Strekas, Pro. Natl. Acad. Sci. USA., 69, 2622 (1972).

67. N.T.Yu, in "CRC Critical Review in Biochemistry", ed. G.Fasman. Vol 4. P.229 (1972).

68. T.G.Spiro, in "Chemical and Biochemical Application of Laser", ed. C.B.Moore. Vol 1, Chap. 2. Academic Press, New York (1974).

69. T.G.Spiro and B.P.Gaber, Ann. Rev. Biochem. 46, 553 (1977).

70. V.Fawcett and D.A.Long, in "Molecular Spectroscopy", ed. R.F.Barrow, D.A.Long and D.J.Millen, (Specialist Periodical Reports), The Chemical Society, London, Vol. 4. P.125 (1976).

71. R.H.Felton and N.T.Yu, in "The Porphyrins", ed. D. Dolphin, (1978), to be published.

72. P.R.Carey and H.Schneider, Acc. Chem. Res., 11, 122 (1978).

73. B.W.Griffin and J.A.Peterson, Ann. N. Y. Acad. Sci. 244, 107 (1975).

74. J.A.Peterson, V.Ullrich and A.G.Hildebrant, Arch. Biochim. Biophys., 145, 531 (1971).

75. T.Watanabe and S.Horie, J. Biochem., 79, 829 (1976).

76. S.C.Tang, S.Koch, G.C.Papaefthymiou, S.Foner, R.B.Frankel, J.C.Ibers and R.H.Holm, J. Am. Chem. Soc., 98, 2414 (1976).

77. H.Ogoshi, H.Sugimoto and Z.Yoshida, Tetrahedron Lett., 27, 2289 (1975).

78. C.K.Chang and D.Dolphin, Proc. Natl. Acad. Sci. USA., 73, 3338 (1976).

79. T.G.Spiro and T.C.Strekas, J. Am. Chem. Soc., 96, 338 (1974).

BIBLIOGRAPHY (Continued)

80. T.G.Spiro and T.C.Strekas, J. Am. Chem. Soc., 98, 5482 (1976).

81. G.J.Kubas and T.G.Spiro, Inorg. Chem., 12, 1797 (1973).

82. W.Keifer and H.J.Bernstein, Appl. Spectros., 25, 609 (1971).

83. S.W.May, R.S.Phillips and C.D.Oldham, Biochemistry, (in press).

84. L.Que Jr., J.D.Lipscomb, E.Munch and J.M.Wood, Biochim. Biophys. Acta., 485, 60 (1977).

85. C.A.Tyson, J. Biol. Chem., 250, 1765 (1975).

86. Y.Tomimatsu, S.Kint and J.R.Sherer, Biochem. Biophys. Res. Commun., 54, 1067 (1973).

87. P.Carey and N.M.Young, Can. J. Biochem., 52, 273 (1974).

88. B.P.Gaber, V.Miskowski and T.G.Spiro, J. Am. Chem. Soc., 96, 6868 (1974).

89. H.Fujisawa and O.Hayaishi, J. Biol. Chem. 243, 2673 (1968).

90. M.Fujiwara and M.Nozaki, Biochim. Biophys. Acta., 327, 206 (1973).

91. P.M.Champion and I.C.Gunsalus, J. Am. Chem. Soc., 99, 2000 (1977).

92. R.H.Felton, A.Y.Romans, N.T.Yu and G.R.Schonbaum, Biochim. Biophys. Acta. 434, 83 (1976).

93. L.K.Hanson, W.A.Eaton, S.G.Sligar, I.C.Gunsalus, M.Gouterman and C.R.Connell, J. Am. Chem. Soc., 98, 2672 (1976).

94. Y.Ozaki, T.Kitagawa, Y.Kyogoku, H.Shimada, T.Iizuka and Y.Ishimura, J. Biochem. 80, 1447 (1976).

95. P.M.Champion, R.D.Remba, R.Chiang, D.B.Fitchen and L.P.Hager, Biochim. Biophys. Acta., 446, 486 (1976).

BIBLIOGRAPHY (Continued)

96. P.M.Champion, R.Chiang, E.Munck, P.Debrunner and L.P.Hager, Biochemistry, 14, 4159 (1975).

97. L.Que Jr., J.D.Lipscomb, R.Zimmermann, E.Munck, N.R.Orme-Johnson and W.H.Orme-Johnson, Biochim. Biophys. Acta. 452, 320 (1976).

98. W.A.Hendrickson, G.L.Klippenstein and K.B.Ward, Proc. Natl. Acad. Sci. USA 72, 2160 (1975).

99. R.E.Stenkamp, L.C.Seiker and L.H.Jensen, Proc. Natl. Acad. Sci. USA., 73, 349 (1976).

100. J.B.R.Dunn, D.F.Shriver and I.M.klotz, Proc. Natl. Acad. Sci. USA. 70, 2582 (1973) Biochemistry, 14, 2689 (1975).

101. C.M.Yoshida, T.R.Freedman and T.M.Loehr, J. Am. Chem. Soc., 97, 1028 (1975).

102. H.Brunner and H.Sussner, Biochim. Biophys. Acta, 310, 207 (1973).

103. A.C.Albrecht, J. Chem. Phys., 33, 156 (1960).

104. R.C.Raffenetti, Int. J. Quant. Chem., 98, 289 (1975)

105. P.-O.Lowdin, J. Chem. Phys, 18, 365 (1950).

106. S.Sunder, R.Mendelsohn and H.J.Bernstein, J. Chem. Phys., 63, 573 (1975).

107. T.Kitagawa, M.Abe and H.Ogoshi, (to be published).

108. S.M.Arabei, S.F.Shkirman, K.N.Solovyov and G.D. Yegorova, Spectrosc. Lett., 10, 677 (1977).

109. G.W.Canters, G.Jansen, M.Noort and J.H. van der Waals, J. Phys. Chem., 80, 2253 (1976).

110. J.H.Dawson, R.H.Holm, J.R.Trudell, G.Barth, R.E.Linder, E.Bunnenberg, C.Djerassi and S.C.Tang, J. Am. Chem. Soc., 98, 3707 (1976).

111. K.Nakamoto, Infrared Spectra of Inorganic and Coordination Compounds, John Wiley, New York (1970).

BIBLIOGRAPHY (Continued)

112. S.Salama and T.G.Spiro, J. Am. Chem. Soc., 100, 1105 (1978)

113. F.R.Dollish, W.G.Fateley and F.F.Bentley, Characteristic Raman Frequencies of Organic Compounds, John Wiley, New York (1974).

114. H.Fujisawa, M.Uyeda, Y.Kojima, M.Nozaki and O.Hayaishi, J. Biol. Chem., 247, 4414 (1972).

115. G.A.Hamilton, in "Molecular Mechanisms of Oxygen Activation", ed. O.Hayaishi, Academic Press, New York, p.450 (1974).

116. A.Warshel, Ann. Rev. Biophys. Bioeng., 6, 273 (1977).

117. L.K.Hansen, S.G.Sligar and I.C.Gunsalus, Croat. Chem. Acta., 49, 237 (1977).

118. L.D.Spaulding, C.C.Chang, N.T.Yu and R.H.Felton, J. Am. Chem. Soc., 97, 2517 (1975).

119. T.V.Long and T.M.Leohr, J. Am. Chem. Soc., 92, 6384 (1970).

120. T.V.Long, T.M.Leohr, J.R.Allkins and W.Lovenberg, J. Am. Chem. Soc., 93, 1809 (1971).

121. L.Rimai, I.Salmen and T.Yamamoto, to be published.

122. L.K.Hansen, private communication.

VITA

Lok-Sang Duncan Cheung, son of Mr. & Mrs. Chi-Cheung Cheung, was born in Kowloon, Hong Kong on October 16, 1950.

He was a graduate from Munsang College, Kowloon City, Hong Kong in May, 1969. He entered Louisiana State University in New Orleans in September, 1969 and received the Bachelor of Science degree in Chemistry in May, 1973. In September of 1973, he began his graduate work in the School of Chemistry at the Georgia Institute of Technology.